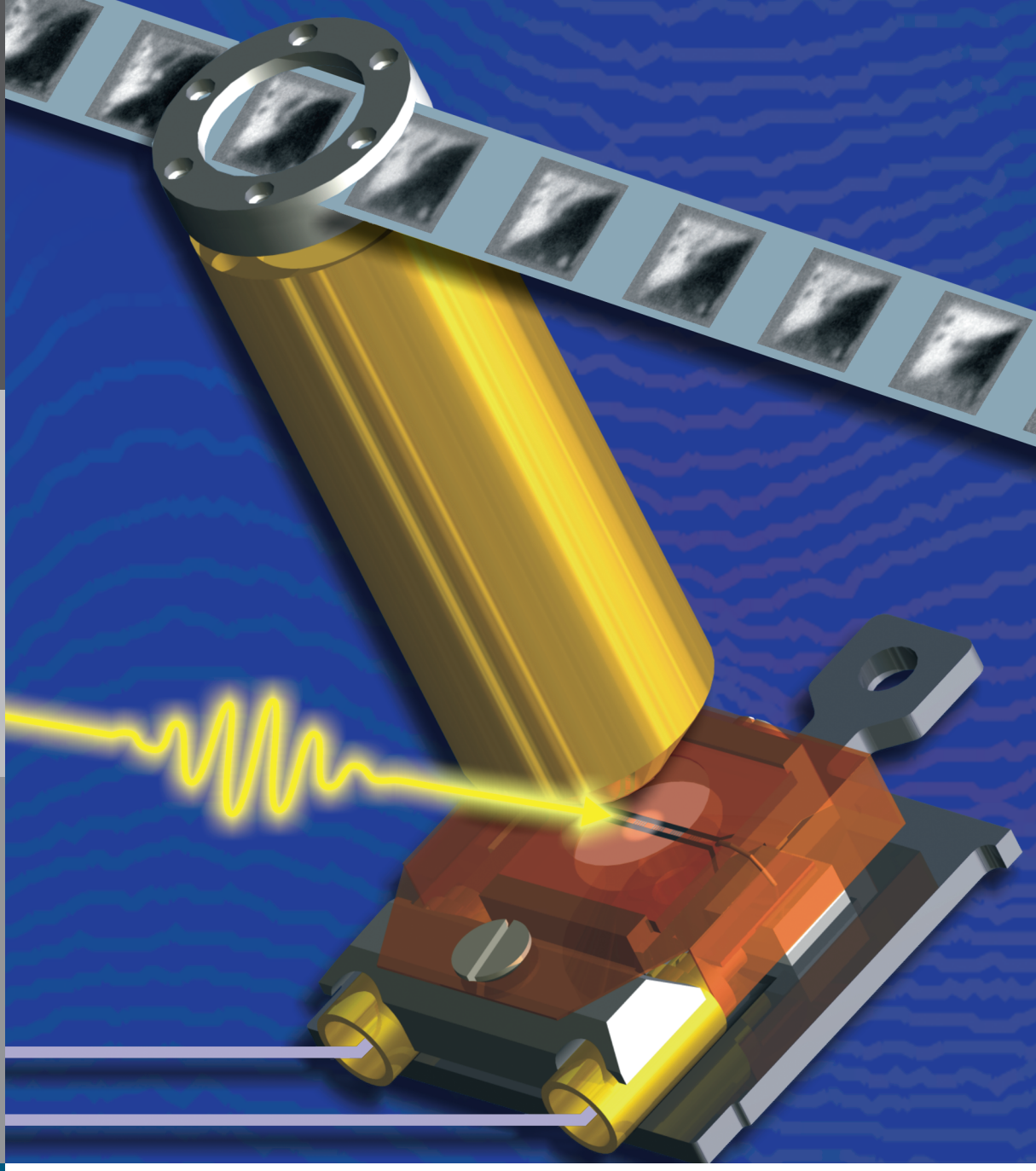

Magnetization Dynamics in Magnetically Coupled Heterostructures

Alexander Kaiser

Mitglied der Helmholtz-Gemeinschaft

JÜLICH
FORSCHUNGSZENTRUM

Schriften des Forschungszentrums Jülich
Reihe Information / Information Band / Volume 5

Forschungszentrum Jülich GmbH
Institut für Festkörperforschung (IFF)
Elektronische Eigenschaften (IFF-9)

Magnetization Dynamics in Magnetically Coupled Heterostructures

Alexander Kaiser

Schriften des Forschungszentrums Jülich
Reihe Information / Information Band / Volume 5

ISSN 1866-1777 ISBN 978-3-89336-577-7

Bibliographic information published by the Deutsche Nationalbibliothek.
The Deutsche Nationalbibliothek lists this publication in the Deutsche Nationalbibliografie; detailed bibliographic data are available in the Internet at http://dnb.d-nb.de.

Publisher and Distributor: Forschungszentrum Jülich GmbH
Zentralbibliothek, Verlag
D-52425 Jülich
phone:+49 2461 61-5368 · fax:+49 2461 61-6103
e-mail: zb-publikation@fz-juelich.de
Internet: http://www.fz-juelich.de/zb

Cover Design: Grafische Medien, Forschungszentrum Jülich GmbH

Printer: Grafische Medien, Forschungszentrum Jülich GmbH

Schriften des Forschungszentrums Jülich
Reihe Information / Information Band / Volume 5

D 464 (Diss., Duisburg, Univ., 2009)

ISSN 1866-1777
ISBN 978-3-89336-577-7

The complete volume is freely available on the Internet on the Jülicher Open Access Server (JUWEL) at http://www.fz-juelich.de/zb/juwel

Abstract

This thesis focusses on the influence of interlayer coupling on the magnetization dynamics of heterostructure systems. This topic has been investigated by time-resolved photoemission electron microscopy (PEEM) using a pump-probe approach. Magnetic and chemical contrast is provided by the illumination with circularly polarized x-rays due to the x-ray magnetic circular dichroism (XMCD) effect. In this way the spatially resolved magnetodynamic response of the single layers in asymmetric trilayer samples on short magnetic field pulses was studied . The measurements have been carried out at the electron storage rings ESRF (Grenoble) and BESSY-II (Berlin).

Samples with different material combinations have been deposited by molecular beam evaporation (MBE) and magnetron sputtering and subsequently micro-structured by optical lithography and Argon ion beam milling. Combining PEEM and magneto-optical Kerr effect (MOKE) studies the coupling conditions have been investigated. In CoFe/Cr/ NiFe and Fe/Cr/Co systems oscillatory interlayer exchange coupling depending on the Cr spacer thickness was found, while the Heusler-based Co_2MnSi/ MgO/Co_2FeSi system showed a roughness-induced orange-peel coupling.

Time-resolved measurements have been carried out on single films and interlayer exchange coupled trilayers. In single-crystalline iron films the influence of the magnetocrystalline anisotropy on the magnetodynamic response was studied. A bulging of the domain walls was found experimentally and in micromagnetic simulations. This effect is discussed in terms of an inhomogeneous demagnetizing field within the magnetic elements. In heterostructures the competition between single film properties such as shape and magnetocrystalline anisotropy and the interlayer exchange coupling was studied. The single films showed an inhomogeneous response with a locally varying coupling strength due to locally enhanced magnetic stray fields at domain walls or defects. The results are discussed in terms of the local energy contributions. By varying the temporal shape of the excitation field different magnetodynamic reactions have been investigated. Using short magnetic field pulses magnetic eigenmodes have been excited that have been reproduced by macro-spin calculations. The frequency of the eigenmode was found to be considerably increased due to the interlayer coupling.

Zusammenfassung

Das Thema dieser Arbeit ist der Einfluss von Zwischenschicht-Kopplung auf die Magnetisierungsdynamik magnetischer Heteroschichten. Die Fragestellung wurde mittels zeitaufgelöster Photoemissions-Elektronen-Mikroskopie (PEEM) untersucht. Dabei erhält man magnetische und chemische Empfindlichkeit durch die Beleuchtung der Probe mit zirkular polarisierter Röntgenstrahlung aufgrund des magnetischen Röntgenzirkular-Dichroismus (XMCD). Auf diese Weise wurde in asymmetrischen Dreischicht-Systemen die magnetodynamische Reaktion der einzelnen Schichten auf kurze magnetische Feldpulse ortsaufgelöst untersucht. Die Messungen wurden an den Elektronenspeicherringen ESRF (Grenoble) und BESSY-II (Berlin) durchgeführt.

Proben mit unterschiedlichen Materialkombinationen wurden mit Molekularstrahlepitaxie (MBE) und Magnetronsputtern hergestellt und anschließend mittels optischer Lithographie und Argon-Ionenstrahl-Ätzen mikro-strukturiert. Die Kopplungsbedingungen wurden mit PEEM und dem magnetooptischen Kerr-Effekt (MOKE) untersucht. Dabei wurde in Fe/Cr/Co- und CoFe/Cr/NiFe-Systemen eine oszillierende Zwischenschicht-Austausch-Kopplung, die von der Chrom-Zwischenschichtdicke abhängt, beobachtet, während Heusler-basierte $Co_2MnSi/MgO/Co_2FeSi$-Proben eine rauhigkeitsinduzierte Orangenhautkopplung aufwiesen.

Zeitaufgelöste Messungen wurden an Einzelschichten und zwischenschichtgekoppelten Dreifachschichten durchgeführt. An einkristallinen Eisenschichten wurde der Einfluss der magnetokristallinen Anisotropie auf die Magnetodynamik untersucht. Dabei wurde sowohl experimentell, als auch in mikromagnetischen Simulationen, eine Ausbeulung der Domänenwände beobachtet, die durch das inhomogene Streufeld der Mikrostrukturen erklärt werden kann. In Heteroschichten wurde der Einfluss der Austauschkopplung und der Eigenschaften der Einzelschichten wie magnetokristalliner und Formanisotropie untersucht. Dabei zeigten die einzelnen Schichten unterschiedliche inhomogene Reaktionen mit einer örtlich veränderlichen Kopplungsstärke aufgrund von lokalen Streufeldern an Domänenwänden und Defekten. Die experimentellen Ergebnisse werden anhand der lokalen Energiebeiträge diskutiert. Durch eine Variation der zeitlichen Form des Anregungspulses konnten unterschiedliche magnetodynamische Effekte untersucht werden. So wurden mithilfe von kurzen Feldpulsen magnetische Eigenmoden angeregt, die mit Makrospin-Berechnungen reproduziert werden konnten. Dabei war die Frequenz der angeregten Eigenmode erheblich aufgrund der Zwischenschichtkopplung erhöht.

Acknowledgements

The work shown in this thesis was not carried out only by myself but it was done in collaboration with several colleagues, whom I want to thank at this point:

Prof. Dr. Claus M. Schneider for providing the environment and my position to perform this research. I am very grateful to him for supervising me after the loss of Ulrich Hillebrecht and for sharing his experience at synchrotron beamtimes.

Prof. Dr. Hans Joachim Elmers for accepting the task of co-examiner of the thesis.

Dr. Ulrich Hillebrecht for sparking my interest in the topic of photoemission microscopy. I enjoyed the first and unfortunately only beamtime that we attended together and the exploration of various beer gardens in Köpenick and Rudow. Regrettably, he did not have the chance to see the success of the experiments.

Dr. Carsten Wiemann for the successful collaboration and proof-reading of the manuscript. Thanks to his PEEM experience, we could squeeze the maximum of spatial resolution out of the microscope.

Dr. Stefan Cramm for motivating me during many long night shifts, helpful phone support and sharing his synchrotron knowledge.

Konrad Bickmann und Bernd Küpper for various invaluable design and construction works, that often had to be done on short notice, and the interesting insights into bunker and Fiesta technology.

Heinz Pfeifer for building several irreplaceable "Heinz-devices" and his almost unlimited reservoir of connectors, cables and measuring instruments.

Reinert Schreiber for the careful deposition of excellent MBE samples.

Jürgen Lauer for keeping track of the Labview-spaghetti and the quick bugfixing even without having access to a test-synchrotron.

Prof. Dr. Charles S. Fadley and Dr. Florian Kronast for the opportunity to take part at the exciting standing-wave PEEM experiments.

Dr. Krysztof Grzelakowski for visiting Jülich for supporting us with PEEM maintenance and for his explanations regarding the microscope layout.

Dr. Ingo Krug for guiding my first steps at the Elmitec PEEM, assisting me with the RF sample holder construction and for his powerful set of Igor methods.

Dr. Diana Rata, Dr. Debjani Banerjee and Franz-Josef Köhne for maintaining the magnetron sputter machine and for the deposition and characterization of the Heusler films.

Dr. Matthias Buchmeier for instructing me to operate the MOKE set-up and his helpful explanations regarding the analysis and interpretation of MOKE measurements.

The team of the IFF mechanical workshop, headed by Kurt Hirtz, for the realization of mechanical works.

Mona Nonn for the fabrication of masks for the optical lithography.

Holger John for the support of the IFF clean room.

Dr. Riccardo Hertel for fruitful discussions and helpful suggestions regarding the interpretation of domain patterns.

Dr. Martin Weides for providing access to the sputtering machine, the maintenance of the wire bonder and the organization of the Cologne physicists bowling events.

All colleagues at the IFF for the enjoyable collaboration and infrequent non-physical activities, particularly my room mates **Christian Spudat**, **Mohammed Qureshi** and **Carsten Wiemann** for the pleasant working atmosphere, the supply of coffee and occasional distraction from the regular research routine.

The staff at **BESSY** and the beamline ID08 at the **ESRF**, especially our local contact **Carsten Tieg**, for their technical support during the beamtimes.

The **SFB 491** for the financial support of my thesis, and all colleagues from Duisburg and Bochum for providing each other with samples and measurements.

All good friends and my family for a life besides research: Especially my girlfriend **Uta Lebioda** for accompanying and emotionally supporting me during the previous months, **Dennis Meier** for the careful proof-reading of my thesis and spare time activities spent together, **Julian Ulrich** and **David Behrle** for providing the balance for the beamtime stress in Berlin and my parents **Jutta and Hans-Joachim Kaiser** for their interest and support during my studies.

Contents

Chapter 1

Introduction

Layered magnetic structures have become an integral part of today's technology. They can be found in various types of electronic devices such as sensors (PARKIN *et al.*, 2003), hard disk read heads (BERGER, 2009) or transistors (JANSEN, 2003). It was the improvement of high-vacuum molecular-beam epitaxy (MBE) starting in the early 1980ies, that allowed for the controlled epitaxial growth of magnetic thin film systems in the monolayer regime (BLAND & HEINRICH, 2005). Soon various physical effects such as *interlayer exchange coupling* (GRÜNBERG *et al.*, 1986) and the Nobel prize-awarded *giant magneto-resistance* (GMR) effect (BINASCH *et al.*, 1989; BAIBICH *et al.*, 1988) had been discovered and previously known effects like the *tunnelling magnetoresistance* (TMR) (JULLIERE, 1975; MOODERA *et al.*, 1995) and *exchange anisotropy* (MEIKLEJOHN & BEAN, 1956; NOGUÉS & SCHULLER, 1999) experienced a revival in magnetic thin film devices. All those effects led to the establishment of the field of *spintronics* as a new research area that is attractive for both physicists, due to the quantum character of the electron spin, and engineers, due to the vast potential for new devices with novel functionalities, e.g. MRAM (GALLAGHER & PARKIN, 2006) or magnetic logics (REISS, 2009). An overview of different configurations of layered magnetic structures is given in fig. 1.1.

The integration of magnetic heterostructures into the read heads of hard disk drives has decisively determined the ongoing progression of storage density and thus assured the supremacy of hard disks over other mass storage devices. More than ten years ago, hard disk read heads have become the major area of application of the 1989 discovered GMR effect, that gives rise to a dependence of the resisitivity of a magnet-metal-magnet trilayer on the relative orientation of the two magnetic layers. In hard disks this effect is exploited in so-called spin-valves where the orientation of one magnetic layer is fixed while the other one aligns along the stray field of the bits written in the storage material (fig. 1.1(c)). Thus, for the decrease of access times with every new product generation, the switching speed of the free layer in the read head is one

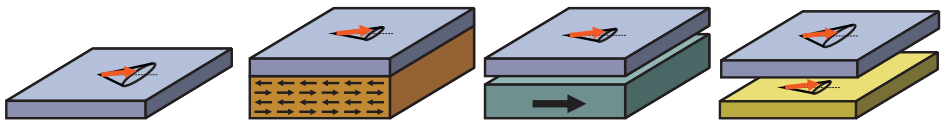

Figure 1.1: Different configurations of important magnetic layered systems: (a) single magnetic layer, (b) ferromagnetic-antiferromagnetic interface inducing exchange anisotropy in the ferromagnetic layer, (c) spin-valve system with fixed bottom and free top layer, (d) coupled system of two ferromagnetic layers.

of the major factors. Therefore, a fundamental knowledge of magnetization reversal in magnetic heterostructures is mandatory for maintaining the technical progress.

The physics behind magnetization reversal has been investigated since the beginning of the 20th century. Soon it became clear that several processes taking place on different timescales are involved in magnetization reversal and for a full understanding of the complex magnetization dynamics both high temporal and spatial resolution of the measurement technique are mandatory. For almost fifty years the temporal resolution has been obtained within the frame of pump-probe approaches. In this way reversible processes can be studied by stroboscopic illumination of a sample at a controllable delay after the excitation with a magnetic field. Most of the previous experiments were based on the *magneto-optical Kerr effect* (MOKE) relying on the polarization rotation of linearly polarized light during the reflection on a magnetic surface. In first experiments by CONGER & TOMLINSON (1962) the sun was used as a light source, with the light beam being artificially pulsed by mechanical devices, while in more advanced experiments KRYDER & HUMPHREY (1969) made use of electro-optical shutters to improve the temporal resolution. With a temporal resolution being in the nanosecond regime, these experiments focussed on rather slow magnetodynamic reactions such as the magnetization reversal by motion of the magnetic domain walls or coherent magnetization rotation.

With the availability of short-pulse lasers in the 1980s the interest in the study of magnetization dynamics was revived. Due to the higher temporal resolution of the probe beam also the temporal width of the excitation signal had to be decreased. This could be achieved by the generation of the magnetic field directly on the sample by lithographically defined coplanar waveguides or microcoils, through which short current pulses are sent giving rise to a local Oersted field acting on the magnetic microstructures. The temporal resolution in the picosecond regime that could be obtained in this manner enabled the study of the precessional motion of the spins in a magnetic field – composed of both external and internal components. In spatially resolved experiments the inhomogeneous magnetization reversal in small Permalloy elements (HIEBERT *et al.*, 1997) or the motion of micromagnetic features such as mag-

netic domain walls or vortices (PARK *et al.*, 2003) was investigated. In both examples, the influence of inhomogeneous internal fields on the magnetization dynamics were studied by the combination of spatial and temporal resolution.

As the MOKE effect provides no way of elemental discrimination, the first experiments were limited to the study of magnetic single layers (fig. 1.1(a)). For the study of magnetic multilayers, however, the sample depth becomes an important degree of freedom, becoming accessible after the discovery of the *X-ray magnetic circular dichroism* (XMCD) effect by SCHÜTZ *et al.* (1987). It is based on the absorption of circular polarized X-rays from a synchrotron radiation source at the core-levels of a given atom. Thus, the way was paved for the element-selective analysis of magnetic moments. It was soon applied together with spatially resolving methods such as *photoemission electron microscopy* (PEEM) for an element-selective analysis of the micromagnetic configuration (STÖHR *et al.*, 1993). In first experiments applying the elemental selectivity to magnetic multilayer samples the antiparallel coupling of a chromium monolayer to an epitaxial iron film (SCHNEIDER *et al.*, 1996) and the effect of interlayer exchange coupling on the orientation of the magnetic domains in the iron/chromium/cobalt system (KUCH *et al.*, 1998) was studied with XMCD-PEEM. Using a combination of the XMCD and *X-ray magnetic linear dichroism* (XMLD) effects NOLTING *et al.* (2000) studied the coupling of spins at the ferromagnet-antiferromagnet interface (fig. 1.1(b)).

Due to the pulsed time-structure of the synchrotron radiation the pump-probe approach to magnetization dynamics could be easily implemented in PEEM experiments (VOGEL *et al.*, 2003; KRASYUK *et al.*, 2003). Subsequent experiments revealed the motion of the vortex core (CHOE *et al.*, 2004) or the coexistence of domain wall motion and spin precession (RAABE *et al.*, 2005) in small magnetic elements.

Only few experiments have been conducted so far, exploiting elemental selectivity and temporal resolution at the same time for the study of magnetic multilayers. BONFIM *et al.* (2001) have studied the switching behaviour of magnetically coupled cobalt/Al_2O_3/Permalloy trilayer systems in an XMCD-based experiment. They investigated the difference in the coupling in the dynamic and static regime. However, due to the spatially integrating technique the influence of the different reversal mechanisms could only be studied indirectly by evaluating the switching times. VOGEL *et al.* (2004, 2005) have carried out several PEEM experiments on pseudo-spin-valve elements consisting of a soft-magnetic Permalloy layer interlayer exchange coupled to a magnetically harder Cobalt film, as indicated in fig. 1.1(c). Under the application of a moderate magnetic field pulse the magnetization of the Permalloy film was realigned, while the hard Cobalt magnetization was not affected and provided the restoring field for the Permalloy magnetization. It was found that local domain wall stray fields significantly enhance the coupling of the ferromagnetic films serving as a preferential nucleation centre for new domains. A different approach was used by CHOU *et al.* (2006): Using scanning transmission X-ray microscopy (STXM) they studied the cobalt/copper/Permalloy system under a sinusoidal excitation field. In both

layers they found an oscillatory motion of the vortex core with a phase shift of 180° between the two layers that was attributed to a dipolar coupling between the two ferromagnetic films. However, due to the differential technique that was used in these measurements, this method is only applicable to oscillatory processes.

The aim of this thesis is to explore ways to overcome these restrictions. We have combined temporal, spatial and elemental resolution and carried out experiments on asymmetric trilayer samples where both magnetic layers exhibited a reaction on the pulsed excitation (fig. 1.1(d)). The layer-dependent response is determined by both the intrinsic layer properties such as the saturation magnetization, the magnetocrystalline anisotropy and the damping constant and the interlayer coupling of the two magnetic layers. Before carrying out time-resolved measurements on trilayers, the magnetostatic sample properties of the trilayers have been studied in the equilibrium configuration and the dynamic properties of single layers with different magnetic properties have been investigated in separate time-resolved experiments. The findings of these preparatory experiments will be considered in the interpretation of the time-resolved experiments.

This thesis is organized as follows:

In **chapter 2** the fundamental aspects determining the magnetic configuration of interlayer coupled systems will be introduced. The important energy terms will be discussed and based on these considerations different aspects of domain formation and magnetization dynamics will be derived.

Chapter 3 is devoted to the experimental methods used in this thesis. The magnetic characterization with the XMCD effect and the image formation in a PEEM will be introduced.

In order to carry out time-resolved measurements technical development had to be made, that will be described in **chapter 4**. These technical preparations include the development of a sample-holder/sample-stage combination equipped with high-frequency compatible cabling and adapters, the sample design and the implementation of a gating technique allowing for the selection of photoelectron pulses with a desired repetition frequency independent of the light source frequency. Furthermore, first microscopy experiments involving standing wave-enhanced photoemission, that will allow for depth-resolved measurements, will be presented.

In **chapter 5** layer-resolved PEEM measurements of magnetic trilayer systems will be shown. The images of the magnetization patterns taken for different coupling parameters of the two magnetic layers will be interpreted in terms of their material properties and coupling conditions. The PEEM experiments will be correlated to quasistatic MOKE measurements from which the coupling parameters are derived.

Chapter 6 focusses on the study of magnetization dynamics in magnetic single layer elements of iron and Permalloy ($Ni_{80}Fe_{20}$) that show a different magnetodynamic

behaviour due to the difference in the magnetocrystalline anisotropy. In the measurements the Iron domain walls were found to bulge under the influence of the magnetic field. The measurements will be related to results obtained from micromagnetic simulations and interpretations of the domain wall bulging will be given.

Chapter 7 shows time-resolved measurements on magnetic heterostructures. A distinctly inhomogeneous behaviour was found with spatially varying influence of demagnetizing field, magnetocrystalline anisotropy and interlayer coupling. Based on the findings regarding the equilibrium magnetization patterns of heterostructures from chapter 5 and the time-resolved behaviour of single layers from chapter 6, the results will be assigned to the single layer properties and the coupling conditions. By applying excitation signals of different timescale and shape, different magnetodynamic reactions have been provoked.

Finally, in **chapter 8** the experimental results will be summarized and an outlook on future experiments will be given.

Chapter 2

Fundamentals

This chapter covers the fundamental energy terms determining the magnetic configuration of interlayer coupled thin film systems. Both the phenomenological description and physical origins will be presented. Based on the energetics of the ferromagnetic system the formation of magnetic domains and different aspects of magnetization dynamics will be discussed.

2.1 Ferromagnetism of 3d transition metals

While the origin of ferromagnetic order in the rare earth elements can be understood by a model of localized magnetic moments being regularly arranged on a lattice and interacting with each other, this model does not succeed in calculating the magnetic moments and high Curie temperatures occurring in 3d transition metals like iron, cobalt and nickel (BLUNDELL, 2001). Due to the delocalized structure of the 3d electrons also the ferromagnetic behaviour of these materials has to be treated within a band-model. The simplest band-model explaining ferromagnetic ordering is the Stoner-Wohlfarth-Slater-model of metallic ferromagnetism (STONER, 1938) that will be introduced in the following.

Quantum-mechanically, the origin of ferromagnetism is the *exchange interaction* leading to a preferential parallel ordering of the magnetic moments due to an electrostatic energy gain. Because of the Pauli principle the spins of different electrons cannot occupy the same electronic state, if they are aligned parallel. Thus they are promoted to states with a higher kinetic energy. At the same time the overlap of the electron wave functions is reduced and so is the Coulomb repulsion between those electrons. If the reduction of the Coulomb energy exceeds the increase in kinetic energy, the parallel ordering of the spins is energetically favoured and spontaneous ferromagnetism will occur.

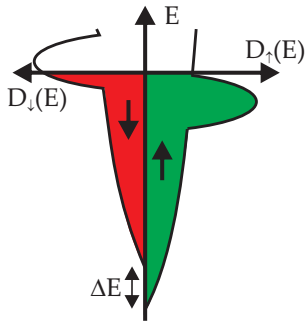

Figure 2.1: Schematic spin-split density of states (DOS) of a 3d metal with exchange splitting ΔE. Due to the high DOS at the Fermi energy E_F the Stoner criterion is fulfilled and spontaneous ferromagnetism occurs.

A quantitative condition for the occurrence of spontaneous ferromagnetic ordering is the *Stoner criterion* that will be derived in the following (after BLUNDELL, 2001). Due to their delocalized nature the valence electrons in the 3d metals have to be treated in a collective way by a band-model. Consider the density of states of a metal without magnetic ordering. Parallel alignment requires an asymmetry between spin-down and spin-up electrons. In the band model this is achieved by taking electrons from the spin-down side with energies from $E_F - \delta E$ to E_F and placing them at energies from E_F to $E_F + \delta E$ at the spin-up side. Supposing a constant density of states around the Fermi energy $D(E_F)$, the number of electrons in this energy interval is $D(E_F)\delta E/2$. The change in kinetic energy is thus

$$\Delta E_{\text{kin}} = \frac{1}{2} D(E_F)(\delta E)^2. \tag{2.1}$$

As stated above, this increase in kinetic energy is connected to a reduction of Coulomb energy due to the Pauli principle. With I representing the Stoner parameter describing effective exchange interactions between electrons, the change in potential energy is

$$\Delta E_{\text{pot}} = -\frac{1}{2} I(D(E_F)\Delta E)^2. \tag{2.2}$$

The total change of energy is

$$\Delta E = \Delta E_{\text{kin}} + \Delta E_{\text{pot}} = \frac{1}{2} D(E_F)(\Delta E)^2(1 - ID(E_F)). \tag{2.3}$$

Thus spontaneous ferromagnetism occurs if $\Delta E < 0$, which is fulfilled for

$$I \cdot D(E_F) \geq 1. \tag{2.4}$$

This relation is known as the *Stoner criterion*.

With the exchange interaction $I \cong 1$ eV being similar for all 3d metals (STÖHR & SIEGMANN, 2006), the condition for ferromagnetic ordering strongly depends on the density of states around the Fermi energy. While for iron, cobalt and nickel the Fermi energy crosses the $3d$ bands yielding high $D(E_F)$ values (see fig. 2.1) and the Stoner

criterion is fulfilled, in copper the completely filled $3d$ band is situated well below the Fermi energy and thus the Stoner criterion is not satisfied.

For the description of the energy density stored in the exchange interaction the Heisenberg formalism can be used. Originally been formulated for the interaction of localized spins $\boldsymbol{S_i}$ the Heisenberg Hamiltonian

$$\mathcal{H}_{\text{Heisenberg}} = -2\sum_{i,j} J_{ij}\boldsymbol{S_i}\cdot\boldsymbol{S_j} \tag{2.5}$$

with the exchange integral J_{ij} can be used in a continuous approximation for the derivation of the exchange energy of a metallic magnet. On a continuum level the exchange integrals J_{ij} are replaced by the exchange stiffness parameter A and the single spins $\boldsymbol{S_i}$ are replaced by a continuous magnetization $\boldsymbol{M}(\boldsymbol{r})$. Then the exchange energy density becomes (LANDAU & LIFSHITZ, 1935)

$$f_{\text{exc}} = A(\boldsymbol{\nabla}\cdot\boldsymbol{M}(\boldsymbol{r}))^2. \tag{2.6}$$

2.2 Anisotropy

Observation tells us, that the magnetization cannot freely rotate in single-crystalline samples due to the formation of magnetically easy and hard axes. In a phenomenological picture, the magnetic anisotropy is the energy that it takes to rotate the magnetization from an easy axis to a hard axis (STÖHR & SIEGMANN, 2006). It must be constant when the magnetization is reversed. Thus, the contribution of the anisotropy to the free energy density of an uniaxial system can be expressed by a series expansion in even functions of the angle γ enclosed by the magnetization $\boldsymbol{M}$ and the easy axis

$$f_{\text{ani}} = K_1\sin^2\gamma + K_2\sin^4\gamma + K_3\sin^6\gamma + \ldots \tag{2.7}$$

where K_i are the anisotropy constants with dimension [energy/volume]. The magnetic anisotropy can be represented by an effective anisotropy field $\boldsymbol{H}_{\text{ani}}$ which is defined as the field which generates a torque $\boldsymbol{T} = V\cdot\mu_0\boldsymbol{M}\times\boldsymbol{H}$ equal to the torque that the effective anisotropy exercises on $\boldsymbol{M}$ given by $\partial E_{\text{ani}}/\partial\gamma$. Including only $K_1 \neq 0$ this yields

$$\mu_0 H_{\text{ani}} = \frac{2K_1}{M}\cos\gamma. \tag{2.8}$$

The energy minimization of the integral over eqs. (2.6) and (2.7) defines the characteristic *exchange length*

$$l_{\text{exc}} = \sqrt{A/K_1}, \tag{2.9}$$

which is the distance over which the magnetization is expected to change direction in the presence of an anisotropy.

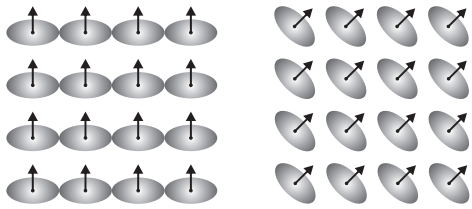

Figure 2.2: Illustration of the magnetocrystalline anisotropy: A rotation of the magnetization leads to a different overlap of the atomic orbitals (blue) and the electrostatic energy of the system is changed. (after BERGMANN *et al.*, 2005).

In a cubic system the energy density must be invariant under permutations of the directional cosines $\alpha_{1,2,3}$ of $\boldsymbol{M}$ with respect to the crystal axes due to symmetry arguments (BIHLMAYER, 2005):

$$f_{\text{ani}} = K_1(\alpha_1^2\alpha_2^2 + \alpha_1^2\alpha_3^2 + \alpha_2^2\alpha_3^2) + K_2\alpha_1^2\alpha_2^2\alpha_3^2 + \dots \tag{2.10}$$

Two major effects contribute to the anisotropy in magnets: the magnetocrystalline anisotropy due to the spin-orbit interaction and the shape anisotropy due to the interaction of the magnetization with its own stray field. Both effects have strong influence on both micromagnetic structure and temporal behaviour and will thus be discussed in the following.

2.2.1 Magnetocrystalline anisotropy

The physical origin of the magnetocrystalline anisotropy lies in the spin-orbit coupling and the crystal field generated by neighbouring atoms. For a multi-electron system the isotropic spin moment $\boldsymbol{S}$ is coupled to the anisotropic orbital moment $\boldsymbol{L}$. This spin-orbit interaction is described by the Hamiltonian $\mathcal{H}_{SO} = \xi(\boldsymbol{r})\boldsymbol{L}\cdot\boldsymbol{S}$ with the effective coupling constant $\xi(\boldsymbol{r})$, which is of the order of 50-100 meV for the $3d$ electrons. The magnetocrystalline anisotropy is the difference of the spin-orbit terms for the alignment along the easy and hard axes

$$\Delta f_{\text{MCA}} = \langle H_{SO}\rangle_{\text{hard}} - \langle H_{SO}\rangle_{\text{easy}} = \xi(\boldsymbol{r})\left(\langle \boldsymbol{L}\cdot\boldsymbol{S}\rangle_{\text{hard}} - \langle \boldsymbol{L}\cdot\boldsymbol{S}\rangle_{\text{easy}}\right). \tag{2.11}$$

The exact derivation of the energy changes due to a different magnetization orientation is rather complex and will thus not be carried out here (for a review see BRUNO (1993) or BLÜGEL (1999)). However the effect leading to the magnetocrystalline anisotropy can be easily understood within the model shown in fig. 2.2. Due to the spin-orbit coupling a rotation of the spin system also induces a rotation of the orbital moments and thus a reorientation of the atomic orbitals. Neglecting magnetostrictive effects the crystal lattice on which the orbitals are placed is not changed and thus a magnetization rotation may lead to a different overlap of the orbitals of

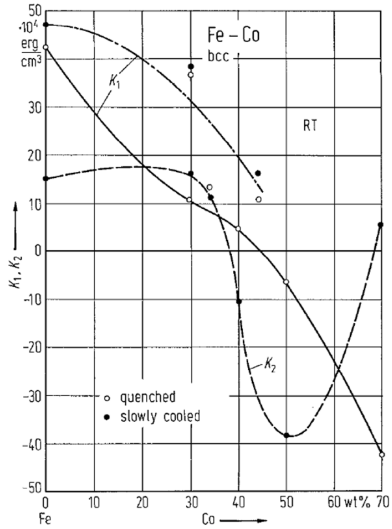

Figure 2.3: Magnetocrystalline anisotropy constants K_1 and K_2 of bcc Fe_xCo_{1-x} alloys (from BONNENBERG *et al.*, 1986). By the proper choice of chemical composition anisotropy can be switched on/off or rotated by 45° without changing the crystal structure.

neighbouring atoms yielding a change in electrostatic energy. Therefore, the magnetization direction with the lowest electrostatic energy is favourable. From this model it is also obvious that the magnetocrystalline anisotropy must reflect the symmetry of the crystal lattice.

Due to its electronic origin, the values of the magnetocrystalline anisotropy constants are strongly influenced by band structure effects. For similar lattice constants the anisotropy can change between positive and negative values when the chemical composition of an alloy is varied, as shown in fig. 2.3 for the example of Co_xFe_{1-x}. Hence by the choice of the chemical composition the anisotropy constant can be tuned to desired values.

2.2.2 Shape anisotropy

Another source of anisotropy in a sample with finite dimensions is the interaction with the demagnetizing field. The demagnetizatizing field H_d is generated at magnetic charges that are created on the boundaries of a magnetic object (see fig. 2.4 for an illustration). The demagnetizing field $\boldsymbol{H_d}$ is defined by the divergence of the magnetization $\boldsymbol{M}$ (HUBERT & SCHÄFER, 1998)

$$\boldsymbol{\nabla} \cdot \boldsymbol{H_d} = -\boldsymbol{\nabla} \cdot \boldsymbol{M}. \tag{2.12}$$

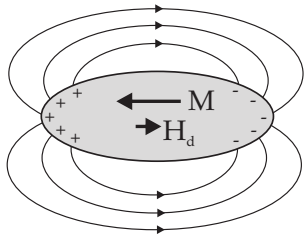

Figure 2.4: Illustration of the stray field and the demagnetizing field H_d of an ellipsoidal magnetic particle. At the poles of the particle magnetic charges (marked by + and -) are generated giving rise to the demagnetizing field opposite to the magnetization direction. The stray field is smallest when the magnetization is oriented parallel to the long axis.

The sinks and sources of $\boldsymbol{M}$ act like positive and negative poles of $\boldsymbol{H_d}$. The energy of a magnetic sample in its own stray field is given by

$$E_d = \frac{\mu_0}{2} \iiint\limits_{\text{all space}} \boldsymbol{H_d}^2 \mathrm{d}V = -\frac{\mu_0}{2} \iiint\limits_{\text{sample}} \boldsymbol{H_d} \cdot \boldsymbol{M} \mathrm{d}V. \tag{2.13}$$

The stray field is related to the magnetization by the symmetrical demagnetization tensor $\mathbf{N}$:

$$\boldsymbol{H_d} = -\mathbf{N}\boldsymbol{M}. \tag{2.14}$$

In the case of a spherical sample $\mathbf{N}$ is diagonal with $N_{11} = N_{22} = N_{33} = 1/3$. For an infinitely extended thin film with the surface in the xy-plane the demagnetization factors in the plane vanish $N_{11} = N_{22} = 0$ and $N_{33} = 1$. In that case the energy density of the demagnetizing field can be written in the form of an uniaxial anisotropy energy density (see eq. (2.7))

$$f_{\text{shape}} = \frac{E_d}{V} = -\frac{\mu_0}{2} \boldsymbol{H_d} \cdot \boldsymbol{M} = \frac{\mu_0 M_s^2}{2} \cdot \cos^2\theta = \frac{\mu_0 M_s^2}{2} \cdot \sin^2(\pi/2 - \theta) \tag{2.15}$$

with the shape anisotropy constant $K_s = \mu_0 M_s^2/2$. Due to the interaction with the demagnetizing field the magnetization tends to orient in a direction with minimum H_d values. For a thin film the shape anisotropy constrains the magnetization in the sample plane and in the case of an infinitely long magnetic rod the magnetization is aligned along the rod axis.

For a rectangular prism the demagnetizing factors can be calculated by a formula derived by AHARONI (1998). The demagnetization factors of a flat platelet with lateral dimensions $a = 10\,\mu\text{m}$, $b = 5\,\mu\text{m}$ and thickness $c = 10\,\text{nm}$, for example, are $N_{11} = 0.0023$, $N_{22} = 0.0046$, $N_{33} = (1 - N_{11} - N_{22}) = 0.9931$. For small deviations the lateral demagnetization factors scale with a/c and b/c, respectively.

2.3 Coupling of Ferromagnetic Films

When two permanent magnets are brought together, they start influencing each other by their magnetic fields. In order to obtain a state of closed magnetic flux, they will

arrange antiparallel because the north pole of one magnet will be attracted by the south pole of the other and vice versa. This type of dipolar coupling of the fringing fields of magnets is also responsible for the alignment of magnetic thin films as long as they stay sufficiently separated from each other, e.g. by oxide layers, contamination or roughness (BÜRGLER & GRÜNBERG, 2005). However, if brought into direct contact, the two magnets will align parallel due to direct exchange coupling of the spins. In the limit of thin barriers between the ferromagnetic films, their alignment is determined by the competition of different mechanisms such as direct exchange coupling, magnetostatic coupling and interlayer exchange coupling. Thus, the relative orientation of two magnetic thin films separated by a thin spacer layer has been the topic of interest for many research groups (see STILES (2004) for a review).

Phenomenologically the areal energy density of a system of two coupled magnetic layers can be written as

$$\sigma_{\text{coupl}} = -J_1(\boldsymbol{m_1} \cdot \boldsymbol{m_2}) - J_2(\boldsymbol{m_1} \cdot \boldsymbol{m_2})^2 \tag{2.16}$$

with the coupling parameters $J_{1,2}$ for bilinear and biquadratic coupling, respectively (DEMOKRITOV, 1998). Depending on the sign of J_1, the collinear coupling aligns the two layers parallel ($J_1 > 0$) or antiparallel ($J_1 < 0$). For $J_2 < 0$ the biquadratic term favours a non-collinear canted configuration of $\boldsymbol{m_1}$ and $\boldsymbol{m_2}$.

2.3.1 Magnetostatic coupling

As stated in the introduction, the macroscopic fringing fields at the edges of two ferromagnets favour an antiparallel alignment of the films, but also in a more microscopic view fringing fields occurring at interfaces are influencing the magnetic coupling of thin films through a non-magnetic interlayer. This type of coupling is referred to as *orange-peel coupling* or *Néel coupling*, named after its discoverer NÉEL (1962a,b).

At a rough interface, there are magnetic poles at the surface. For a slowly varying surface height the distribution of these "magnetic charges" as shown in figs. 2.5(a) and 2.5(b) $\sigma(\boldsymbol{r})$ can be written as

$$\sigma(\boldsymbol{r}) = \boldsymbol{M} \cdot \boldsymbol{n}(\boldsymbol{r}) \tag{2.17}$$

with the local surface normal $\boldsymbol{n}(\boldsymbol{r})$ (STILES, 2004). The interaction of the magnetic charge densities $\sigma_{1,2}$ of two such interfaces separated by a non-magnetic spacer layer of constant thickness D is

$$E = \mu_0 \int\limits_{\text{Interface 1}} \mathrm{d}^2 r_1 \int\limits_{\text{Interface 2}} \mathrm{d}^2 r_2 \frac{\sigma_1 \boldsymbol{r_1} \sigma_2 \boldsymbol{r_2}}{\sqrt{D^2 + (\boldsymbol{r_1} - \boldsymbol{r_2})^2}}. \tag{2.18}$$

By considering sinusoidally varying correlated interfaces at the vertical positions $z_1 = \delta \cos(2\pi x/\lambda)$ and $z_2 = \delta \cos(2\pi x/\lambda) + D$ being separated by a spacer with constant

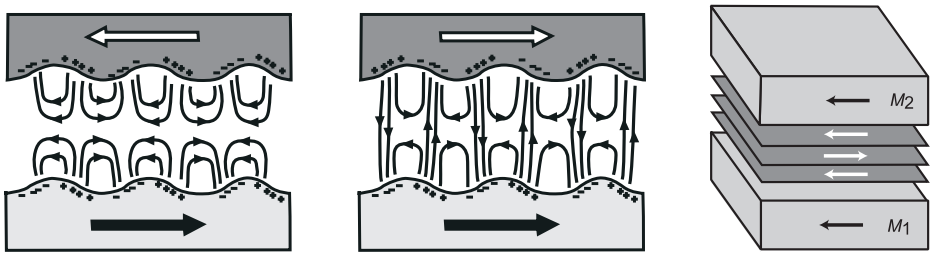

(a) Antiparallel aligned layers with correlated interface roughness (STILES, 2004).

(b) By parallel alignment the fringing fields change lowering the field energy (STILES, 2004).

(c) Direct exchange coupling through an antiferromagnetic interlayer (after BÜRGLER & GRÜNBERG, 2005)

Figure 2.5: Illustration of orange peel coupling (a, b) and direct exchange coupling through an antiferromagnetic interlayer (c).

thickness D, the coupling between the layers is parallel with strength

$$J_1 = \mu_0 M_1 M_2 \frac{\delta^2}{\lambda} e^{-2\pi D/L} \tag{2.19}$$

with $M_{1,2}$ the corresponding values of the saturation magnetization along the sample plane. Eq. (2.19) shows that for flat films with $\delta \to 0$ and for large spacer thickness $D \to \infty$ J_1 disappears.

2.3.2 Direct exchange coupling

When the magnetic layers are not separated by an interlayer or the interlayer has pinholes, the spins of both layers are coupled by direct exchange interaction inducing a parallel alignment of two ferromagnetic layers in direct contact.

If a ferromagnetic film (FM) is brought into direct contact with an antiferromagnet (AFM), the direct coupling at the FM-AFM interface may induce an antiparallel alignment of the ferromagnet with the first monolayer of the antiferromagnet. Considering FM-AFM-FM trilayers grown under sufficiently good conditions, the single monolayers of the antiferromagnetic interlayer are ordering ferromagnetically with an antiparallel alignment of neighbouring layers, as shown in fig. 2.5(c). Thus the monolayers of the antiferromagnet show an alternating magnetic orientation. Due to the direct exchange coupling at the FM-AFM interface the relative orientation of the two FM films depends on the number of AFM monolayers in between, yielding a parallel alignment for an odd number and antiparallel alignment for an even number of AFM monolayers, respectively. This phenomenon being referred to as *proximity magnetism*

has been observed in antiferromagnetic Cr and Mn films when layer-by-layer growth was achieved (see SLONCZEWSKI, 1995; BÜRGLER & GRÜNBERG, 2005).

2.3.3 Interlayer exchange coupling

With the availability of ultra-high vacuum film deposition machines epitaxial growth of magnetic thin films became feasible and led to the discovery of the *interlayer exchange coupling* (GRÜNBERG *et al.*, 1986). This type of coupling oscillates periodically between parallel and antiparallel alignment of the magnetization in the two layers as the interlayer thickness is varied (PARKIN *et al.*, 1990). The oscillation of the coupling parameter J_1 can be explained by the existence of spin-dependent standing electron waves in the nonmagnetic interlayer due to the spin-split density of states in the two magnetic layers (STILES, 2004).

Due to imperfect match of the densities of states of two neighbouring materials electrons are partially reflected at the interfaces. In a ferromagnet the reflectivity of electrons at a non-metal/ferromagnetic interface becomes spin-dependent due to the spin-split density of states. If the electrons in the spacer material are reflected on both interfaces they are confined to the interlayer and a *quantum well state* is formed. In a simplified model following BÜRGLER *et al.* (2001) the electronic states are spin-polarized standing waves similar to electronic states in an one-dimensional potential well (SCHWABL, 1992). The condition to form a standing wave in a potential well with thickness D is

$$2|\boldsymbol{k}_\perp^{(n)}| = n\frac{2\pi}{D}. \tag{2.20}$$

These quantum well states correspond to discrete energy levels with

$$\epsilon_n = \frac{\hbar^2}{2m}\left(\boldsymbol{k}_\perp^{(n)}\right)^2 = n^2\frac{\hbar^2\pi^2}{2mD^2}. \tag{2.21}$$

Thus the total energy is

$$E_{\mathrm{QW}} = \sum_{n,\epsilon_n<E_F} \epsilon_n. \tag{2.22}$$

When increasing the spacer thickness D, the energy levels of the electronic states move downwards on the energy scale and each time when another level crosses the Fermi energy E_F the corresponding states are populated and the total energy is increased step-like. When D is increased further, E_{QW} is decreasing again, until the next level crosses E_F. Therefore, an oscillatory behaviour of E_{QW} is obtained.

Looking at the density of states of a typical system of two magnetic films of a *3d* metal separated by a spacer material made of a noble metal, as shown in fig. 2.6, it can be clarified that the quantum well state does only exist for spin-down electrons in parallel alignment of the two magnetic films. For anti-parallel alignment only one potential

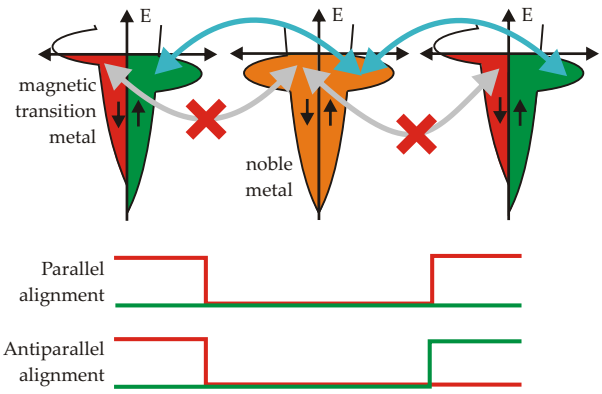

Figure 2.6: Top: Schematic DOS of parallel aligned magnetic transition metals and a nonmagnetic noble metal. Bottom: Schematic potential steps as seen by spin-up electrons (green) and spin-down electrons (red) for parallel and antiparallel aligned magnetic layers, respectively.

step exists for both types of electrons. So only the energy of a parallel coupled system oscillates, while the energy of the antiparallel coupled system does not show this oscillatory behaviour. Thus, the energy difference $\Delta E = E_{\uparrow\uparrow} - E_{\uparrow\downarrow}$ oscillates between positive and negative values when varying D, indicating regions of parallel and antiparallel coupling as shown in fig. 2.7(a). The oscillation period λ_D follows from eq. (2.20) with $\Delta n = 1$:

$$\lambda_D = \frac{2\pi}{2|\boldsymbol{k}_\perp|}. \tag{2.23}$$

In a 3D model the wavevector $\boldsymbol{k}_\perp$ is the component of a Fermi wave vector $\boldsymbol{k}_F$ perpendicular to the interface planes. The parallel component $\boldsymbol{k}_\parallel$ is conserved during the reflection process, while $\boldsymbol{k}_\perp$ is reversed to $-\boldsymbol{k}_\perp$. $\boldsymbol{k}_\perp$ can be found graphically from a cross-section through the Fermi surface under the condition that critical spanning-vectors $\boldsymbol{q_i}$ exist with an orientation perpendicular to the interface planes and to the Fermi surface connecting two Fermi wave vectors with the same $k_\parallel$ and opposite $k_\perp$. Then the oscillation period is given by

$$\lambda_D = \frac{2\pi}{|\boldsymbol{q}|} \tag{2.24}$$

By backfolding $\boldsymbol{q}$ into the first Brillouin zone an oscillation period larger than the lattice parameter is ensured. For the case of copper with the interface oriented in the (001) plane the Fermi surface is depicted in fig. 2.7(b). There are two critical spanning vectors $q_{1,2}$ giving rise to a superposition of two oscillation periods $\lambda_{D,i} = 2\pi/q_i$. The example of copper has been chosen due to the relatively simple shape of the Fermi surface. However, the model also works for materials with more complicated Fermi surface, e.g. for chromium (ZABEL, 1999).

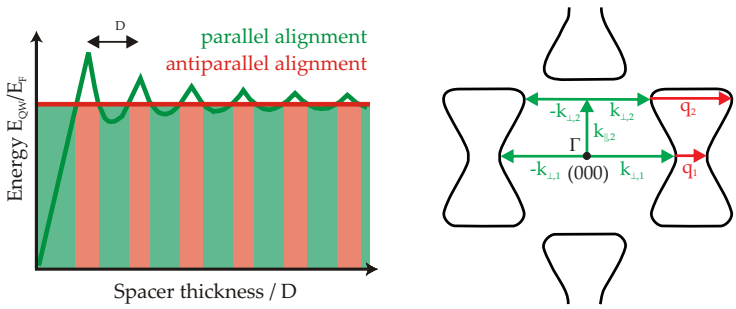

Figure 2.7: (a) Normalized quantum well energy E_{QW}/E_F against spacer thickness D. The oscillation of the energy for parallel alignment leads to alternating parallel and antiparallel alignment (after BÜRGLER & GRÜNBERG, 2005). (b) Schematic Fermi surface of copper with two critical spanning vectors in [001] direction (after BÜRGLER *et al.*, 2001). The Fermi wavevectors $\pm\boldsymbol{k}_{\perp,i}$ (green) are depicted together with their corresponding critical spanning vectors $\boldsymbol{q}_i$ (red).

2.3.4 Biquadratic coupling

In sample regions with weak bilinear coupling, magnetization configurations with perpendicular orientation due to the biquadratic coupling term are observed. Experimentally J_2 was found to be always negative favouring perpendicular coupling. A variety of interpretations of biquadratic coupling exists:

- SLONCZEWSKI (1991) attributed it to a fluctuation mechanism leading to a frustration of bilinear coupling. Due to an inhomogeneous spacer thickness distribution the bilinear coupling strength $J_1(D)$ oscillates over a range of ΔJ_1 over the distance L. If J_1 fluctuates between positive and negative values, alternating regions of parallel and antiparallel coupling are formed. For a distance L smaller than the exchange length given in eq. (2.9) the magnetization cannot react on fluctuations by creating domains of different alignment. It can be shown that the minimization of the sum of exchange and coupling energy then leads to bilinear coupling with
$$J_2 \propto -\frac{(\Delta J)^2 L}{A}. \tag{2.25}$$
- In the "loose spin" model magnetic impurities inside the spacer material are held responsible for the biquadratic coupling term (SLONCZEWSKI, 1993). The magnetic impurities are only weakly coupled to the magnetic layers by indirect exchange coupling via the electrons in the spacer layer. A single loose spin is always bilinearly coupled to the adjacent magnetic films. For a collection of spins at different positions these bilinear contributions may cancel out giving

rise to a dominant biquadratic coupling. Since the single spins do not exhibit a direct exchange coupling their alignment is not very stable against thermal fluctuations. Thus the biquadratic coupling due to loose spins is subject to a strong temperature dependence.

- DEMOKRITOV *et al.* (1994) proposed a different mechanism for the biquadratic coupling due to magnetic dipole interaction. While correlated interface roughness can lead to bilinear orange-peel coupling, as previously discussed, it can be shown that uncorrelated roughness induces biquadratic coupling.
- Furthermore, it has been shown that the competition between parallel pinhole coupling and antiparallel interlayer exchange coupling also induces biquadratic coupling (BOBO *et al.*, 1999).

The variety of these models shows that the occurrence of biquadratic interlayer coupling may depend on many different factors. The origin of biquadratic coupling in a given system can only be ruled out by the variation of different conditions such as temperature or interface roughness.

2.4 Magnetic domains

The free energy of a ferromagnetic system is given by the energy terms introduced in the above sections. In an external field $\boldsymbol{H}_{ex}$, the free energy takes the form:

$$\begin{aligned} F_{\text{Ferromagnet}} =& F_{\text{exc}} + F_{\text{MCA}} + F_{\text{demag}} + F_{\text{coupl}} + F_{\text{ext}} \\ =& A \int_V (\boldsymbol{\nabla} \cdot \boldsymbol{m})^2 \, \mathrm{d}V + \int_V f_{\text{ani}} \mathrm{d}V - \frac{\mu_0}{2} \int_V \boldsymbol{H_d} \cdot \boldsymbol{M} \mathrm{d}V \\ &+ \int_A \sigma_{\text{coupl}} \mathrm{d}A - \mu_0 \int_V \boldsymbol{H}_{\text{ex}} \cdot \boldsymbol{M} \mathrm{d}V \end{aligned} \tag{2.26}$$

with V denoting an integration over the whole sample volume and A an integration over the interface area (HUBERT & SCHÄFER, 1998).

The equilibrium configuration $\boldsymbol{M}(\boldsymbol{r})$ is given by the minimum of (2.26). Most of the energy terms favour a homogeneous alignment of the magnetization throughout the entire sample. The interaction with the demagnetizing field for such a configuration will increase the F_{demag}-term. To reduce this energy contribution, the magnetization will split up into multiple *domains* of homogeneous magnetization being separated by *domain walls* of several nm thickness, which describe a region with a continuous rotation of the magnetization. Depending on the influence of the shape anisotropy the magnetization in the domain walls can be oriented out-of-plane (*Bloch walls*) or purely in-plane (*Néel walls*). The two domain wall types are illustrated in fig. 2.8.

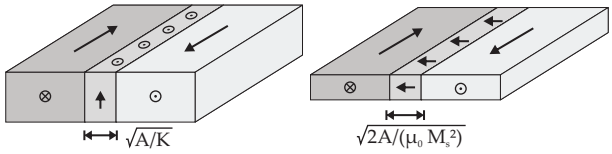

(a) Bloch wall (b) Néel wall

Figure 2.8: Domain wall configurations with (a) out-of-plane magnetization (Bloch wall) and (b) in-plane magnetization (Néel wall).

As stated in sect. 2.2 the typical length scale over which the magnetization may change is the exchange length $l_{\text{exc}} = \sqrt{A/K}$. This is also the typical order of the domain wall thickness (HUBERT & SCHÄFER, 1998). In the bulk the exchange length is dominated by the magnetocrystalline anisotropy K and $l_K = \sqrt{A/K}$ becomes the typical width scale of a Bloch wall. In thin films, it is dominated by the stray field anisotropy K_s thus the exchange length is given by

$$l_s = \sqrt{A/K_s} = \sqrt{2A/\mu_0 M_s^2} \tag{2.27}$$

which is the length scale of the width of a Néel wall. Typical values for iron are $l_s = 3.3\,\text{nm}$ and $l_K = 21\,\text{nm}$, respectively (KRONMÜLLER & FÄHNLE, 2003). The relation between wall width and film thickness is determining the type of wall. As a rule of thumb, a wall can be assumed of Bloch type if the film thickness is larger than the wall width and it is of Néel type if the film thickness is smaller (HERTEL, 2009).

The last term in (2.26) denotes the Zeeman energy due to the interaction of the magnetization with an external field. When the external field is varied, the energy is changed and a new equilibrium configuration $\boldsymbol{M}(\boldsymbol{r})$ is obtained by domain wall motion and rotation of the magnetization. However, usually the obtained equilibrium configuration marks a local energetic minimum and does strongly depend on the history of the micromagnetic configuration.

Typical ground state configurations of the magnetization in thin film elements are shown in fig. 2.9. They have been generated by the OOMMF micromagnetic framework (DONAHUE & PORTER, 1999) for a 2x1 µm^2 Permalloy element, reproducing domain patterns shown by RAVE & HUBERT (2000). Due to the minimization of the demagnetizing field, in all configurations the rim magnetization is parallel to the edges. While (a) and (b) show high remanence states with the magnetization parallel to the long edge, the other configurations are macroscopically demagnetized. All the states shown in fig. 2.9 have been acquired using the same simulation parameters and only depend on their micromagnetic history. Due to the shape anisotropy the magnetization tends to lie in the plane generating Néel domain walls, but configurations (c), (d) and (e) contain singularities where a continuous in-plane rotation of the magnetization is not possible. These regions with the magnetization circulating around the centre or regions with head-to-head/tail-to-tail configuration (in the centre of (d)) are referred to as vortices or anti-vortices, respectively. At the vortex/anti-vortex core (the centre) the magnetization is rotated out of the sample plane.

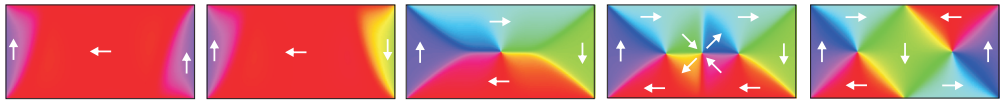

(a) C-state (b) S-state (c) Landau state (d) Cross-tie state (e) Diamond state

Figure 2.9: Magnetization ground-state configurations of a 2 μm x 1 μm Permalloy rectangle. The images have been generated by the OOMMF framework (DONAHUE & PORTER, 1999).

2.5 Magnetization dynamics

The temporal development of a magnetic moment $\boldsymbol{\mu}(t)$ in an external magnetic field $\boldsymbol{H}(t)$ is given by the *Landau-Lifshitz* equation of motion

$$\frac{\mathrm{d}\boldsymbol{\mu}(t)}{\mathrm{d}t} = -\gamma\boldsymbol{\mu}(t) \times \boldsymbol{H}(t) \tag{2.28}$$

with the gyromagnetic ratio $\gamma = \frac{ge}{2m}$, where g is the gyromagnetic splitting factor. For a free electron with $g = 2.002$ the gyromagnetic ratio is $\gamma = 1.78 \times 10^{11}\,1/(\mathrm{Ts})$. In the solid state the external magnetic field $\boldsymbol{H}$ has to be replaced by an effective magnetic field $\boldsymbol{H}_{\mathrm{eff}}(t)$ considering all internal and external contributions and the magnetic moment is replaced by the macroscopic magnetization $\mu_0\boldsymbol{M}(\boldsymbol{r})$ (HEINRICH & COCHRAN, 1993). The effective field is given by the derivative of the free energy density $f(\boldsymbol{M})$ from eq. (2.26)

$$\mu_0\boldsymbol{H}_{\mathrm{eff}} = \frac{\mathrm{d}f(\boldsymbol{M})}{\mathrm{d}\boldsymbol{M}} \tag{2.29}$$

and thus the *Landau-Lifshitz*-equation for a macroscopic sample becomes

$$\frac{\mathrm{d}\boldsymbol{M}(t)}{\mathrm{d}t} = -\gamma\mu_0\boldsymbol{M}(t) \times \boldsymbol{H}_{\mathrm{eff}}(t). \tag{2.30}$$

Eq. (2.30) states that a magnetic field forces the magnetization to precess around the effective field with a frequency given by the applied field. The magnetization is never aligning parallel to $\boldsymbol{H}$ as indicated in fig. 2.10(a). Experimentally it can be shown that for a constant field $\boldsymbol{H}$ the precessional motion of $\boldsymbol{M}(t)$ relaxes to a stable equilibrium direction (fig. 2.10(b)). This effect due to energy dissipation can be considered by introducing an ohmic dissipation term

$$\boldsymbol{H}_{\mathrm{diss}} = -\alpha\frac{1}{\gamma\mu_0 M_S}\frac{\mathrm{d}\boldsymbol{M}}{\mathrm{d}t} \tag{2.31}$$

with the phenomenological GILBERT damping parameter α (2004). Inserting (2.31) in (2.30) yields the *Landau-Lifshitz-Gilbert* equation of magnetization motion

$$\frac{\mathrm{d}\boldsymbol{M}(t)}{\mathrm{d}t} = -\gamma\mu_0\boldsymbol{M}(t) \times \boldsymbol{H}_{\mathrm{eff}}(t) + \frac{\alpha}{M_S}\left(\boldsymbol{M}(t) \times \frac{\mathrm{d}\boldsymbol{M}(t)}{\mathrm{d}t}\right). \tag{2.32}$$

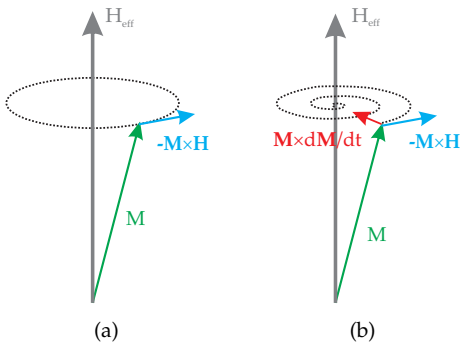

Figure 2.10: (a) Illustration of the Landau-Lifshitz equation without considering damping. $\boldsymbol{M}$ is rotating at constant radius around $\boldsymbol{H}$ (dotted line). (b) The Gilbert damping term leads to an additional component moving $\boldsymbol{M}$ towards the direction of $\boldsymbol{H}$ on a spiral path.

2.5.1 Uniform magnetization precession

In general $\boldsymbol{M}$ and $\boldsymbol{H}_{\text{eff}}$ are spatially inhomogeneous and eq. (2.32) has to be solved in a continuum approximation. For a soft magnetic thin film, however, the magnetization can be assumed homogeneous throughout the whole film and neglecting damping eq. (2.30) can be solved regarding only a single *macrospin* $\boldsymbol{M}$. In that case the angular frequency of the uniform precession mode is given by the KITTEL equation (1948)

$$\omega_0 = \mu_0 \gamma \sqrt{(H_{\text{eff}} + M_S) \cdot H_{\text{eff}}} \tag{2.33}$$

considering the effective field $\boldsymbol{H}_{\text{eff}}$ in the sample plane consisting of the external field H_{ext}, the anisotropy field H_{MCA}, the demagnetizing field H_{demag} and the coupling field H_{coupl}. The form of eq. (2.33) shows that even for zero external field $H_{\text{ext}} = 0$ precessional motion around an internal effective field can be observed. Thus, after excitation with short magnetic field pulses the precessional relaxation of $\boldsymbol{M}$ can be investigated. For typical element sizes with lateral dimensions in µm range and thickness in the nm range the precessional frequencies range between 1-10 GHz. The characteristic damping time τ is given by (MILTAT *et al.*, 2002)

$$\tau = \frac{2}{\alpha \gamma \mu_0 M_S}. \tag{2.34}$$

2.5.2 Domain wall motion

In an external magnetic field ferromagnets are lowering their Zeeman energy by maximizing the volume with the magnetization oriented parallel to the external field. This can be achieved by a rotation of the total magnetization towards the field. However, due to anisotropy constricting the magnetization to particular directions this is not always possible. Another way to lower the Zeeman energy is the growth of domains aligned parallel to the field by the motion of domain walls. Regarding the speed of

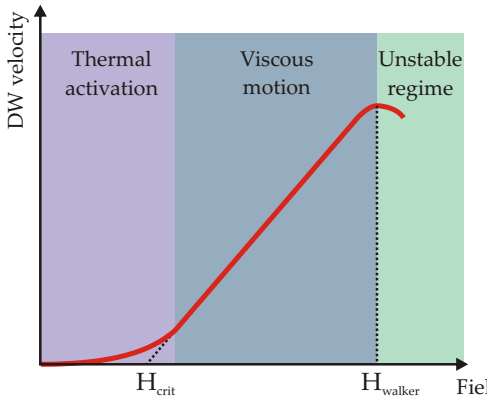

Figure 2.11: Illustration of the different regimes of domain wall motion.

such processes three different regimes can be identified, as depicted in fig. 2.11. When the external field H is lower than a critical field H_{crit}, domain walls are propagating by successive thermally activated jumps with small volumes switching at once. The smallest volume in which the magnetization reverses by one jump, is the Barkhausen volume V_B. For reversing V_B the energy barrier E_B has to be overcome. Then the speed of wall motion can be described by

$$v = \sqrt[3]{V_B}/\tau \exp\left(\frac{\mu_0 M_S H V_B - E_B}{k_B T}\right) \tag{2.35}$$

with a time constant τ of the order of 10^{-9}s (LEE *et al.*, 1999).

When the critical field H_{crit} is exceeded, pinning at defects does not play a role anymore and the domain wall motion enters the viscous regime with (FERRÉ, 2002)

$$v = \mu\mu_0(H - H_{\text{crit}}) \tag{2.36}$$

with a constant domain wall mobility

$$\mu = \gamma\Delta/\alpha \tag{2.37}$$

depending on the domain wall width Δ and the damping coefficient α.

At even higher fields it has been found that the domain wall velocity enters a plateau or oscillates with increasing field. Beyond the critical field no steady state solution for the domain wall motion exists and the wall magnetization is freely precessing and cycling periodically through Bloch and Néel configurations, while the wall oscillates back and forth (HUBERT & SCHÄFER, 1998). SCHRYER & WALKER (1974) have calculated the breakdown field for Bloch walls as

$$H_W = \frac{\alpha}{2} M_S. \tag{2.38}$$

This field is referred to as the *Walker limit*.

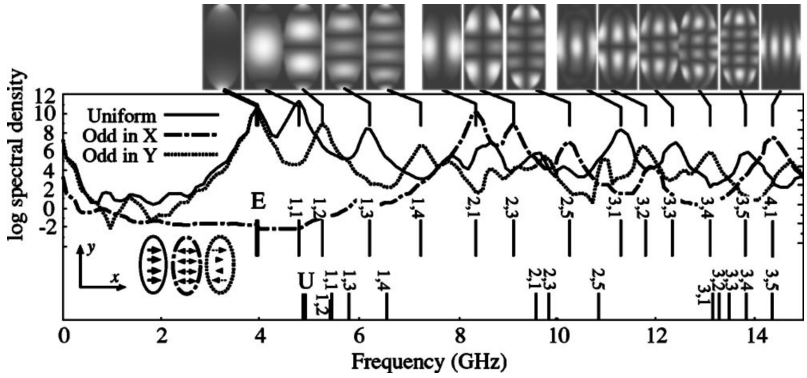

Figure 2.12: Frequency-spectrum and images showing the spatial distributions of eigenmodes in a 160 nm × 3350 nm × 35 nm ellipse of Permalloy in zero applied field. The calculated mode frequencies (centered) are compared with frequencies calculated from a spinwave dispersion relation (bottom). (Taken from MCMICHAEL & STILES, 2005)

2.5.3 Oscillatory eigenmodes

In submicron sized samples the effect of the demagnetizing field becomes stronger and spatially inhomogeneous. Therefore the assumption of a coherent rotation of the magnetization is not valid anymore. Instead higher-order modes of oscillations with different oscillation frequencies and spatially inhomogeneous power distributions are excited. For a theoretical treatment eq. (2.32) has to be solved in a continuous approximation with spatially varying magnetization $\boldsymbol{M}(\boldsymbol{r})$ and fields $\boldsymbol{H}_i(\boldsymbol{r})$ with proper boundary conditions (see MILTAT *et al.* (2002) for a review). The observed eigenmodes include normal modes similar to the vibration of a fixed string (MCMICHAEL & STILES, 2005; ADAM *et al.*, 2007), domain wall modes (PARK *et al.*, 2003) and the gyrotropic motion of a vortex core (CHOE *et al.*, 2004).

While by spatially integrating methods a superposition of different modes is measured, experimental methods with spatial resolution like the PEEM technique can be used to directly visualize and distinguish the different modes. However, for the interpretation of such image series a knowledge of the time and length scales of the various processes is important. A short overview will be given in the following and in fig. 2.13:

Vortex precession and domain wall modes: The motion of micromagnetic features as domain walls or vortices is the slowest process observed in small magnetic elements. Typical resonance frequencies are of the order of several 100 MHz (IVANOV & ZASPEL, 2004), the observed velocities are of the order of 500 m/s (RAABE *et al.*, 2005). Thus displacement amplitudes around 1 µm are reached.

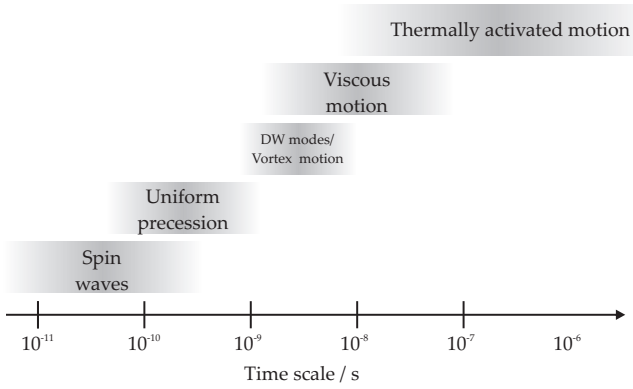

Figure 2.13: Typical timescales of different processes in magnetization dynamics.

Uniform magnetization precession: The frequency of the uniform mode depends on the internal effective field. It is dominating when the effective field can be assumed homogeneous over the element. The frequency can be calculated by the Kittel formula eq. (2.33). With typical magnetization values of the order of $\mu_0 M_s = 1.0\,\mathrm{T}$ and internal fields of $\mu_0 H_{\mathrm{eff}} = 1\,\mathrm{mT}$ (depending on the element dimensions) the frequency of the uniform mode is of the order of 1 GHz. Considering also magnetocrystalline anisotropy and coupling effects the effective field is increased and the uniform mode reaches frequencies of 10 GHz. In the case of uniform precession the magnetization rotates coherently over the whole domain (several µm).

Non-uniform modes: A variety of non-uniform oscillatory modes is displayed in fig. 2.12. The frequency is determined from the number of nodes of the oscillation and can be estimated from the Kittel equation with a wave number dependent demagnetizing factor (McMichael & Stiles, 2005). The frequency goes from the range of the uniform mode up to one order of magnitude higher.

Spin waves: Several authors report the excitation of spin waves in small magnetic elements (Perzlmaier *et al.*, 2008; Wegelin *et al.*, 2007). Spin wave packets have been observed with travelling velocities on the order of 10 km/s and a typical width below 1 µm.

Chapter 3

Experimental methods

This chapter deals with the experimental methods used for the investigation of magnetic heterostructures. We have employed the method of *Time-Resolved X-ray Magnetic Circular Dichroism Photoemission Electron Microscopy*, that can be abbreviated as TR-XMCD-PEEM. In this chapter I will go through all the letters of this acronym: Starting with the X (Generation of X-rays), I will introduce the XMCD-effect (X-ray Magnetic Circular Dichroism) giving access to the imaging of magnetic domains and discuss its application in PEEM (Photoemission Electron Microscopy) and finally explain how TR (time resolution) enters the PEEM using a stroboscopic pump-probe approach.

3.1 X – Generation of X-rays

More than 100 years after their discovery by RÖNTGEN (1898), which was honoured by the first Nobel Prize in physics in 1901, X-rays are nowadays an important tool in many scientific disciplines like chemistry, physics, biology, medicine and even art (BALL, 2008) and archaeology (PANTOS, 2005). X-rays are generated either by the acceleration of charged particles (*Bremsstrahlung*), by the excitation of electronic transitions in atoms (*characteristic X-rays*) or by the peeling of adhesive tape, as shown by CAMARA *et al.* (2008).

It is known from classical electrodynamics that accelerated charged particles are emitting radiation (FLIESSBACH, 1994; JACKSON, 1998). For particles moving with a constant velocity $|\boldsymbol{v}|$ on a circular path the acceleration is always perpendicular to $\boldsymbol{v}$. In the classical limit the radiation field has a $\sin^2\Theta$ dependence with the angle Θ relative to the acceleration direction $\dot{\boldsymbol{v}}$. For relativistic particles with $v \sim c$ the opening angle of the radiation cone decreases to $\Theta \approx 2/\gamma$ with $\gamma = 1/\sqrt{1 - v^2/c^2}$. For typical electron energies of modern synchrotron facilities of the order of several GeVs, the

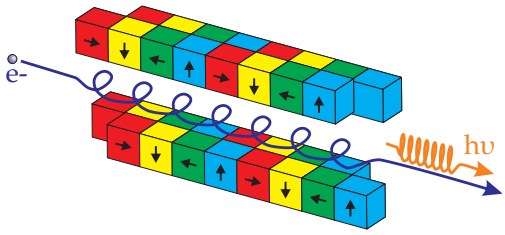

Figure 3.1: Illustration of the trajectory of an electron in an undulator. The arrows are symbolizing the orientation of the periodically arranged magnets. The electron is moving on a helical path giving rise to the emission of circularly polarized light.

opening angle is in the range of 0,1 mrad. The frequency spectrum of the emitted synchrotron radiation is determined by the finite X-ray pulse length Δt as seen by an observer outside of the ring through a small aperture. The typical width of the emitted radiation spectrum is given by

$$\omega = \frac{1}{\Delta t} = 3\gamma^2\omega_0 \tag{3.1}$$

with the cyclotron frequency $\omega_0 = v\gamma/\rho$ of the circulating electrons at a radius ρ (STÖHR & SIEGMANN, 2006).

For magnetic measurements not only the energy tunability but also the variation of the polarization of the photon beam is mandatory. The polarization is closely connected to the angular momentum of the circulating electrons. When a photon is emitted from the rotating electrons, energy and angular momentum is transferred to the generated photons. With the angular momentum $\boldsymbol{L}$ of the circulating electrons oriented perpendicular to the rotating plane (down for the typical clockwise rotational sense), photons emitted in the rotation plane have no projection of $\boldsymbol{L}$ on their propagation vector and thus their angular momentum L_z is zero. Therefore the emitted radiation is linearly polarized in the rotation plane. For radiation emitted below or above the orbit plane $\boldsymbol{L}$ has a finite projection $L_z = \pm\hbar$ along the propagation direction z. Hence the emitted radiation is left- (emission above orbital plane) or right-circularly (emission below orbital plane) polarized.

While in the beginning of the synchrotron era, synchrotron radiation was only an unwanted mechanism of energy loss, soon it became clear that the properties of the synchrotron radiation, such as a broad frequency spectrum, render it an outstanding tool for investigations in solid state or atomic physics. After parasitic use of the synchrotron radiation in first generation sources dedicated to particle physics, the storage rings of the second generation were designed especially for experiments with synchrotron radiation. In a third step, so-called *insertion devices* have been constructed modulating the electron trajectories for an increased flux and improved polarization selection. Undulators as typical insertion devices are consisting of periodic arrays of permanent magnets inducing small periodic modulations of the circular trajectory of the electrons (see fig. 3.1). Due to interference of the photon fields emitted from the individual undulator periods the frequency spectrum of an undulator exhibits a structure of peaked harmonics. The position of the peak energies of an undulator can

be tuned by changing the distance between the opposing magnet arrays. By shifting the different magnet arrays relative to each other, the electrons can be forced to sinusoidal or helical trajectories allowing for variable polarization. A sinusoidal modulation of the electron trajectory in (perpendicular to) the orbit plane leads to horizontal (vertical) linear polarization of the X-rays, while by a helical path circularly polarized X-rays are generated. For a review see ATTWOOD (2007) or CRAMM (2007).

3.2 XMCD – X-ray Magnetic Circular Dichroism

The word *dichroism* is of greek origin and means "two colours". *X-ray magnetic circular dichroism* (XMCD) describes the dependence of the absorption coefficient μ in magnetic materials on the state of circular polarization. It was found that the absorption of circularly polarized light contains contributions proportional to the projection of the light helicity vector on the spin and orbital moment, changing sign when either light helicity or magnetization is flipped. Thus, the first experimental observation of XMCD by SCHÜTZ *et al.* (1987) at the iron K-edge marks the onset of a new era in magnetic spectro- and microscopy, since it became possible to study the magnetic properties such as the spin and orbital magnetic moment of a material element-selectively. The element-selectivity is given by the fact that the measurements are carried out with the photon energy tuned to a characteristic absorption edge of one element. Therefore, only the magnetic moments of that particular element are selectively probed.

Two properties are important for the XMCD effect: A spin or orbitally polarized electronic transition process and an exchange-split density of states yielding magnetization-dependent transition probabilities. Formally, these conditions are properties of the particular transition process. For the typically considered $2p \rightarrow 3d$ transitions, however, these conditions are separately fulfilled by the spin-orbit split initial states and the exchange-split final states (see fig. 3.2). Due to that fact, this process is often referred to as a "two-step-process" (e.g. STÖHR & SIEGMANN, 2006).

The XMCD effect is based on the absorption of circularly polarized photons by core-level electrons. During that process the photon energy and its angular momentum $\pm\hbar$ are transferred to the corresponding electron. Conservation of angular momentum leads to the optical selection rules of the transition $\Delta m_s = 0$ and $\Delta m_l = +1$ for right-circularly and $\Delta m_l = -1$ for left-circularly polarized light, respectively. Formally, the transition rate due to X-ray absorption is given by Fermi's golden rule

$$I_{\text{abs}} = \sum_{i,f} \mathcal{A} \left| \langle f | \boldsymbol{e} \cdot \boldsymbol{r} | i \rangle \right|^2 \delta(\hbar\omega - (E_f - E_i)) \tag{3.2}$$

with a normalization factor $\mathcal{A}$ and the corresponding transition matrix element of the dipole operator $\boldsymbol{e} \cdot \boldsymbol{r}$. The sum is carried out over all unoccupied final states f and occupied initial states i. After determining the relative weight of the $|l, m_l, s, m_s\rangle$

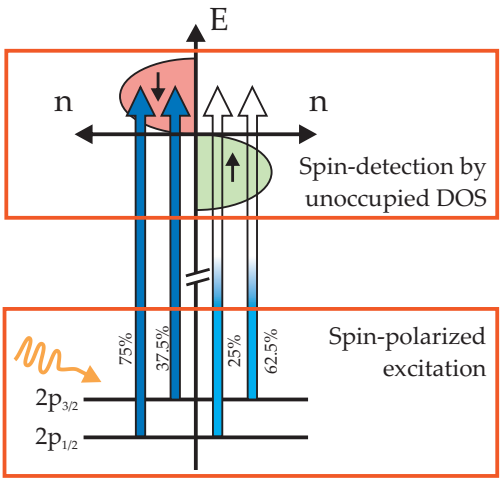

Figure 3.2: Illustration of the transition probabilities for the spin-polarized $2p_{1/2} \rightarrow 3d$ and $2p_{3/2} \rightarrow 3d$ transition probabilities obeying the selection rules for right circularly polarized light $\Delta m_s = 0$ and $\Delta m_l = +1$. Due to the exchange-split density of the final states only transitions between the spin-down bands are allowed.

eigenfunctions in each level expressed with the spin-orbit coupled wave functions $|l, m_l, j, m_j\rangle$ by means of the Clebsch-Gordon coefficients, the single transition matrix elements can be calculated. Summing up the spin-dependent transition probabilities, by circularly right polarized light 75% spin-down (25% spin-up) electrons are excited at the L_2 edge ($2p_{1/2} \rightarrow 3d$) and 37.5% spin-down (62.5% spin-up) electrons at the L_3 edge ($2p_{3/2} \rightarrow 3d$). For the absorption of circularly left polarized light, the values for spin-down and spin-up electrons are interchanged. In the picture of the two-step-process, the absorption of the circularly polarized photon together with the spin-orbit coupling serves as a polarizer for the photoelectrons.

The sum in eq. (3.2) implicitly contains the density of the unoccupied final states. In magnetic materials exchange splitting leads to an asymmetric density of states. This imbalance is used to probe the spin polarization of the electronic transitions. Considering a metal with a completely filled spin-up band and an unoccupied spin-down band, as shown in fig. 3.2, only transitions to the spin-down band are allowed. This leads to the fact, that a flip of either the light polarization (switching the spin-polarization of the electronic transitions) or the the magnetization (switching the density of the final states), changes the absorption rate. The difference of the absorption intensities for right and left circularly polarized light $\sigma\pm$ is the XMCD intensity $I_{\mathrm{XMCD}} = I_{\sigma+} - I_{\sigma-}$. Due to the opposite spin polarization at the L_3 and L_2 transition, I_{XMCD} also has the opposite sign for both absorption edges.

The angular momentum of the photon $\pm\hbar$ is only partly transferred to the spin moment of the photoelectron. Thus, the $2p \rightarrow 3d$ transitions are not only spin-polarized, but also carry an orbital polarization. The orbital polarization of the photoelectrons leads to a dichroism which has the same sign for both L_2 and L_3 edges in contrast to the spin-polarized case. So-called sum-rules have been derived to calculate the orbital and spin moment of the sample independently by integrating over the dichroism

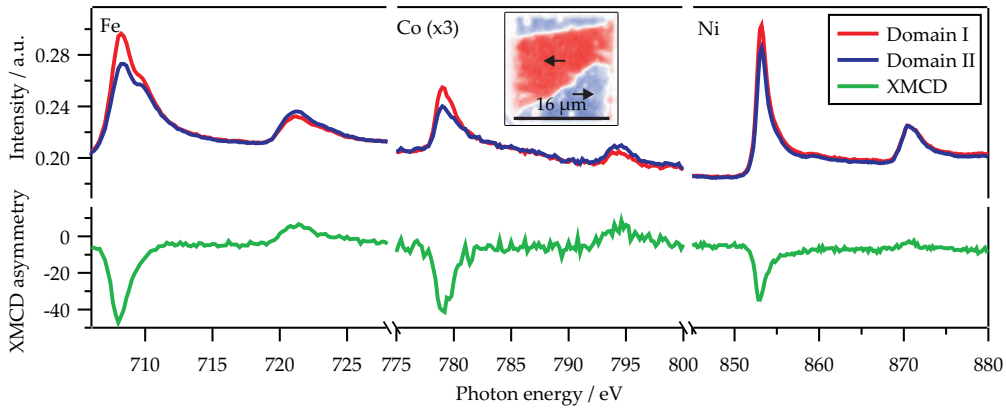

Figure 3.3: Typical X-ray absorption (top) and XMCD (bottom) spectrum of a sample incorporating Fe, Co and Ni. The spectrum has been acquired by taking PEEM images (see inset) at each photon energy step and integrating the intensity over two domains with opposite magnetization (red and blue area in the inset). For each element the XMCD asymmetry has the same characteristics with negative values at the L_3 and positive values at the L_2 absorption edges. This fact shows that the magnetization of all three elements is oriented parallel. The Co photoelectrons from the bottom layer of this heterostructure system exhibit more scattering events than the Fe or Ni photoelectrons yielding to an attenuation of the signal. Thus, the Co intensity has been up-scaled by a factor of three.

spectra in a suitable manner (THOLE *et al.*, 1992; CARRA *et al.*, 1993).

Experimentally, the X-ray absorption intensities are measured via the total electron yield (TEY) or fluorescence. After the absorption process, the core hole is filled either by a radiative X-ray fluorescence or a non-radiative Auger process. The high-energetic Auger electrons, the total number of which is proportional to the absorption rate, are passing through the solid suffering multiple inelastic scattering events leading to a cascade of secondary low-energy electrons. In TEY experiments they are extracted by an electrical field and the current of secondary electrons being proportional to the absorption rate is measured. A typical X-ray absorption and XMCD spectrum for two oppositely magnetized domains is shown in fig. 3.3. The spectra have been measured on two oppositely magnetized domains in a CoFe/Cr/NiFe trilayer. The XMCD spectra have the same characteristics for all three magnetic elements showing the parallel alignment of the Fe, Co and Ni magnetization. As the exact magnetization direction relative to the light incidence direction is not known, a quantitative analysis by the sum rules is not possible in this case.

The magnetic samples have been routinely investigated by the *magneto-optical Kerr effect* (MOKE) which was used for M(H) hysteresis measurements. In a MOKE set-up the rotation of the plane of polarization during the reflection of a laser beam on the sample surface is measured depending on the magnetization at the sample surface.

In a simplified picture the magneto-optical Kerr effect can be interpreted in terms similar to the XMCD effect (STÖHR & SIEGMANN, 2006): The incoming linearly polarized electromagnetic wave can be assumed as the superposition of two right- and left-circularly polarized waves. During the reflection process the laser light penetrates the sample on a length scale of 10-20 nm. Thereby, the polarization-dependent absorption of the magnetic materials leads to a different attenuation for the left- and right circularly polarized components yielding an effective rotation of the polarization plane of the re-composed linearly polarized wave. Quantum-mechanically it relates to spin-dependent transitions in the valence bands.

3.3 PEEM – Photoemission Electron Microscopy

Photoemission Electron Microscopy is a microscopy technique that is based on imaging the spatial photoelectron distribution onto a phosphorous screen with a magnification of about 10^3 - 10^4 in modern instruments. Having been developed back in the 1930s by BRÜCHE & JOHANNSON (1932) and BRÜCHE (1933), its relevance was growing fifty years later with the availability of high-brilliance synchrotron sources. Basically, a PEEM is imaging the spatial distribution of photoelectrons generated by incident photons. The illumination with UV light or X-rays gives rise to energy-dependent elemental contrast and polarization-dependent magnetic contrast. In 1987 PEEM images have been generated for the first time using tunable synchrotron radiation by TONNER & HARP (1988). A few years later the XMCD effect was exploited in PEEM image generation for the imaging of the magnetic domain structure in the bits of a magnetic recording disk (STÖHR *et al.*, 1993). By tuning the photon energy to the appropriate absorption edges element-selective magnetic microscopy can be carried out. Due to the photoelectron escape depth in the range of several nanometres it is even possible to study buried layers and interfaces. The combination of spatial resolution, photon energy tunability of the light source and real-time imaging makes PEEM an ideal tool for spectromicroscopic investigations of all kind. It has thus been used for the study of catalytic reactions (JAKUBITH *et al.*, 1990), the analysis of the spatial distribution of different elements in cosmic grains (BERNHARD *et al.*, 2006) and the reproduction of Fermi surfaces (KOTSUGI *et al.*, 2003).

A PEEM consists of a microscope column aligned perpendicular to the sample surface containing various electron-optical lenses (see fig. 3.4 for an illustration). The sample is typically mounted a few millimetres away from the first extractor lens. Between extractor and sample a voltage of several kilovolts is applied, accelerating the emitted electrons away from the sample into the microscope column. Due to the high field between extractor lens and sample the relative energy spread $\Delta E/E$ of the photoelectrons is reduced and the angular distribution is narrowed. Both effects reduce chromatic and spherical aberrations improving the spatial resolution of the instrument. Another measure for the improvement of resolution is the introduction of an

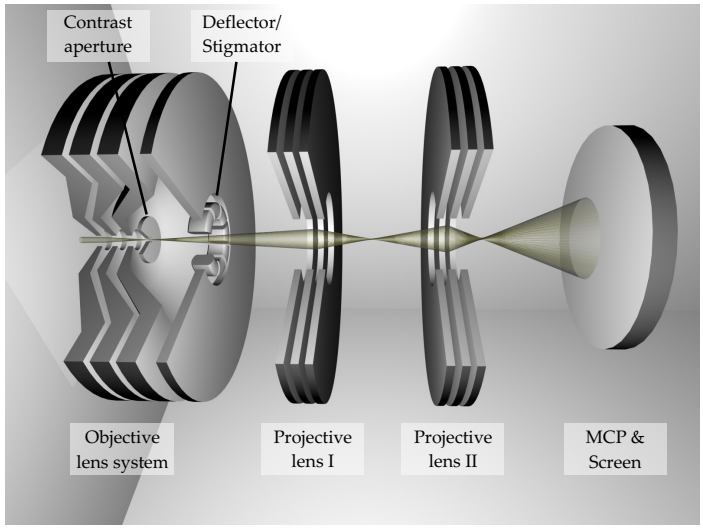

Figure 3.4: Illustration of the electron-optical column of a PEEM (from SCHNEIDER, 2005). The sample (left hand side) is magnified onto the phosphorous screen (right).

aperture in a focal plane of the microscope. The aperture serves as a cut-off for photoelectrons with trajectories far away from the optical axis, thus narrowing down angular and energetic distribution of the photoelectrons even more. An even better step for the reduction of aberrations of the extractor lens is the application of an electron mirror improving resolution without loss of intensity. With such aberration-corrected instruments the spatial resolution of current PEEMs in the range of 50-100 nm can be decreased to below 10 nm (BAUER, 2001).

The electron-optical lenses are either of electrical or magnetic type creating an axial symmetric electrical or magnetic field in the microscope column. Additional lens elements involve deflector/stigmator stages that are creating higher multipole field configurations correcting small misalignments of the microscope and the sample. One or two projective lenses are magnifying the projection of the photoelectron distribution once more, before they hit the image intensifier consisting of a multi channel plate (MCP) and a phosphor screen. The image generated on the phosphor is read out by a slowscan CCD camera.

Basically three different imaging modes can be discerned in the PEEM image generation (see fig. 3.5 for an illustration):

Threshold photoemission is the imaging mode that is available with low photon energy excitation sources as UV lamps or lasers. With photon energies slightly above the work function of the material, electrons from the Fermi level are excited above the vacuum level and travel with a kinetic energy of $E_{\mathrm{kin}} = h\nu - \Phi$ with the photon energy $h\nu$ and the work function Φ (EINSTEIN, 1905). Elemental and crystallographic contrast is achieved at positions with different work

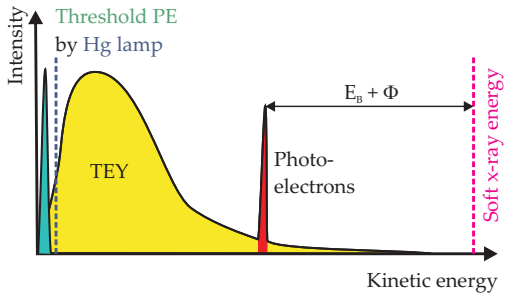

Figure 3.5: Kinetic energies of the photoelectrons in three different imaging modes. The coloured areas correspond to the measured intensities in a PEEM experiment, the dashed lines denote the photon energies of the incident light. In threshold photoemission by a Hg lamp (blue) only a narrow distribution of kinetic energies (green) is excited, in X-ray absorption measuring the total electron yield (TEY) all secondary electrons and the photoelectron peak are detected (yellow), while in an energy-filtered experiment the kinetic energy of the detected photoelectrons can be constricted to a small window (red).

functions, yielding only a qualitative information without the possibility of a chemical mapping.

X-ray absorption: Under the illumination with higher energetic X-rays at synchrotron sources also electrons from electronic states well below the Fermi level with a finite binding energy E_B are excited. The distribution of the kinetic energies of the photoelectrons is rather broad, not only containing primary photoelectrons with $E_{\text{kin}} = h\nu - E_B - \Phi$ but also lower energetic secondary electron cascades induced by emission and capture of Auger electrons (SCHNEIDER & SCHÖNHENSE, 2002). However, not the whole spectrum of kinetic energies is transmitted equally through the PEEM column, but the energy-dependent transmission of the PEEM limits the photoelectron contribution to lower energies (low pass). The photoelectron intensity is proportional to the energy-dependent absorption coefficient of the given material. Investigating transitions from elemental core levels to free electronic states above the Fermi level yields a strong elemental contrast providing the possibility to do a chemical mapping of the sample surface. The chemical sensitivity is demonstrated in fig. 3.3: Here the Fe absorption peak exhibits a splitting due to partial oxidation of the top layer. By independently selecting the photon energy of the Fe and the oxide peak, the spatial oxidation distribution can be imaged. All magnetic measurements shown in this thesis have been acquired using this mode.

Energy-filtered PEEM: For spectroscopic purposes it may be necessary to also filter the photoelectrons according to their kinetic energy. By such an approach the spatial distribution of photo- or Auger electrons belonging to one particular electronic state or transition can be imaged enabling for example the imaging in k-space (KOTSUGI *et al.*, 2003; KRÖMKER *et al.*, 2008). Also for experiments that rely on a constant excitation energy such as the standing wave experiments described in sect. 4.4 the option of energy filtering is mandatory if spectroscopic informations are also going to be obtained. Various approaches of energy-filtered

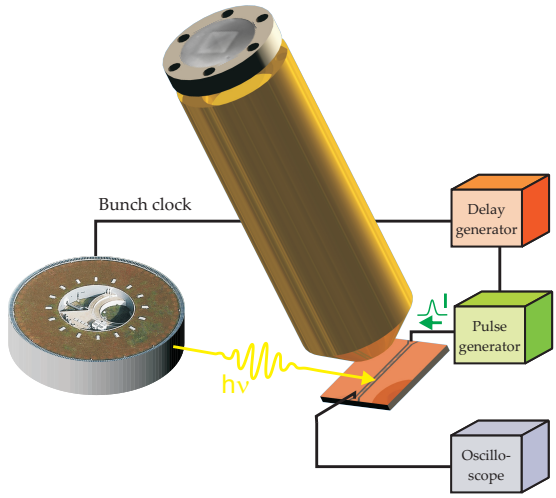

Figure 3.6: Illustration of the setup for the time-resolved imaging of magnetization dynamics. The samples are excited by an electrical pulse generator injecting current pulses into an coplanar waveguide giving rise to an in-plane magnetic Oersted field (pump). The pulse generator is frequency-matched to the synchrotron light pulses (probe). By shifting the delay between pump and probe pulse the temporal evolution of the magnetization dynamics can be studied.

PEEM enabling a different degree of energy resolution have been made such as retarding field analysers consisting of a grid with an applied voltage (MERKEL *et al.*, 2001), Ω-filters consisting of four 90°-deflectors (FINK *et al.*, 1997), single (BAUER, 2001) or aberration-corrected double (ESCHER *et al.*, 2005) hemispherical analysers.

Images of the local magnetization are acquired by exploiting the XMCD effect and recording images for left and right circularly polarized light. The XMCD asymmetry A_{XMCD} of the intensities for every pixel is calculated, being proportional to the projection of the light helicity vector $\boldsymbol{q}$ on the magnetization $\boldsymbol{M}$ (SCHNEIDER & SCHÖNHENSE, 2002):

$$A_{\mathrm{XMCD}} = \frac{I_{\sigma+} - I_{\sigma-}}{I_{\sigma+} - I_{\sigma-}} \propto \boldsymbol{q} \cdot \boldsymbol{M} \propto \cos(\angle(\boldsymbol{q}, \boldsymbol{M})) \tag{3.3}$$

with the measured intensity $I_{\sigma}\pm$ for right and left circularly polarized light, respectively. The element-selectivity of the XMCD effect yields XMCD-PEEM a suitable method for layer-resolved magnetization imaging in coupled heterostructures, allowing for microscopic studies of the coupling behaviour.

3.4 Time-Resolved PEEM of magnetization dynamics

By exploiting the temporal structure of a pulsed light source it is possible to carry out time-resolved pump-probe PEEM measurements. For such experiments the excitation-source (e.g. a laser or an electrical pulse generator) must be frequency-matched to the

light-source. Then, by shifting the delay between excitation (pump) and probe by the photoemission process, snapshots of the sample state can be made at certain moments after the excitation and so the temporal evolution is imaged. Different types of dynamics have been studied using time-resolved PEEM experiments, such as the micro-magnetic reaction on short field pulses (SCHÖNHENSE *et al.*, 2006b), thermally induced spin-reorientation (EIMÜLLER *et al.*, 2007) or the propagation of surface plasmons (BAUER *et al.*, 2007; MEYER ZU HERINGDORF *et al.*, 2007). Since the image is created from photoelectrons being only generated during illumination the temporal resolution in such stroboscopic experiments is given by the width of the light pulse, which is of the order of 30 ps for X-rays (from BESSY WEBSITE, 2009) and can be as short as several hundred attoseconds for specialized laser systems (STOCKMAN *et al.*, 2007).

In the experiments carried out for this thesis, the magnetization dynamics of µm-sized magnetic elements as a reaction to sub-ns magnetic field pulses has been studied. For this purpose a pump-probe-approach has been used employing metallic coplanar waveguides lithographically structured on the sample. The magnetic excitation is carried out by short Oersted-field pulses when a current pulse is passing through the waveguide. The magnetic microstructures on top of this waveguide are experiencing a periodic excitation by a magnetic field that is mainly oriented parallel to the sample surface and perpendicular to the direction of the current flow. The current pulse is generated by an external pulse generator connected with high-frequency compatible cabling to the sample. The pulse generator is pulsing with the same frequency as the synchrotron bunch repetition frequency at a variable delay before each light pulse, that can be adjusted by an external delay generator. For each investigated pump-probe delay PEEM images have been recorded with alternating illumination by right and left circurlarly polarized light and the corresponding XMCD asymmetry images have been generated showing the domain structure of the investigated element. By comparing XMCD images for different delays micromagnetic processes such as domain wall motion (FUKUMOTO *et al.*, 2006), magnetization rotation (KRASYUK *et al.*, 2005), the gyrotropic vortex motion (CHOE *et al.*, 2004) or the excitation of spin-waves (WEGELIN *et al.*, 2007) can be studied. The technical details of our set-up will be discussed in the next chapter.

Chapter 4

Methodical developments

An elementary part of this thesis has been devoted to the methodical improvement of the PEEM method for the studies of magnetic heterostructures. Before carrying out time-resolved PEEM measurements technical modifications had to be implemented into the measuring equipment. This chapter describes the technical implementation of the TR-PEEM method into the FOCUS IS-PEEM setup. The concept of deflection gating, which was developed for the realization of time-resolved measurements independent on the synchrotron working mode, will be introduced. Furthermore, the *SWEDGE* method (standing wave/wedge) was employed in PEEM measurements. This technique has been shown to yield depth resolution in photoemission spectroscopy experiments. By combining SWEDGE and PEEM the sample depth as a formerly missing degree of freedom can be made accessible in microscopic measurements, too. First experimental results will be presented.

4.1 Experimental setup

The underlying experimental setup is shown in fig. 3.6. The microscope which was used for the time-resolved measurements is a FOCUS IS-PEEM based on electrostatic lenses (FOCUS GMBH, 2001). In this instrument the sample is on ground potential and the photoelectrons are accelerated by a positive extractor voltage of up to 14 kV. The distance between sample and extractor is fixed, but the sample can be laterally positioned within a range of 5 mm in both directions. It is installed on a changeable sample holder which can be exchanged by an in-vacuum wobble stick without breaking the vacuum. Due to the direct attachment of the sample manipulator to the microscope column, movements of the sample relative to the microscope are effectively suppressed. The base pressure of the instrument is in the 10^{-9} mbar range.

Magnetic microstructures have been defined on the sample by optical lithography and Ar ion beam milling. In the experiments these structures have been excited by

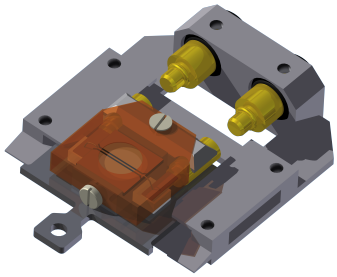

Figure 4.1: Illustration of the sample stage and sample holder with MMCX connectors. The sample is shielded by a copper sheet (drawn semi-transparent). The electrical contact of the sample has been achieved by wire-bonding.

magnetic field pulses around a metallic conductor due to short current pulses. In order to feed current pulses into the sample waveguide the sample holders had to be equipped with high-frequency compatible adapters and a corresponding counterpart had to be mounted at the stationary part of the sample stage together with high-frequency compatible cables. In order to retain the mounted sample stage and the option of in-vacuum sample transfer the load on the sample stage had to be minimized. Thus, weight and size of all components and the rigidity of the high-frequency cables had to be considered. We have used an approach based on the work of KRASYUK (2006) employing flexible sub-miniature cables (ELSPEC GMBH, 2007) and MMCX connectors with a maximum transmitted frequency of 6 GHz (DIN, 2002).

Sample holders and sample stage (see fig. 4.1) have been manufactured out of titanium in order to minimize the weight on the sample stage and to ensure an unmagnetic environment, since even small magnetic fields can deteriorate the image quality and spatial resolution of the instrument. The electrical contact of the coplanar waveguide has been achieved by wire-bonding. In a PEEM the sample itself is an important part of the objective lens system, since a deviation from axial-symmetry of the sample gives rise to distortions of the electrical field between extractor and sample degrading the image quality. Due to that fact and in order to avoid arking between protruding bonding wires and the extractor, the sample has been shielded by a thin copper sheet with a 5 mm opening. For facilitation of the sample transfer process the MMCX connectors have been mounted with flexible elastomer rings allowing for more tolerance of the sample positioning.

All cabling has been done by coaxial 50-Ohm cables to suppress damping of the excitation signal. For the generation of the input signal different pulse generators have been used depending on the required time- and voltage scales: We have used an *Agilent 81134A* together with a *Picosecond Pulse Labs 5865* amplifier for the generation of short rectangular pulses with rise and fall times below 100 ps, amplitude below 10 V and repetition rates up to 3 GHz and *Avtech AVMH-3/4* for the generation of Gaussian-shaped ns-long pulses with up to 100 V voltage and lower repetition rates in the MHz range. The pulse generators have been synchronized to the RF signal provided by the synchrotron, which can be delayed by a *Highland Technology HT400* delay generator. The RF line was 50-Ohm-terminated at the input of a fast oscilloscope where the

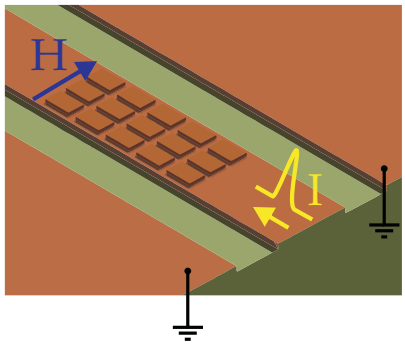

Figure 4.2: Schematic illustration of a coplanar waveguide (CPW) with magnetic microstructures deposited on top. The current pulse passes through the centre conductor while the outer planes are grounded. The impedance of the CPW depends on the dimensions and the dielectric constant of the substrate (green).

transmission of the excitation pulse was monitored.

4.2 Generation of magnetic fields pulses

The magnetic field pulses used for the excitation of magnetization dynamics in the ferromagnetic structures are generated by the Oersted field around a metallic conductor. The magnetic structures are deposited directly onto this metallic conductor. In order to reduce the dispersion of the current pulses all electrical lines have to be impedance-matched to 50 Ohms. The simplest way to achieve this by means of optical lithography is the *coplanar waveguide* (CPW) (WEN, 1969; SIMONS & WILEY, 2001). CPWs consist of a narrow metallic conductor between extended metallic ground planes, as illustrated in fig. 4.2. The impedance of a CPW depends on its dimensions and the dielectric constant of the substrate. Maximal frequencies of a CPW can be up to several THz, i.e. much higher than the frequency limit of the RF cables. Two propagating modes exist in a CPW with even and odd symmetry with respect to the centre conductor (GRIEBEL, 2002). While the odd mode includes only transverse field components, the even mode possesses strong longitudinal magnetic field components. With air-bridges or bonding wires the two ground-planes can be shorted and the even mode is suppressed. This step is crucial for the magnetodynamic studies in order to ensure a well-defined magnetic field direction.

The magnetic field around the coplanar waveguide can be calculated by the law of Biot-Savart (FLIESSBACH, 1994). Fig. 4.3 shows the in-plane and out-of-plane components of the magnetic field around a coplanar waveguide of 25 µm width and 200 nm thickness for a current of 100 mA. One can clearly see that the in-plane component can be assumed constant above the waveguide while the out-of-plane component shows a strong variation over the width of the conductor. However, above the middle of the waveguide the out-of-plane component is much smaller than the in-plane component and can thus be neglected.

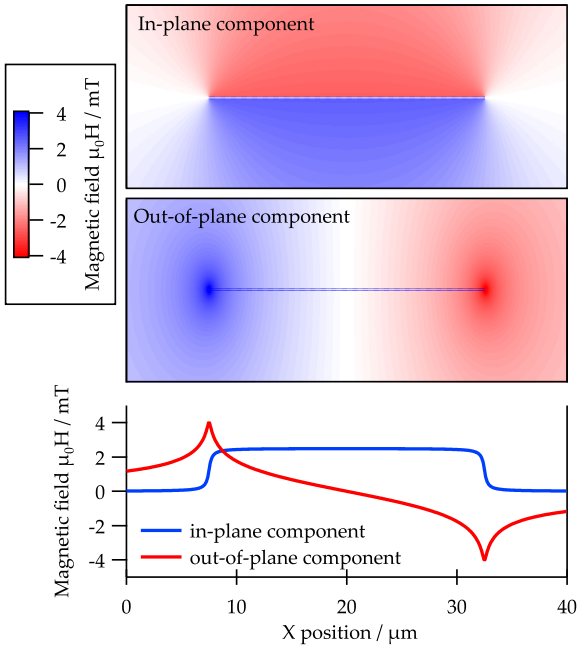

Figure 4.3: Magnetic field components perpendicular to the pulse propagation direction of a coplanar waveguide (25 µm width, 200 nm thickness) with a current of 100 mA obtained by numerical integration of the law of Biot-Savart. The cross-section of the CPW is indicated by the blue dotted box.

Throughout the magnetodynamic measurements the magnetic field calibration has been carried out as follows: In images taken before, at the same time of and after the field pulse the magnification of the image changes due to the voltage pulse propagating through the waveguide. The "breathing" of the images can be correlated with the transmitted voltage pulse as measured on the oscilloscope. Both measurements have the same shape (see fig. 4.4) and thus the magnetic field values can be calculated from the voltage profile, while the temporal position can be calibrated from the magnification curves. In previous works by VOGEL *et al.* (2004) the breathing and displacement of the PEEM image is attributed to the effect of the Lorentz force on the photoelectrons. In our measurements this could not be confirmed: If the Lorentz force was the reason for the displacement of the photoelectrons, the same displacement would occur under equal magnetic field values. Simultaneous inversion of pulse propagation direction and pulse polarity leaves the current and magnetic field unchanged, but in our experiments it resulted in an opposite photoelectron displacement. However, a single inversion of pulse propagation direction leading to opposite magnetic field values results in equal displacement. From this type of time reversal invariance it can be concluded that the breathing of the images in our measurements is only determined by the electrical field.

The pulse profile as measured from the displacement of an edge visible in the images and the transmitted signal measured on the oscilloscope are compared in fig. 4.4.

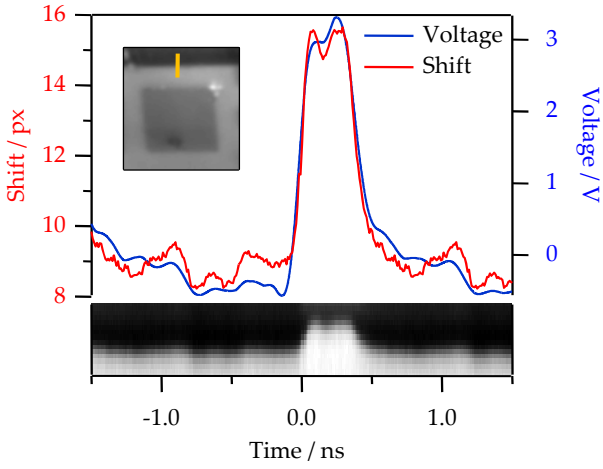

Figure 4.4: Profile of the excitation pulse as measured in transmission on the oscilloscope (blue) and on the sample from the shift of one edge (red). The pulse profile was measured by evaluating line profiles along the orange line (inset) and determining the edge position. The time-dependent line profiles are plotted in the bottom panel.

The bottom panel shows time-dependent line profiles along the orange line shown in the inset. By evaluating the edge position in the line profiles the pulse profile was measured. This comparison shows that the pulse profile is only slightly changed on the way through the RF lines. However, both signals are not equal due to a reflection of the signals. It also becomes obvious that the temporal resolution by the pump-probe measurement is significantly better than that from the oscilloscope which was used for the measurements, since sharp features in the pulse profile are blurred in the oscilloscope data.

4.3 Deflection gating

The time-resolved PEEM technique is based on a stroboscopic pump-probe approach. Since the number of photoelectrons that are emitted by one single photon pulse is not sufficient for image generation, it is necessary to integrate the intensity for several seconds to minutes for one image. During that time the system is repeatedly excited several million times. Thus, it is mandatory that between two subsequent light pulses the magnetic system has enough time to reach a defined ground state before the next pump-probe cycle is initiated by injecting a current pulse through the waveguide. Otherwise ill-defined intermediate states may be probed. Since in most magnetodynamic processes relaxation is based on the restoring force or torque of the demagnetizing field, relaxation takes place on a much slower timescale than the excitation process. Most synchrotrons are working with a typical bunch repetition frequency of 500 MHz. Thus, the delay between two subsequent light pulses is only 2 ns, which is usually much smaller than the required relaxation time of 10-20 ns, for example, if domain wall motion is involved. Therefore, at many synchrotrons special beam conditions are offered, where only one or few electron bunches are circulating inside the

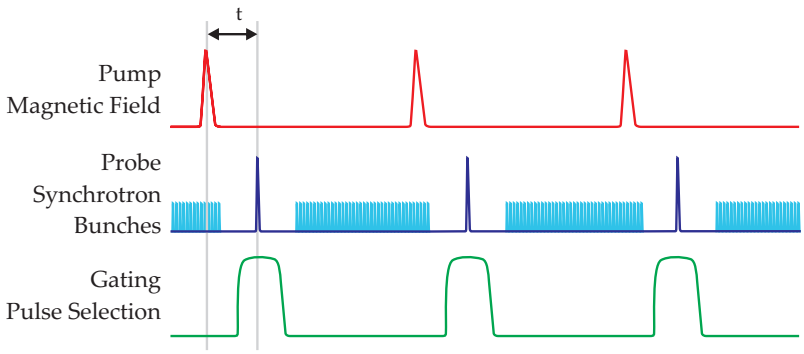

Figure 4.5: Schematics of the hybrid bunch structure with excitation and gating pulses. The system is pumped at a variable delay ΔT before the arrival of the single bunch. Only the single bunch is used for imaging (dark blue), while photoelectrons of the multi bunches (light blue) are blanked out.

storage ring. The standard bunch mode at BESSY-II, similar to the situation at other storage rings, is the "hybrid bunch" mode. Here, most of the intensity is carried by several hundred small electron packets ("multi bunches") following each other with 2 ns temporal separation and one bunch with higher filling ("single bunch") that is isolated from the other bunches by an around 100 ns wide gap (see fig. 4.5 and bottom of fig. 4.7(b)). Using suitable gating mechanisms the contribution of the smaller multi bunches to the PEEM image generation can be suppressed and only the isolated single bunches are used. They are repeated with an interval of 800 ns, which is long enough for the relaxation of the magnetic system (see fig. 4.5 for an illustration).

Several approaches have been pursued to achieve such beam selections: Attempts have been made by using mechanical choppers (KOSCIESZA & BARTUNIK, 1999), but opening windows in the sub-µs range are only achievable under very special conditions (MCPHERSON *et al.*, 2002). For time-resolved PEEM experiments it has been shown that the problem can be solved by gating the MCP detector with a short voltage pulse of several hundred volts (QUITMANN *et al.*, 2008) or by applying voltages pulses to a grid in front of the detector (VOGEL *et al.*, 2003). Both approaches have not been considered for our experiments: On the one hand a grid in front of the detector reduces the transmission, on the other hand the MCP gating method proved to be unsatisfactory in our case, as the signal-to-noise ratio with moderate voltage pulses was too low. The intensity gain of a MCP depends exponentially on the supply voltage with a working point around 2 kV. Thus, by fast switching between e.g. 1.6 kV and 2.0 kV the image intensity can be switched by ca. three orders of magnitude. However, experiments showed that the capacitance of the MCP and cross-talk between MCP and other microscope elements complicates the problem and thus the approach of MCP gating was dismissed.

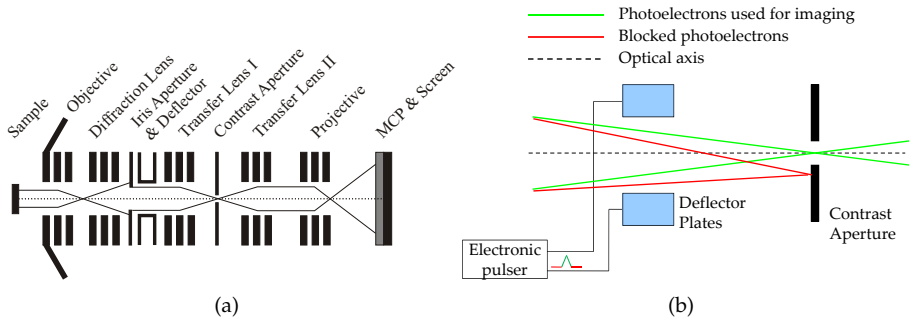

Figure 4.6: (a) Beam path in the PEEM and (b) a schematic drawing of the deflection gating technique.

Instead we made use of a quadrupole deflector system mounted in our PEEM by which the photoelectron beam of unwanted light pulses can be deflected such that it does not pass a small aperture in the microscope column. A similar system was used by REMPFER *et al.* (1991) in pre-CCD times to prevent sensitive in-vacuum films from exposure by photoelectrons. The deflector system is mounted in the first image plane of the microscope and is used to correct misalignments of the microscope and to guide the beam through the small contrast aperture (see fig. 4.6(a) for the beam path). Similar to the situation in a cathode ray tube, the photoelectrons are passing the perpendicularly applied electric deflection field and thus experience a force perpendicular to their propagation direction. The parallel beam is deflected by the angle

$$\alpha_{\mathrm{defl}} \approx \arctan\left(\frac{1}{2}\frac{l}{d}\frac{U_{\mathrm{defl}}}{U_{\mathrm{col}}}\right) \tag{4.1}$$

with the length l and distance d of the deflector plates and the deflection and column voltages U_{defl} and U_{col} (KÜPFMÜLLER *et al.*, 2005). For $l/d \approx 1$ (the exact dimensions are not known) and typical values of $U_{\mathrm{col}} = 1000\,\mathrm{V}$ and $U_{\mathrm{defl}} = 10\,\mathrm{V}$ the deflection angle is $\alpha \approx 0.3\,^{\circ}$. The adjacent transfer lens is adjusted in such way that the image plane at the iris aperture plane is translated into a focal plane at the contrast aperture. By this conversion angles are converted into displacements from the centre and vice versa. Thus, the additional angle that the photoelectrons obtain by passing the deflection potential leads to a displacement of the focal spot in the aperture plane and the electrons are blocked for high enough deflection voltages.

In our experimental situation the beam is displaced such that it does not pass the contrast aperture. For gating a short voltage pulse of $\pm 30\,\mathrm{V}$ is inductively coupled onto two opposite deflector electrodes, such that the beam is not blocked during the duration of the gating pulse. The gating electronics is synchronized to the repetition frequency of the single bunch and is always gating when photoelectrons have been emitted by a single bunch pulse.

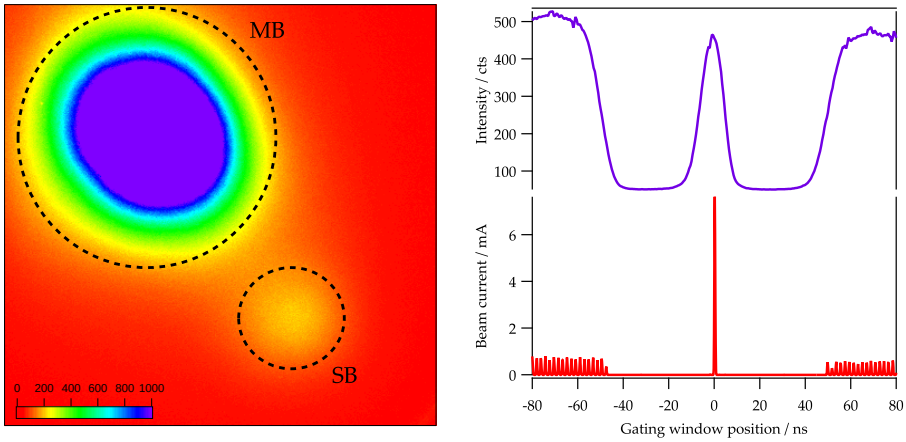

(a) (b)

Figure 4.7: Characterization of the deflection gating technique: (a) Image of the photoelectron distribution in the focal-plane with turned on gating. "MB" marks the position of the multi bunch electrons, "SB" marks the position of the deflected single bunch electrons. (b) Bunch pattern of the BESSY-II hybrid bunch (bottom) with a corresponding measurement of the gated intensity plotted against temporal position of the gating window (top).

With the help of the second transfer lens the microscope can be switched between showing real-space images of the sample surface and the angle distribution of the photoelectrons. The latter corresponds to the photoelectron distribution in the contrast aperture plane. A typical image of the angle distribution in the focal plane is shown in fig. 4.7(a). This image has been acquired in the gating mode for a contrast aperture with a large diameter. In this mode all photoelectrons can pass the contrast aperture leading to a large energy spread and degraded image resolution in real-space imaging. However, when imaging the angle distribution this mode reveals the functionality of the gating principle. In fig. 4.7(a) two focus positions can be discerned, marked by "MB" and "SB": A focus of the undeflected multi bunch electrons (MB) and a second focus from the single bunch electrons (SB), which are deflected from the original position. This image also shows the relationship of the intensities of the multi bunch and single bunch pulses. The multi bunch pulses carry about 97% of the intensity. By choosing a contrast aperture with a smaller opening and placing it at the position marked by "SB" all the multi bunch contribution is blocked and only single bunch pulses are used for imaging.

The timing characteristics of the deflection gating is shown in fig. 4.7(b). Here the gated intensity was measured while changing the delay between gating pulse and single bunch ($t = 0$). Five different regions can be discriminated in the measurements. For $t = 0$ the gating window only overlaps with the single bunch illumination

and thus only those electrons are passing the contrast aperture. This is the correct adjustment for the study of magnetization dynamics. If the absolute value of the delay is slightly increased, the gating window hits the gap that separates the single bunch from the multi bunches and no photoelectron pulse overlaps with the gating window. For larger positive or negative delays the intensity increases again because now the gating pulse deflects electrons created by multi bunch illumination. The relationship between single bunch and multi bunch intensity is different in the measured intensity and the bunch pattern shown at the bottom of fig. 4.7(b) because the gating window has a temporal width of 10-20 ns and during that time 5-10 multi bunches can pass the contrast aperture carrying more intensity than one single bunch.

These measurements show that the temporal width of the gating window is small enough to only overlap with the single bunch illumination and thus contributions of the unwanted multi bunches to the image generation are effectively blocked. A degradation in image quality compared to ungated measurements could not be observed.

4.4 Accessing buried interfaces

The finite escape depth of the photoelectrons and the tunability of the photon energy in X-ray photoemission experiments provides access to buried layers. By tilting the sample relative to the incoming light the probing depth can be varied between bulk- and surface-sensitive. However, in PEEM experiments this option is not available, since usually the microscope column, sample position and light incidence direction are fixed. In this section I present a new approach of laterally and depth-resolved experiments in a PEEM via standing-wave excited photoemission.

X-ray standing waves have been widely used in hard X-ray experiments for the determination of surface structure (WOODRUFF, 2005). In such experiments Bragg reflection from a single-crystal generates an X-ray standing wave field above the crystal surface due to a superposition of incoming and reflected waves. Recently this concept has been applied to soft X-ray photoemission experiments by the use of synthetic multilayer mirrors as standing wave generators (HAYASHI *et al.*, 1996; YANG *et al.*, 2000). Bragg reflection leads to the generation of a standing wave field above the multilayer mirror, which is illustrated in fig. 4.8(a). By growing a wedge-shaped layer on top of this multilayer, the position of the standing wave maxima can be scanned relative to the position of the layers and interfaces above the wedge by laterally displacing the sample (see fig. 4.8(b)). With the so-called *SWEDGE* (standing wave/wedge) technique the determination of elemental intermixing and magnetic moments at buried interfaces can be studied by evaluating the photoelectron and XMCD spectra at different wedge positions (YANG *et al.*, 2002).

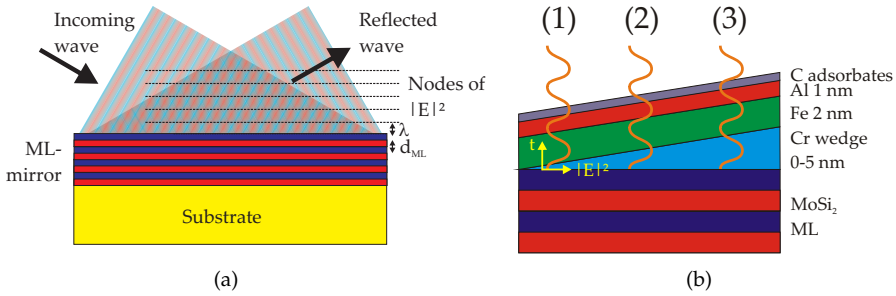

Figure 4.8: (a) Illustration of the standing wave generation above a multilayer mirror. The superposition of incoming and reflected wave generates nodes and anti-nodes of the squared electrical field $|E|^2$ with the periodicity of the multilayer mirror. (b) Illustration of the standing wave method with a wedged multilayer-system: By laterally displacing the sample the maxima of the standing wave are scanned through the layers and interfaces: (1) maximum in C adsorbats, (2) maximum in Al layer, (3) maximum in Fe layer.

By replacing the long wedge with one that is shorter than the typical size of the field of view, such experiments can also be carried out in a PEEM by illuminating the whole wedge in one image instead of scanning the sample laterally. First experiments have been carried out at the beamline UE49-PGM-a at BESSY-II using the SPEEM faciliy. This instrument is equipped with a hemispherical energy analyser enabling imaging based on a selected photoelectron peak. Samples were grown on a $Si/MoSi_2$ multilayer mirror consisting of 40 bilayers with a periodicity of 4 nm. First experiments with an Ag wedge have proved that the experimental concept works and the results have been published in KRONAST *et al.* (2008a).

Results of experiments carried out on an multilayer system with a Cr wedge (see fig. 4.8(b)) will be presented in the following. The sample has been grown by MBE. The thickness gradient along the wedge was generated by fixing a razor blade between sample surface and evaporation crucible. The blade prevents parts of the surface from evaporation. At the transition between shadowed and free regions a narrow Cr wedge is generated in the half-shadow.

For the standing wave experiments it is mandatory to have two modes of energy selection. While the photon energy has to be tuned to fulfil the Bragg condition in order to obtain maximum reflectivity at the multilayer mirror for the given angle of incidence, the energy analyser of the microscope has to be used to select photoelectrons with a certain kinetic energy in order to maintain elemental selectivity. A typical photoelectron spectrum is shown in fig. 4.9 taken with constant photon energy and varying kinetic energy. The photoelectron peaks can be identified and assigned to the constituting elements of the single layers.

By tuning the photon energy to the first-order Bragg peak of maximum reflectivity,

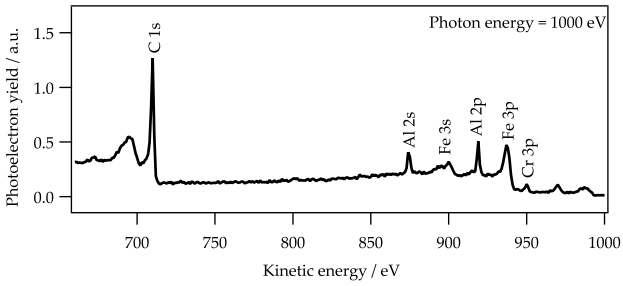

Figure 4.9: Photoelectron spectrum of the multilayer sample. The photon energy was held constant at 1000 eV and only the analyser voltage filtering the kinetic energy was varied. Thus, elemental selectivity in the PEEM measurements is possible without changing the photon energy.

strong standing waves above the mirror are created. Using the relation

$$\lambda_x = \frac{c}{\nu} = 2d_{\mathrm{ML}} \sin\theta_{\mathrm{Bragg}} \tag{4.2}$$

with a fixed incidence angle $\theta = 16^\circ \pm 2^\circ$, we obtain a photon energy of the Bragg maximum of $E_x = (570 \pm 70)$ eV.

By scanning the photon energy over this area and simultaneously driving the analyser energy the photoelectron yield of a fixed initial state (e.g. C-1*s*) is monitored. In these measurements a modulation of the intensity near the expected Bragg maximum could be detected. The position of this modulation was moving when the sample tilt was varied and thus the modulation could be unambiguously ascribed to reflectivity changes giving rise to standing wave effects. The strongest modulation effects were found for $E_x = 610\,\mathrm{eV}$ corresponding to a Bragg angle of $\theta_{\mathrm{Bragg}} = 14.7^\circ$.

With the photon energy tuned to the Bragg maximum the standing wave modulations can be made visible by imaging the wedge with photoelectrons stemming from the separate layers. Fig. 4.10 shows the modulation effects appearing in the carbon layer (imaged by the C-*1s* electrons) and the Fe layer (imaged by the Fe-*2p* electrons). While in the C-*1s* image the modulation is clearly visible in the PEEM images, the image of the Fe modulations have been generated by the difference of a picture taken at the Bragg peak ($E = 610\,\mathrm{eV}$) and one taken well below the Bragg peak ($E = 580\,\mathrm{eV}$). Using this technique, contributions in the images that do not depend on the photon energy are removed.

To scan the standing wave through the sample the photon energy is varied across the Bragg resonance. Due to the finite number of layers in our multilayer mirror the reflectivity curve has a finite width. By X-ray optical calculations the FWHM of the Bragg peak has been calculated to 16 eV (GULLIKSON, 2008). Over the same energy range the phase changes by about 120°. Thus, by changing the photon energy the maxima of the electrical field are moved through the layers. Line profiles over the wedge for different photon energies are displayed in fig. 4.11 showing the change of the photoelectron intensities when varying the photon energy around the Bragg maximum.

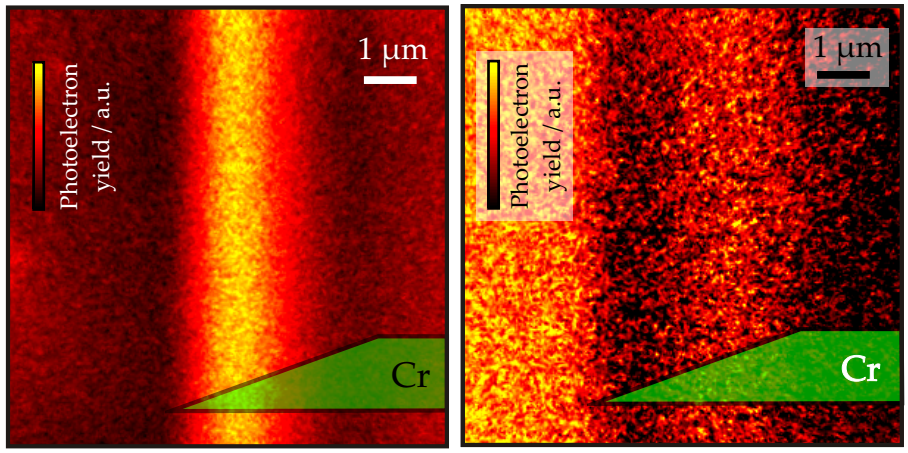

(a) C 1s (b) Fe 2p

Figure 4.10: Standing wave modulations in PEEM images with the photon energy tuned to the first Bragg maximum and kinetic energy selection of electrons from C-*1s* states (a) and Fe-*2p* states (b). The position of the wedge is indicated by the green profile.

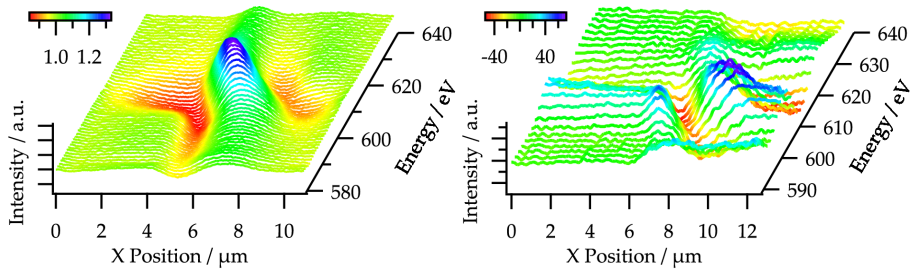

(a) C-*1s* (b) Fe-*2p*

Figure 4.11: Linescans of the C-*1s* (a) and Fe-*2p* (b) photoelectrons taken at different photon energies around the Bragg peak visualizing the modulation of the photoelectron intensities along the wedge.

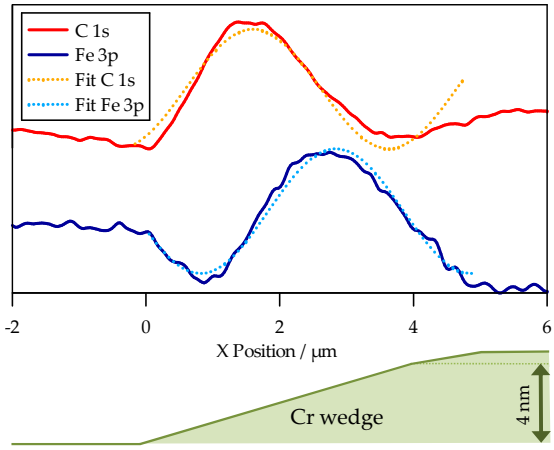

Figure 4.12: Line profiles over the wedge for the Fe and C layers with corresponding sine-fits. For $x < 4\,\mu m$ the wedge has a linear gradient, at higher values the slope decreases. The fit curves are shifted by 1.05 µm with respect to each other.

Fig. 4.12 compares line profiles over the wedge for both layers taken at a fixed energy. Both of them clearly show modulations depending on the wedge thickness that have been fitted with a sine function. The sine fit matches the measured intensity profile well for $x < 4$ µm. At higher x-values still a modulation is present but deviating from the sine fit. The modulation has a period of $l_\lambda = 4$ µm. Thus, we conclude that for $0 < x < 4$ µm the wedge has a linear gradient and a flattening at higher values. Due to the constant slope, lateral distances along the wedge can be directly translated to relative vertical positions of the standing wave maxima. With $\lambda/l_\lambda = 4\,nm/4\,\mu m = 10^{-3}$, the wedge height at $x = 4$ µm corresponds to the standing wave wavelength of 4 nm. The two fit curves are shifted by Δl =1.05 µm. Neglecting effects due to finite thickness this value corresponds to a height difference of $\Delta l \cdot \lambda/l_\lambda = 1.05\,nm$. Regarding the deposition parameters the C and Fe layers are expected to be separated by a 1 nm thick Al layer which agrees reasonably well with the measured value.

4.5 Summary of the methodical developments

This chapter focussed on the methodical developments of the PEEM method improving the investigations of magnetic heterostructures. In order to study magnetization dynamics the PEEM was prepared for time-resolved measurements. For this purpose a sample design employing coplanar waveguides and a sample stage with high-frequency cables and adapters have been developed. In addition, the regular time-structure at BESSY-II made it necessary to realize a novel gating concept. We have used a system of deflectors in the PEEM to switch the photoelectron beam between passing the contrast aperture and being blocked by it. The approach has proved to work reliably on a timescale of 20 ns and is thus feasible for blanking out the contribution of unwanted light pulses to the image generation in order to increase the

time interval between two photoelectron pulses. Measurements carried out in such a virtual single bunch mode will be presented in chapter 6.

Moreover, first experiments have been carried out implementing the *SWEDGE* method into microscopy. Using a multilayer mirror as a standing wave generator and a multilayer structure with one wedged layer, it has been shown that depth resolution beyond the regular exponential decay can be reached. The *SWEDGE* technique is a well-established method in photoelectron spectroscopy. Our measurements prove that such experiments can also be carried out in microscopy within one image and without the necessity to scan the lateral sample position. However, the findings presented in this thesis and in KRONAST *et al.* (2008a) are yet in a state of "proof-of-principle". With an optimized sample design it is expected to enable the microscopic study of the buried layers and interfaces. In combination with magnetic sensitivity given by the XMCD effect a magnetic depth profiling of the magnetic domain structure might be possible. In magnetic heterostructure systems the analysis of the interface domain structure could give new insights in the understanding of coupling mechanisms.

Chapter 5

Domain structure in magnetic heterostructures

As a prerequisite for the study of magnetization dynamics, the equilibrium magnetization patterns of various magnetically coupled heterostructures have been investigated. As pointed out above, by applying its elemental and magnetic contrast mechanisms XMCD-PEEM is an ideal method for such studies. In this chapter, layer-resolved magnetization patterns of different material systems are introduced and discussed regarding their coupling properties.

5.1 Dual-Heusler systems

Having been discovered more than hundred years ago by HEUSLER (1903), Heusler alloys have recently received great interest due to their promising properties for application in spintronics devices (PALMSTRØM, 2003). With a high Curie temperature of around 1000 K for particular systems and structural compatibility to semiconductor materials they are fulfilling important prerequisites for their applicability in technology. The potential half-metallic character of Co-based Heusler alloys makes them an interesting topic for investigation.

Heusler alloys are ternary compounds with the general formula X_2YZ consisting of two transition metals X, Y and one element Z of the $III - V$ groups. They crystallize in the $L2_1$ phase consisting of four interpenetrating fcc lattices, as shown in fig. 5.1(a). Bulk electronic structure calculations (e.g. DE GROOT *et al.* (1983); GALANAKIS *et al.* (2002)) show that many Heusler compounds have half-metallic character, i.e. only one spin-band has a finite density of states at the Fermi energy yielding 100% spin-polarization at the Fermi level. The calculated DOS of Co_2MnSi indicating the half-metallic character is shown in fig. 5.1(b).

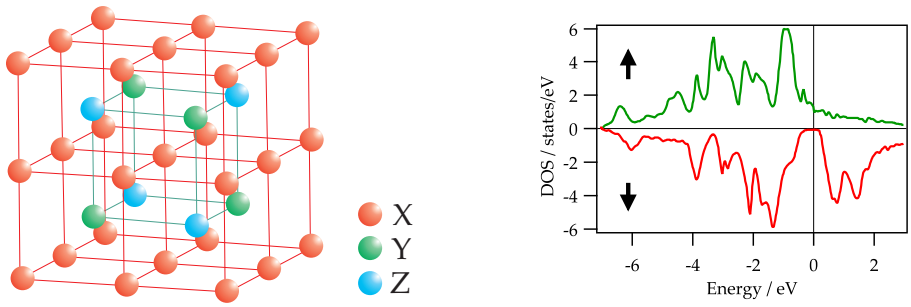

(a) (b)

Figure 5.1: (a) General $L2_1$ structure of Heusler compounds X_2YZ. (b) Calculated spin-split density of states of Co_2MnSi (GALANAKIS *et al.*, 2002) showing the half-metallic character of the Heusler compound: The spin-down band shows insulating behaviour due to the band gap at the Fermi energy while the spin-down band has metallic character.

Due to these facts half-metallic Heusler compounds are potential electrode materials for magnetic tunnel junctions (MTJ). MTJs consist of two magnetic electrodes separated by a very thin tunnelling barrier. Due to the spin-split density of states their resistivity depends on the alignment of the two electrodes which can be understood in a simple physical picture (BÜRGLER & GRÜNBERG, 2005): Assuming energy and spin conservation during the tunnelling process, the tunnelling current can be understood as the sum of spin-up and spin-down contributions $I_{\text{total}} = I_\uparrow + I_\downarrow$. The value of the different contributions depends on the density of states at the Fermi level and the match of the electronic states of the two metals. The possible configurations are sketched in fig. 5.2 showing that the tunnelling current is highest for the spin-up channel in parallel configuration. The tunnelling magnetoresistance (TMR) in the diffusive limit can be quantitatively described by JULLIERE's model (1975) as

$$\text{TMR} = \frac{R_{\uparrow\downarrow} - R_{\uparrow\uparrow}}{R_{\uparrow\uparrow}} = \frac{2P_1P_2}{1 - P_1P_2}$$

with the spin polarization values at the Fermi level of the two electrodes P_1 and P_2 and the resistances $R_{\uparrow\downarrow}$ and $R_{\uparrow\uparrow}$ of the antiparallel and the parallel magnetization configuration, respectively. In this simplified model Heusler compounds with a spin polarization of up to 100 % at the Fermi level are expected to show an infinitely high TMR effect. Indeed high TMR values have been demonstrated experimentally for Heusler-based MTJs (SAKURABA *et al.*, 2006). The use of epitaxially grown electrode/barrier combinations might lead to even higher values due to the reduction of defects and the onset of resonant tunneling mechanisms (YUASA *et al.*, 2004). Magnesium oxide (MgO) provides compatible lattice constants to many Heusler alloys allowing for epitaxial growth of the MTJ structures (YAMAMOTO *et al.*, 2006).

Co_2MnSi (CMS) and Co_2FeSi (CFS) are two protagonists of the class predicted to ex-

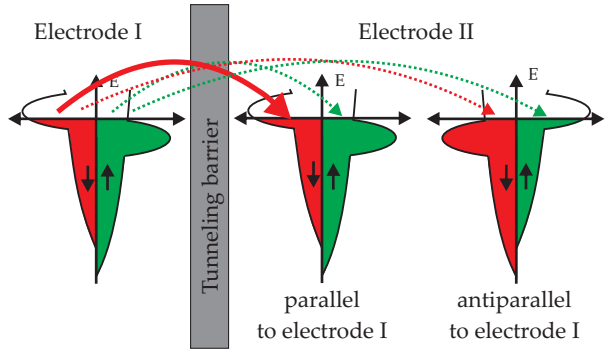

Figure 5.2: Illustration of the TMR effect for parallel and antiparallel configuration. Due to the high DOS at the Fermi level and a good match of the electronic states, the tunnelling current is highest for the spin-up channel in parallel configuration of the two electrodes (indicated by the thick arrow), while for other configurations the tunnelling current is lower (dotted arrows).

hibit half-metallic behaviour, having similar lattice constants and providing structural compatibility to MgO. Both materials have very high Curie temperatures of 985 K (CMS, WEBSTER & ZIEBECK (1988)) and 1100 K (CFS, WURMEHL *et al.* (2005)), thereby fulfilling a prerequisite for their potential use in applications. The magnetic moment per formula unit is 5.07 μ_B (CMS) and 6 μ_B (CFS), respectively. The experimental results described below show that both materials have clearly distinguishable coercive fields. This opens a pathway to combine CFS and CMS in one MTJ in the sense of a pseudo spin-valve structure, i.e., without using exchange bias materials for the reference magnetization direction.

Up to now many macroscopic studies of the magnetic, electronic and structural properties of magnetic tunnel junctions have been carried out. As a complement to these investigations we have studied the domain structure of $Co_2FeSi/MgO/Co_2MnSi$ trilayers as a prototypical system for an epitaxial dual-Heusler MTJ. The results of this study have been published in KAISER *et al.* (2009a) and will be discussed in the following.

Single films and trilayer structures have been prepared by magnetron sputtering onto Silicon substrates with a 20 nm Vanadium seed layer at room temperature, followed by an in-situ annealing step at 450°C (single films) and 300°C (trilayers with MgO), respectively. During the sputtering process a residual in-plane magnetic field of 7 mT was present in the deposition chamber. Afterwards the samples have not been exposed to any other magnetic field and have been studied in the as-grown state. The films have been capped with a thin Vanadium layer to prevent oxidation of the layer stack. X-ray diffraction patterns showed the films to grow in a highly textured B2-phase. This is expected to result in a reduction of the spin-polarization and therefore a loss of the half-metallicity as compared to the preferred $L2_1$-phase (PICOZZI *et al.*, 2004). The films have subsequently been microstructured by optical lithography and Argon ion beam milling into squares with areas ranging from 2×2 to $100 \times 100\,\mu m^2$. Prior to the microscopy experiments $M(H)$-curves have been measured using vibrating sample magnetometry in order to determine the coercive fields and magnetic moments.

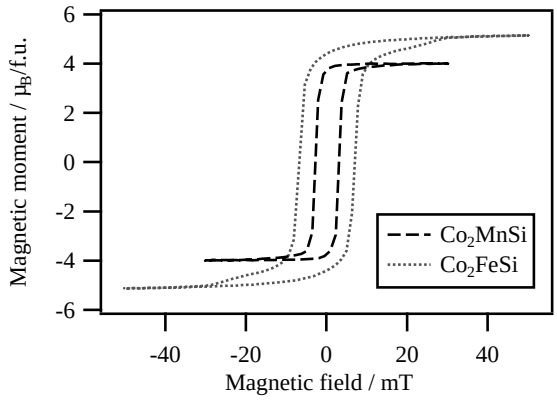

Figure 5.3: In-plane $M(H)$-curves of 20 nm Co_2MnSi (CMS) and Co_2FeSi (CFS) thin films measured with vibrating sample magnetometry, showing the difference in saturation magnetization and coercive fields.

5.1.1 Single films

Fig. 5.3 shows the $M(H)$-curves of 20 nm thick single films of CMS and CFS measured with the magnetic field applied in the film plane. They exhibit different coercive fields of 2.8 mT (CMS) and 6.5 mT (CFS) and magnetic moments per formula unit of 4.0 μ_B (CMS) and 5.2 μ_B (CFS). The reduction of the magnetic moments compared to the bulk values can be explained by atomic site disorder and interface effects. The hysteresis measurements have been carried out with the magnetic field applied along different in-plane angles in order to determine a possible global magnetic anisotropy in the samples. For both samples no sizeable in-plane anisotropy could be found. This in-plane isotropy of the samples was also confirmed by FMR measurements carried out by ZAKERI (2007).

The magnetic structure of both materials (fig. 5.4) is strongly influenced by the polycrystalline nature of the films. In both films multi-domain states are formed with the local magnetization direction laterally varying due to anisotropy fluctuations ("magnetization ripple"). However, a perpendicular magnetization direction is strongly suppressed by the demagnetizing field forcing the average magnetization direction into the film plane. A direct comparison of the images in Figs. 5.4(a) and 5.4(b) reveals clear differences between CMS and CFS. Both films develop a magnetization ripple with the average magnetization vector pointing perpendicular to the domain walls (HOFFMANN, 1968). The existence of magnetization ripple can be attributed to the polycrystalline nature of the films leading to a strong variation of the local magnetocrystalline anisotropy associated with each grain. The average wavelength of the periodic ripple structure can be correlated with the average crystallite size (BALTZ & DOYLE, 1964). In our measurements the CMS film showed a more textured magnetization distribution with a preferred axis, giving rise to the "feathery" pattern. In contrast, the CFS films reveal a grain-type domain structure, which is possibly related to a smaller grain structure and higher disorder in the film. The average ripple

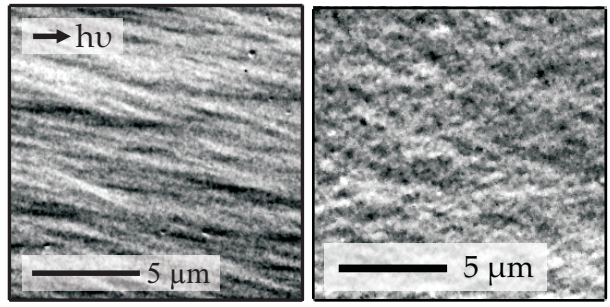

(a) CMS (b) CFS

Figure 5.4: Magnetic domain patterns of extended (a) CMS and (b) CFS films. The magnetic contrast originates from XMCD at the Co L_3 edge. In all images the direction of light incidence is from left to the right.

wavelength in CMS is about 1.89 µm and significantly larger than the value for the respective CFS films (0.68 µm).

In comparison with fig. 5.3, it is also interesting to note that the shorter ripple wavelength in CFS is in fact related to a higher coercivity. This finding is consistent with the picture that the smaller grains and higher disorder in this film type block the magnetization reversal process, for example, via domain wall pinning.

In the next step, we structured the films into small micrometre-sized elements resulting in the introduction of a demagnetizing field acting on the structures. In the magnetic domain patterns, the difference between the two materials becomes even more obvious: Under the influence of the shape-induced demagnetizing field, the response of elements of comparable size is distinctly different. The CMS film develops a so-called concertina or buckling pattern (shown in fig. 5.5(c)) also known from Permalloy elements in a similar thickness range (CHUMAKOV *et al.*, 2005). It is formed by alternating low-angle walls with the local magnetization direction varying around the average magnetization. With decreasing element size the effect of the demagnetizing field becomes stronger and successively simpler flux-closure patterns reminiscent of Landau states start to form (fig. 5.5(a) and 5.5(b)), which are still accompanied by buckling structures. The latter disappear for elements in the micrometre regime. However, the occurrence of the buckling state is not necessarily the magnetic ground state configuration, but may arise due to a local energetic minimum caused by neighbouring domains blocking each other.

A completely different response is observed in the CFS films. Even under the influence of the demagnetizing field in small $10 \times 10\,\mu m^2$ elements (fig. 5.5(d)) the polycrystalline nature of the film is dominating the magnetization pattern and the fine-grained domain structure remains essentially unchanged from that observed in the extended film (fig. 5.4(b)). This result shows that the intrinsic anisotropy of the CFS-film is much stronger than the demagnetizing field of the square element.

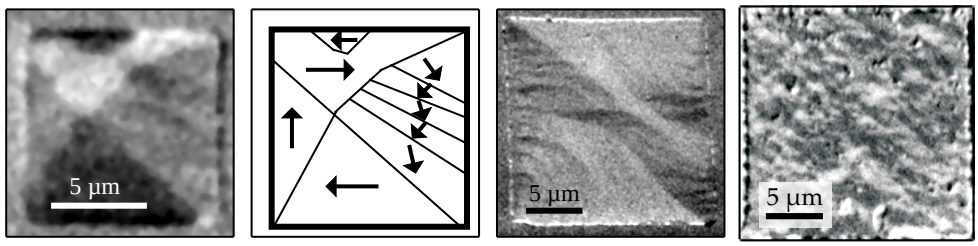

(a) CMS 10×10 µm^2 (b) CMS (sketched) (c) CMS 20×20 µm^2 (d) CFS 20×20 µm^2

Figure 5.5: Magnetic domain structures in patterned CMS and CFS elements. (a) CMS 10x10 µm^2, (b) Sketch of domain pattern in CMS 10×10 µm^2, (c) CMS 20×20 µm^2, (d) CFS 20×20 µm^2. In each case the magnetic contrast has been obtained at the Co L_3 edge.

5.1.2 Trilayer: Co_2MnSi (20 nm)/MgO (3 nm)/Co_2FeSi (2 nm)

In a second step the single Heusler films have been combined into trilayer structures with a MgO interlayer of 3 nm thickness. In order to separate the magnetic response of the individual layers in this stack, the full versatility of soft X-ray PEEM is needed. By tuning the photon energy of the incident beam to the L_3-absorption edges of the specific elements (Co, Mn, Fe) the magnetization of both ferromagnetic layers can be investigated independently. At the Co edge, the response of both the CFS and CMS layers is probed, whereas XMCD at the Fe and Mn edges provides the magnetic information of the CFS and CMS layer, respectively.

In the case of the CMS (20 nm)/MgO (3 nm)/CFS (2 nm) structure (our nomenclature always starts with the bottom layer), the resulting domain images for a 10-µm square element are compiled in fig. 5.6. The thickness of the CFS layer has been chosen as 2 nm, in order to still be able to probe the bottom CMS layer. It has to be noted that due to the lower film thickness of the top layer, a direct comparison to the results of the single film measurements in chapter 3.1 is not possible, since the film thickness may strongly influence the domain configuration. As we will show below, however, magnetic coupling phenomena are the dominant effects determining the top layer magnetization distribution.

The information depth for the total yield detection mode in PEEM is limited to a few nanometres in metals (FRAZER *et al.*, 2003). As a consequence, the Mn-signal is rather weak and the magnetic contrast is only about 20 % of that of the Co and Fe signals. In order to facilitate the comparison of the images in fig. 5.6 the Mn-contrast has thus been scaled up to the same level as for Co and Fe.

A direct comparison of the three domain patterns reveals identical structures for the Co and Fe data. Although the contrast on the Mn absorption edge is weaker and the

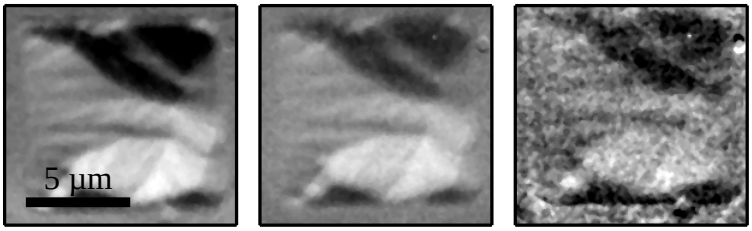

(a) Co-L_3 (b) Fe-L_3 (c) Mn-L_3

Figure 5.6: Element-selective domain imaging in the layer system CMS/MgO/CFS, revealing a parallel magnetic coupling of the CFS and CMS films. In the first two images (Co, Fe) the same scaling of the magnetic contrast is used, while in the third image (Mn) the measured contrast is five times smaller and has been upscaled for better visibility. The element size is $10\times10\,\mu m^2$.

image has a lesser signal-to-noise figure, the main domain features, but also some of the concertina structures can be clearly discerned. This indicates that the two Heusler films are indeed not magnetically independent, but exhibit a considerable ferromagnetic coupling through the MgO interlayer. The reasons for this coupling can be a roughness-induced Néel/orange-peel mechanism or pinholes in the MgO layers, as discussed in sect. 2.3.

The data also show that the micromagnetic behaviour of the CMS(20 nm)/MgO(3 nm)/CFS(2 nm) trilayer stack is strongly dominated by the thicker CMS film. The domain patterns shown in fig. 5.6 and in 5.7(a) resemble the situation of the single CMS film. While for the larger $20 \times 20\ \mu m^2$ element the magnetic microstructure is determined by the polycrystalline structure of the film and a magnetization ripple is formed, for $10 \times 10\ \mu m^2$ elements the competition between anisotropy-induced ripple formation and flux closure domains due to the demagnetizing field creates a very different equilibrium configuration.

5.1.3 Trilayer: Co_2FeSi (20 nm)/MgO (3 nm)/ Co_2MnSi (2 nm)

As a surprise, the magnetic microstructure changes drastically, when the layer sequence of the trilayer is reversed, i.e., the bottom layer is formed by a 20 nm thick CFS film. Instead of the anisotropy-dominated multi-domain ripple structure shown in fig. 5.5(d) we find a completely different behaviour (see fig. 5.7(b)). The average domain size increased and a low-remanence magnetization pattern consisting of two antiparallel Landau domains are formed. Some of the 90°-walls have been replaced by an additional domain with two low-angle walls. This configuration has been referred to as "tulip" state (HUBERT & RÜHRIG, 1991). The 180°-walls between neighbouring antiparallel domains are modified by a high density of cross-ties. By

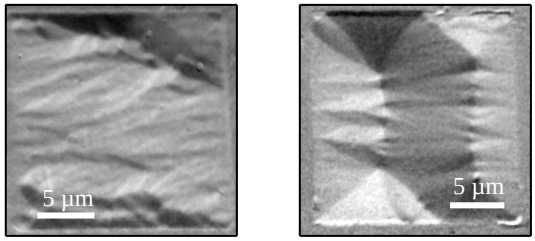

(a) (b)

Figure 5.7: Comparison of magnetic domain patterns acquired at the Co L_3 edge of 20×20 µm^2 square elements of both trilayers CMS(20 nm)/MgO(3)/CFS(2) (a) and CFS(20)/MgO(3)/CMS(2) (b).

the formation of cross-ties the magnetostatic energy is reduced, since 180°-walls are replaced by energetically more favourable 90°-walls (HUBER JR. *et al.*, 1958).

The element-selective analysis of the domain structure reveals similar magnetic structures at the Co-L_3 and Fe-L_3 absorption edges, which is consistent with the domain structure resulting from the CFS film. On the other hand, we do not find a magnetic contrast at the Mn-L_3 edge. In addition, the Co magnetic signal is not significantly stronger than the Fe signal. If the Co signal would be acquired from both layers, however, that would be the case. As our method has been shown to be able to even pick up the Mn XMCD from the buried layer in the CMS/MgO/CFS sandwich, we must conclude that the CMS film in our trilayer is nonmagnetic – at least at room temperature, where the experiments have been carried out. This behaviour may be attributed to a strong thickness dependence of the CMS magnetic moment in thin films below 8 nm thickness supporting the results of previous XAS and FMR measurements (SCHMALHORST *et al.*, 2004; WANG *et al.*, 2005; RAMEEV *et al.*, 2006). A strongly reduced Curie temperature in the 2 nm CMS film may be explained by interdiffusion at the interface leading to a higher atomic disorder. Furthermore, this result seems to indicate that the MgO barrier in this layer has only a negligible density of pinholes, because a direct exchange coupling to the bottom CFS layer should also result in a common Curie temperature for both layers. Hence one can postulate that the parallel coupling of the other investigated trilayer system, that has been deposited under the same conditions, is induced by orange-peel coupling due to rough bottom layers.

Room-temperature $M(H)$-measurements of the CFS/MgO/CMS sandwich reveals a soft magnetic behaviour with a coercive field of 2.5 mT and a total magnetic moment of 4.6 $\mu_B/f.u.$. With the 2 nm thin CMS layer being magnetically inactive the difference in the magnetic properties of this trilayer and the single CFS film can only be explained by the different annealing temperatures of both samples ($T_{\text{trilayer}} = 300\,^{\circ}\text{C}$, $T_{\text{singlelayer}} = 450\,^{\circ}\text{C}$). By the lower annealing temperature the crystalline structure is not fully established leading to a weaker magnetocrystalline anisotropy. Similar results have indeed been reported by OOGANE *et al.* (2007). Thus, the relative influ-

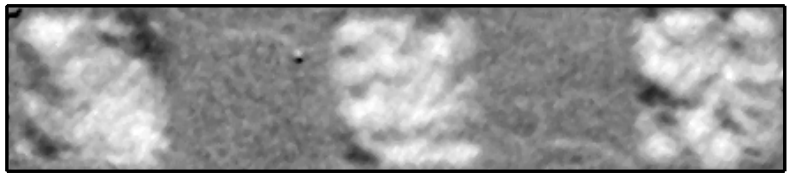

(a) 200°C

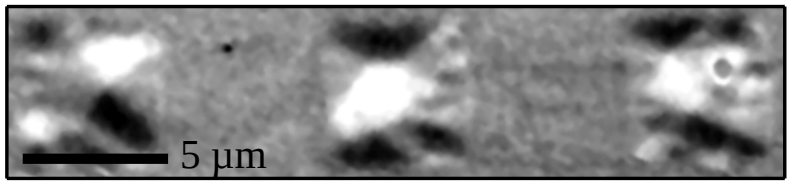

(b) 270°C

Figure 5.8: Snapshots of the magnetization distribution in a CMS/MgO/CFS sandwich during annealing to different temperatures taken at the cobalt L_3 absorption edges. Size of the square elements: $5 \times 5\ \mu m^2$. Both images refer to the same grey scale.

ence of the demagnetizing field may be stronger. As a consequence, the formation of Landau-type flux-closure patterns is favoured over a multi-domain magnetization ripple.

5.1.4 Effect of annealing on the magnetic microstructure

In order to gain more insight into the role of the annealing process and temperature, we have also performed in-situ annealing experiments on the above samples in the photoemission microscope, using a built-in heating stage. It is a well-known fact that the deposition or annealing temperature of Heusler alloys has a strong impact on their structural, magnetic and electric properties (KÄMMERER, 2003). In particular, the annealing should lead to a reduction of the site disorder. Therefore, the Heusler phase formation will also have a strong effect on the micromagnetic structure of the individual films and of the layer stack. As an example, we have chosen a CMS(20 nm)/MgO(3 nm)/CFS(2 nm) trilayer in the as-grown state for the annealing experiments. As a new approach to the problem, we have taken the magnetic domain images directly at different sample temperatures and not at room temperature after the annealing. In this way, we are able to directly follow the evolution of magnetic changes in the system. Note that this approach requires the Curie temperature to be sufficiently high to yield a magnetic signal in PEEM.

The as-grown layer stack indeed exhibits only a quite weak magnetic dichroism at the

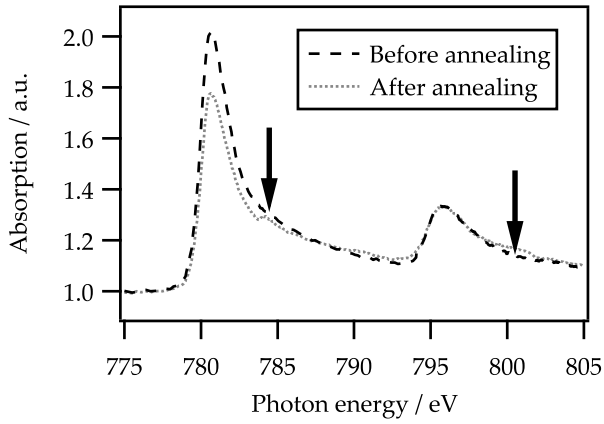

Figure 5.9: X-ray absorption spectra of the Co $L_{2,3}$ edges before and after the annealing step. Features changing during the annealing procedure are marked by the arrows.

Co-L_3-edge. As a consequence, the domain pattern observed at room temperature is rather diffuse and noisy. This result does not change very much up to a temperature of 200°C (fig. 5.8(a)). Between 230°C (not shown) and 270°C, however, we observe a sudden change of the domain pattern (fig. 5.8(b)): Despite the elevated temperature, the contrast becomes stronger and the domain pattern more regular. This change can be linked to a (partial) formation of the Heusler phase. In order to prove this link, we have also acquired additional spectroscopic information by taking local X-ray absorption spectra across the Co-$L_{2,3}$-edges (fig. 5.9). Comparing the spectra of the as-grown with those of the annealed state, we can clearly see that the change in the magnetic microstructure is accompanied by the appearance of an additional spectral feature on the high-energy side of the main absorption lines. This additional feature has previously been identified as an indication for increased atomic and magnetic order in these materials (SCHMALHORST *et al.*, 2004) and is therefore sometimes referred to as "Heusler peak". Our experimental approach provides a direct access to the formation dynamics of the Heusler phase and will be expanded to other systems in the future.

5.2 Epitaxial systems

5.2.1 Fe/Cr/Co trilayers

The Fe/Cr system is among the most intensely studied systems exhibiting interlayer exchange coupling. In contrast to noble spacer materials it is the complex Fermi surface of Cr and its antiferromagnetic character, that is complicating the interpretation of coupling measurements. However, two coupling periods have been found (STILES, 2004; BÜRGLER *et al.*, 2001): A long one with $\lambda \approx 1.8\,\text{nm}$ (12.5 monolayers) and a short one with $\lambda \approx 0.29\,\text{nm}$ (2 ML). The short coupling period is attributed to proximity coupling due to the antiferromagnetic ordering of the Cr interlayer, as discussed in

sect. 2.3.2, and the longer coupling period is attributed to interlayer exchange coupling and can be ascribed to features in the Fermi surface of Cr (BÜRGLER *et al.*, 2001). UNGURIS *et al.* (1991) have shown that the short coupling period depends strongly on the growth quality and can be suppressed for films with a higher grade of disorder.

However, the advantage of elemental selectivity in magnetic imaging with PEEM does only hold if different materials are incorporated. Thus, we have investigated chemically asymmetric Fe/Cr/Co trilayers in order to be able to access the micromagnetic state of both ferromagnetic layers. The same system has been studied by THEIS-BRÖHL *et al.* (1996) by MOKE and FMR measurements. They observed an oscillatory interlayer coupling and a strong dependence of the M(H) curves on the corresponding spacer thickness d with a coupling period of $\lambda = 10 - 11$ ML superimposed of a strong biquadratic coupling and hints for the existence of a short 2 ML coupling period. Theis-Bröhl et al. report of very weak antiferromagnetic coupling. Together with the low coercive field of Fe, which can be tuned by the Cr interlayer thickness, Fe/Cr/Co trilayers are considered as an interesting material combination for spin-valves. KUCH *et al.* (1998) have carried out spatially resolving PEEM measurements on Fe-whiskers covered with Cr and Co thin films but besides one transition between parallel and antiparallel coupling at 2 ML no evidence for an oscillatory coupling was found, particularly no extended regions with biquadratic coupling were observed.

We have studied the coupling behaviour in Fe(10 nm)/Cr(0-5 nm)/Co(2 nm) trilayers grown by MBE on GaAs substrates with Ag buffer layers. The Fe (001) films grow epitaxially with bcc structure on the Ag buffer layers (BÜRGLER *et al.*, 1997) and are thus exhibiting a four-fold inplane anisotropy. The Cr interlayer was deposited with a linear thickness gradient in order to study different coupling strengths within a single sample. The crystalline growth of Fe and Cr was monitored during the deposition by LEED. The Co film did not show clear LEED spots due to imperfect lattice match with the underlying layers. M(H) curves have been measured by MOKE. Subsequently the sample has been microstructured by optical lithography and Ar ion beam milling and investigated in the PEEM.

Fig. 5.10 shows the MOKE data of the Fe/Cr/Co trilayer taken at representative spacer thickness values. For $d < 0.75$ nm we observe parallel coupling, as shown in fig. 5.10 (left). For larger spacer thickness values antiparallel coupling of both ferromagnetic layers is detected. In zero field the antiparallel alignment of the layers is favoured and thus the magnetization of one of the layers is reversed already at negative fields (middle part of fig. 5.10). The right part of fig. 5.10 shows the situation typical for positions with a thicker spacer than 1.5 nm: One can see two independent switching fields of both layers. In between the magnetization is slightly rotating, indicating a canted magnetization configuration due to dominating biquadratic terms. Unlike the results reported by THEIS-BRÖHL *et al.* (1996) in our sample no parallel coupling was observed for spacer thickness values higher than 0.75 nm in spite of a similar thickness dependence of the measurements. This fact might be attributed to a reduced growth quality with higher interface roughness giving rise to a stronger

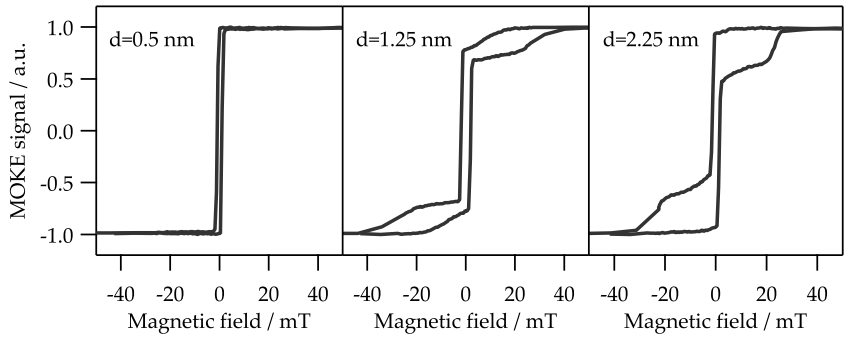

Figure 5.10: MOKE measurements of interlayer exchange coupled trilayers Fe/Cr/Co for different spacer thickness. The MOKE measurements correspond to a different coupling behaviour of the two ferromagnetic layers. Left: $d = 0.5$ nm parallel coupled, middle: $d = 1.25$ nm antiparallel coupled, right: $d = 2.25$ nm decoupled, independent switching.

biquadratic background. Similar suppression of positive bilinear coupling was reported for samples of Fe/Cr/Fe type (BÜRGLER *et al.*, 2001).

A common method for the extraction of coupling parameters from MOKE data is a fit of simulated M(H) curves to the data. The M(H) relationships can be generated by a minimization of the free energy. However, these models do not include hysteresis effects and thus fail here due to the high coercitivity of the Co layer (BUCHMEIER, 2009). Nevertheless from an estimate of the Co switching field at least the order of magnitude of the coupling constant can be derived using the relation $H_s = -\frac{J_1}{\mu_0 M_s t}$ (DEMOKRITOV, 1998) for dominating bilinear coupling. In the MOKE data of the 1.25 nm thick spacer the hystereses of the Co layer can be clearly discerned from the Fe hysteresis switching around zero field. The Co hystereses centres are shifted by about $\mu_0 H = 18\,\mathrm{mT}$. Using the above introduced formula and $M_s = 1.4 \cdot 10^6\,\mathrm{A/m}$ for Co, we get a coupling constant $J_1 = 5 \cdot 10^{-5}\,\mathrm{J/m^2}$ having the same order of magnitude as the results of THEIS-BRÖHL *et al.* (1996). For higher spacer thickness the Co switching fields are reduced. Therefore and due to the high hysteresis effects the switching fields cannot be easily evaluated anymore.

After the characterization with MOKE the sample has been investigated in the PEEM. Images of the magnetization in Fe and Co of single elements at characteristic positions of the sample are shown in fig. 5.11(a). The elements have been imaged using XMCD at the Fe and Co L_3 absorption edges. The PEEM images correspond to the MOKE measurements discussed above. The images from the Fe bottom layer reveal regular flux-closure domain patterns with four triangular or rectangular domains, in which the magnetization is aligned along one of the four magnetocrystalline easy axes in iron. As discussed in sect. 2.4, the formation of such four-domain patterns is

due to a stray field minimization confining the magnetic flux into the element. The ground state due to the stray field energy is given by the Landau state with four triangular domains magnetized parallel to the element edges, as shown in the left and right pictures in fig. 5.11(a). In these cases the magnetocrystalline easy axes have been oriented parallel to the edges. The competition of stray field energy and magnetocrystalline energy leads to the flux-closure pattern with rectangular domains, that can be seen in the middle picture. Here the stray field is reduced by the formation of four domains and thus reducing the integral magnetization to zero, but the magnetocrystalline anisotropy does not allow for a rotation of the magnetization parallel to the elements' edges. Therefore due to the formation of magnetic charges at the edges the stray field cannot be eliminated completely, as indicated in fig. 5.12 (a). The deviation of the flux-closure principle in the equilibrium configuration can be easily understood by effective field considerations: Using literature values for the anisotropy constant $K_1 = 48000\,\mathrm{J/m^3}$ and the magnetization $M_s = 1.7 \cdot 10^6\,\mathrm{A/m}$ (WIJN, 1991), the anisotropy field is $\mu_0 H_{\mathrm{ani}} = 60\,\mathrm{mT}$, while the demagnetizing field using an in-plane demagnetizion factor of $N_x = 0.0025$ calculated by the AHARONI formula (1998) is with $\mu_0 H_d = 5\,\mathrm{mT}$ significantly smaller, i.e. the influence of the magnetocrystalline anisotropy prevails.

The comparison with the images from the Co top layer reveals the coupling character between the two layers. For a low spacer thickness of $d = 1\,\mathrm{nm}$ an inverted image of the magnetization distribution in the bottom layer is observed. As already inferred from the MOKE measurements in this thickness range Fe and Co couple antiparallel. For a larger spacer thickness (centre) a different situation appears, where the Co magnetization is rotated by 90° relative to the Fe domains. Regarding biquadratic energy terms rotations around 90° both clockwise and counter-clockwise yield the same coupling energy, thus for a given Fe-magnetization two configurations in the Co layer are possible and we can observe eight domains in Co coupled to the four domains in Fe. The reason for the occurrence of a higher number of domains in the Co layer can be attributed to the flux-closure principle. A simple 90° rotation of the Fe magnetization would give rise to domain walls with head-to-head or tail-to-tail configurations in the Co layer. As indicated in fig. 5.12(b) these configurations are effectively avoided and flux-closure is conserved to a large extent.

For a spacer thickness of 2.5 nm the Co domain pattern does not show any similarity to the Fe domains anymore. Such irregular patterns may also be observed in single polycrystalline Co films. Thus, one can conclude that both layers behave as in the uncoupled case, which was already deduced from the MOKE measurements showing two separate switching fields. This means that the coupling strength for this thickness must be smaller than the intrinsic anisotropy of the Co layer.

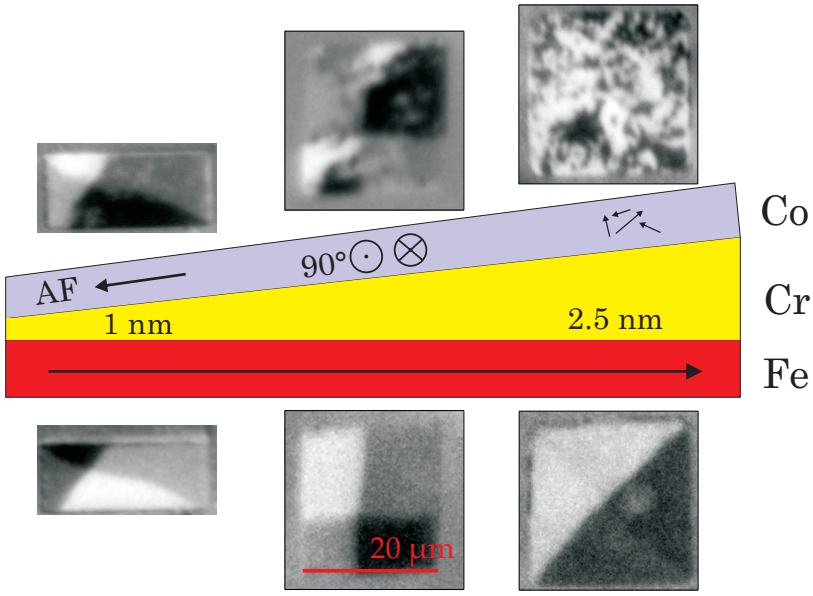

(a) Fe/Cr/Co

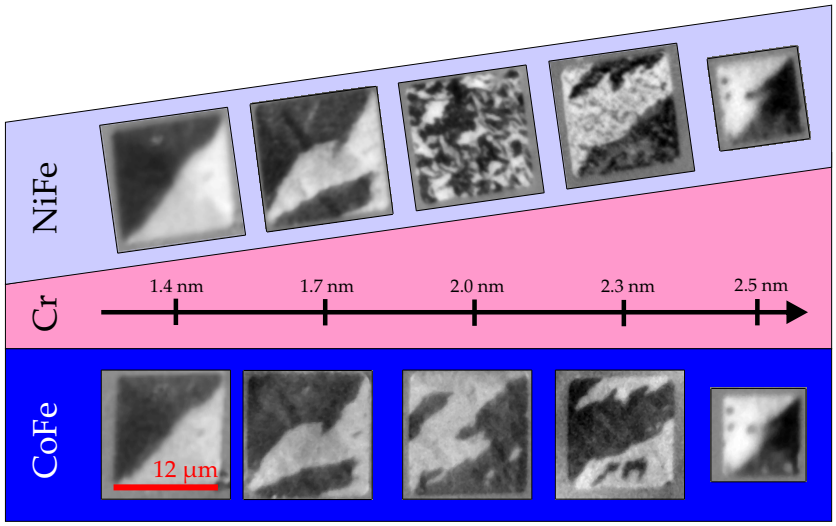

(b) CoFe/Cr/NiFe

Figure 5.11: PEEM measurements of interlayer exchange coupled trilayers Fe/Cr/Co (a) and CoFe/Cr/NiFe (b) for different spacer thicknesses. Due to the element-selectivity of the PEEM method the magnetization in both ferromagnetic layers is probed independently and the oscillatory coupling can be studied.

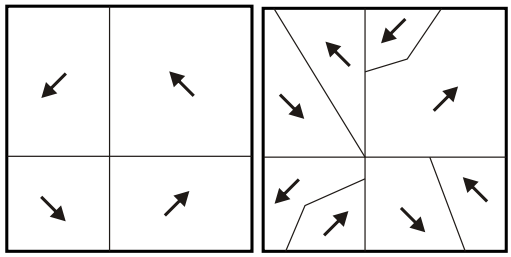

(a) Fe (b) Co

Figure 5.12: Illustration of the domain patterns from the bottom Fe layer (a) and the top Co layer (b) in a region with perpendicular interlayer coupling.

5.2.2 CoFe/Cr/NiFe trilayers

The measurements on the Fe-based trilayers show that the magnetization configuration is strongly influenced by the orientation of the magnetocrystalline easy axes. As shown in fig. 2.3, the anisotropy constants in Fe can be tuned by alloying it with Co without losing the lattice match to the neighbouring layers Ag and Cr. Thus, in order to study an interlayer-exchange coupled trilayer without the influence of magnetocrystalline anisotropy we have replaced Fe by $Co_{50}Fe_{50}$, where the anisotropy constant K_1 is supposed be significantly smaller. In order to retain chemical contrast between the two layers, Permalloy ($Ni_{80}Fe_{20}$) was chosen for the top layer. In this manner, we could image the magnetization of the bottom layer at the Co L_3 and the top layer at the Ni L_3 absorption edge. CoFe was deposited by co-evaporation of the pure metals Co and Fe, while Permalloy was deposited from compound material. The chemical composition was checked by Auger electron spectroscopy (AES). The thickness of the CoFe film was chosen as 5 nm, while the NiFe thickness had to be lower in order not to block photoelectrons from the bottom layer.

Again, the influence of coupling on the quasistatic hysteresis characteristics was investigated by MOKE measurements. Characteristic M(H) curves are displayed in fig. 5.13 and show a drastic sensitivity on the spacer thickness: At $d = 0.5$ nm and $d = 0.75$ nm the system has a rather high coercitivity probably due to perpendicular coupling, a higher interlayer thickness of $d = 1.75$ nm leads to a parallel coupling of the layers with the M(H) curve having sharp edges indicating a simultaneous switching of both layers. For $d = 2.5$ nm additional shifted hysteresis loops are forming due to a second range of antiparallel coupling, while at $d = 4$ nm the remagnetization curve is determined by a rotation of the magnetization rather than an instant switching, probably due to biquadratic copuling terms. Thus, in contrast to the Fe/Cr/Co film we observe real oscillatory coupling with both regions of parallel and antiparallel coupling of the two ferromagnetic layers. The coupling period can be deduced from the spacer thickness dependence of the coercive field as $\lambda \approx 2.0$ nm lying in the range of the long coupling period observed in Fe/Cr/Fe trilayers. The occurrence of positive bilinear coupling in contrast to the above discussed system can be attributed

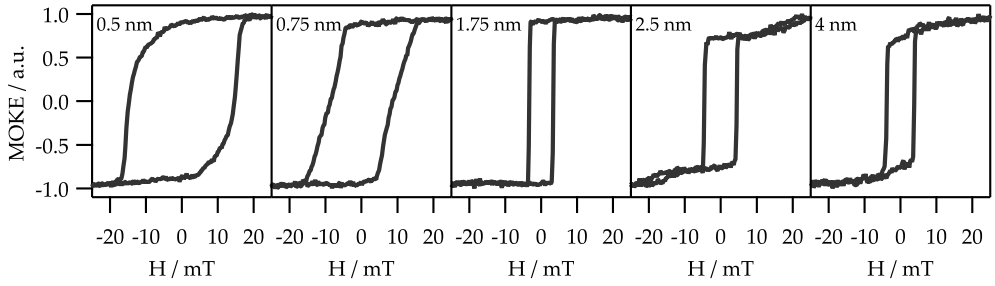

Figure 5.13: MOKE measurements of interlayer exchange coupled trilayers CoFe/Cr/NiFe for different spacer thickness. The MOKE measurements correspond to different coupling behaviour of the two ferromagnetic layers.

to a less pronounced biquadratic background leading to a stronger influence of the bilinear coupling.

Due to the high coercive field of the CoFe layer, the coupling constant can be only determined approximately as in the Fe/Cr/Co case. In the MOKE measurements taken for antiparallel coupling at $d = 2.5\,\mathrm{nm}$ two hystereses can be distinguished with a splitting of ca. 17 mT corresponding to a coupling constant of $J_1 = -2.5 \cdot 10^{-5}\,\mathrm{J/m^2}$.

The PEEM images of the magnetization distribution are displayed in fig. 5.11(b) revealing the coupling of the CoFe and NiFe layers. In the investigated spacer thickness range parallel coupling (1.4 and 1.7 nm), a partly decoupled behaviour with very small domains resembling a "cow pattern" in the Permalloy layer (2.0 nm) and antiparallel alignment for higher spacer thickness (2.3 nm) are observed, confirming the oscillatory nature of the interlayer coupling. All the images from both layers show an increased fine structure of the magnetization patterns which might be attributed to the reduced magnetocrystalline anisotropy. Due to a higher extent of isotropy, the relative impact of other energy terms on the domain formation is more significant than in the Fe-based samples. However, growth imperfections give rise to fluctuations in the local anisotropy causing the magnetization fine structure.

Contrary to the situation in the decoupled Fe/Cr/Co structure, the domains in the CoFe/ Cr/NiFe trilayer are not completely independent from each other, as further investigations show. Plots with lines of constant magnetization have been generated for the images taken of the single layers. By overlaying the equi-magnetization lines from the top and bottom layer of one sample, correlations in the domain configurations can be studied. In fig. 5.14 various positions with a correlation of the domain wall position or the shape have been identified (marked by arrows). However, a clear coupling angle cannot be recognized, thus coupling is either fluctuating and partly dominated by competing energy terms such as anisotropy fluctuations or only

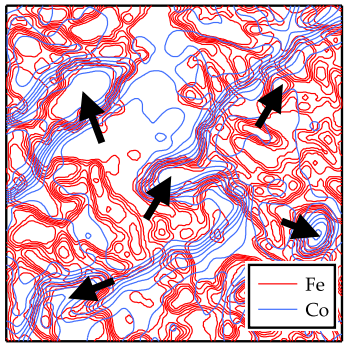

Figure 5.14: Layer-resolved lines of equal magnetization in a partly decoupled CoFe/Cr/NiFe trilayer. Regions with correlated domain wall position or domain shape are marked by arrows.

present at certain locations in the sample. This can be the case at the positions of domain walls in the bottom layer that is considered to dominate the trilayer system due its higher thickness. At a domain wall separating regions with $\boldsymbol{M_1}$ and $\boldsymbol{M_2}$ with interface normal $\boldsymbol{n}$ magnetic interface charges $\sigma_S = (\boldsymbol{M_1} - \boldsymbol{M_2}) \cdot \boldsymbol{n}$ are formed (HUBERT & SCHÄFER, 1998) giving rise to an increased stray field that may influence the domain configurations in the top layer. Calculations of THOMAS *et al.* (2000) have revealed magnetostatic fields of more than 100 mT near the domain walls of one layer in a spin-valve system. Such high fields are exceeding all internal field components and are thus expected to influence the domain structure of a neighbouring layer significantly. However, another reason for the occurrence of correlated domain wall positions is of extrinsic nature: Crystallographic defects in one of the underlying layers would influence the crystallinity also in the magnetic layers serving as a pinning centre for the domain walls in both layers.

5.3 Summary of the magnetostatic results

In this chapter the magnetization patterns in the equilibrium configuration of magnetic trilayers employing different coupling mechanisms and strength have been discussed. The micromagnetic configuration has been interpreted in terms of intrinsic material properties of the layers and the coupling of the magnetic layers.

As a prototypical system for magnetic tunnelling junction dual-Heusler trilayers with an MgO tunnelling barrier have been investigated. The XMCD measurements revealed a parallel coupling between the two magnetic layers, the origin of which is attributed to roughness-induced orange-peel-coupling. Important findings are the strong temperature and thickness dependence of the magnetic ordering. The measurements showed a new way of the investigation of the influence of crystalline ordering on the micromagnetic features. Between 200°C and 270°C the system was

found to undergo an irreversible change of the magnetic structure that is attributed to a partly development of the Heusler phase.

In addition, interlayer exchange coupled Fe/Cr/Co and CoFe/Cr/NiFe trilayers have been investigated. Depending on the spacer thickness the magnetic layers are parallel, perpendicular or antiparallel coupled to each other. The type of coupling as well as the occurrence of magnetocrystalline anisotropy have a decisive effect on the development of the micromagnetic structure in the films. The microscopic PEEM measurements have been correlated with MOKE measurements. It has been found that besides global interlayer coupling and other properties as anisotropy the micromagnetic structure is also influenced by locally varying stray fields around domain walls.

Due to their spin-valve character the interlayer exchange coupled trilayers are considered as interesting materials for application. For the implementation in devices the switching dynamics is an important property of the system, that is supposed to be strongly influenced from the coupling of the two magnetic layers. Especially the influence of locally inhomogeneous coupling conditions on the magnetization dynamics of the whole system are of great interest. Therefore time-resolved experiments have been carried out on these systems, the results of which will be presented in chapter 7.

The switching behaviour of the Heusler systems is another interesting topic. Due to their half-metallic character the magnetization dynamics in these systems is supposed to be determined by a reduced Gilbert damping parameter due to the non-availability of spin-flip processes (HEINRICH, 2004). Indeed, in recent experiments a reduction of the Gilbert damping was reported in half-metallic Heusler films (KUBOTA *et al.*, 2009). For their integration in magnetic tunnelling junctions, however, a decoupled behaviour would be feasible. Thus, the deposition conditions have to be improved first, before the magnetization dynamics of Heusler-based trilayers will be investigated in future experiments.

Chapter 6

Magnetization dynamics in single films – role of magnetocrystalline anisotropy

The interpretation of the magnetization dynamics of heterostructures requires a knowledge of the processes occurring in single layers in order to be able to distinguish reactions related to coupling and to intrinsic effects in the single layers, such as magnetocrystalline anisotropy. We have thus carried out measurements of the magnetization dynamics of magnetic single film elements. We have investigated Permalloy ($Ni_{80}Fe_{20}$) as a soft-magnetic material without considerable magnetocrystalline anisotropy and single-crystalline iron exhibiting a four-fold in-plane anisotropy. It will be shown that the presence of the anisotropy strongly influences the magnetodynamic response of the system. By the comparison of the response of the two materials the role of the magnetocrystalline anisotropy is related to the effect of the demagnetizing field on the magnetization dynamics. The measurements presented in this chapter have been carried out in the BESSY-II hybrid bunch mode using deflection gating, introduced in sect. 4.3. The results have been published in KAISER *et al.* (2009b).

6.1 Magnetically soft and isotropic permalloy

Fig. 6.1 shows snapshots of the magnetization distribution in a 10×10 µm^2 Permalloy element with 10 nm thickness taken at different time delays after the magnetic excitation by a 1 ns long Gaussian field pulse, shown in the bottom panel of fig. 6.2. The magnetodynamic response of the Permalloy microstructure is characteristic for a low-anisotropic material as known from previous experiments by SCHNEIDER *et al.* (2004) and SCHÖNHENSE *et al.* (2006a). The equilibrium state is a Landau flux-closure

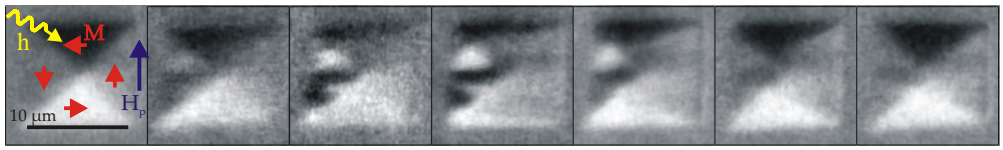

Figure 6.1: Pictures of the transient domain patterns in a 10×10 µm^2 Permalloy structure at different delays after magnetic field pulse excitation. The directions of the local magnetization and the external field pulse are marked with red and blue arrows.

state consisting of four triangular domains. On closer examination of the domain structure in fig. 6.1 (0 ns) the two grey domains (left and right) show a slight substructure with darker regions. This magnetization ripple is due to fluctuations of the magnetocrystalline anisotropy leading to local deviations of the magnetization direction. However, the domain formation is globally dominated by the demagnetizing field and thus the mean magnetization direction in the four clearly discernible domains is aligned parallel to the edges.

Under the application of the magnetic field pulse the black and white domains that are oriented perpendicular to $\boldsymbol{H_p}$ are subject to a torque $\boldsymbol{T} = \mu_0 \boldsymbol{M} \cdot V \times \boldsymbol{H}$ and thus shortly after the onset of the pulse the local magnetization vector is rotated towards the field direction $\boldsymbol{H_p}$. The domain on the right hand side of the structure with the magnetization oriented parallel to the field is growing by moving its domain walls to the left, while in the domain on the left a characteristic stripe pattern is formed due to incoherent rotation processes. By this process the area with energetically unfavourable antiparallel alignment of $\boldsymbol{M}$ and $\boldsymbol{H_p}$ is reduced. In an ideal defect-free sample such stripe patterns could not be observed, since the domain oriented 180° to the external field would experience no magnetic torque. A slight rotation of the domain out of the antiparallel direction would create a small torque acting on the whole domain in one direction. However, the magnetization fluctuations also lead to the generation of torques with opposite sign acting on neighbouring sub-domains. Similar, but less pronounced stripe patterns are formed in the domain on the right during the trailing edge of the excitation pulse ($t = 1.5 - 2$ ns). The reason for this behaviour is the formation of a new transient equilibrium state under the presence of $\boldsymbol{H_p}$. As discussed in sect. 2.5, the torque determining the motion of the magnetization vector does not only depend on the external field $\boldsymbol{H}_{\text{ext}}$ but on an effective magnetic field $\boldsymbol{H}_{\text{eff}}$ including also internal field terms such as the coupling, demagnetizing or anisotropy field. When the external field is decaying, the effective field is dominated by the demagnetizing field, which is oriented antiparallel to the magnetization direction. Thus, on the trailing edge of the pulse the effective field is oriented opposite to the field during the rising edge and the effective torque is exerted on the right domain creating similar stripe patterns. At the edges of the structure, again, the influence of the demagnetizing field is visible. In the edge regions the magnetization vector al-

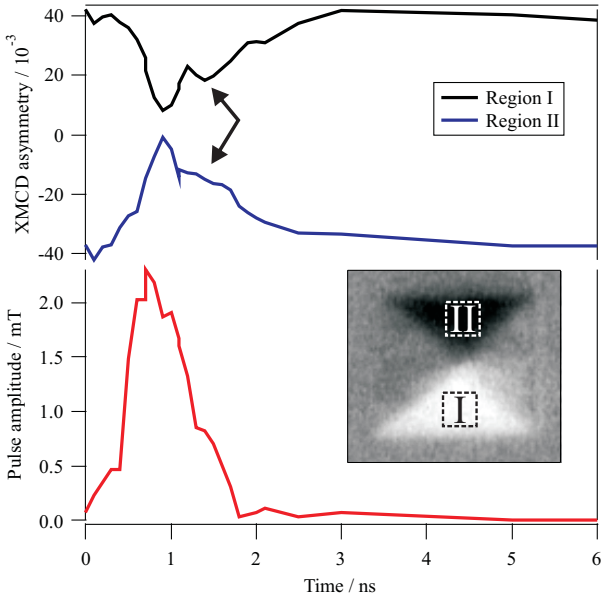

Figure 6.2: Temporal evolution of the magnetization in the 10 × 10 µm^2 Permalloy element (inset). The XMCD signal has been integrated over the regions I and II and is plotted against the temporal delay (top). The excitation pulse as measured on the CPW is shown in the bottom panel. The relaxation of the magnetization rotation is superimposed by oscillations (marked by arrows).

ways remains aligned parallel to the edges, because this avoids magnetic charges at the boundaries yielding a high stray field.

The temporal evolution of the XMCD signal integrated over areas inside the two domains experiencing the highest torque (shown in the inset) is plotted in fig. 6.2 (top). Both domains exhibit a rotation of the magnetization towards the magnetic field pulse during the rising edge of the pulse. This rotation leads to a decrease of the measured XMCD values. Shortly after the peak value has been passed, the system relaxes back towards the Landau configuration. During the relaxation process additional oscillations of the magnetization are observed (marked by arrows), which can be ascribed to the excitation of precessional eigenmodes in the corresponding domains. Due to the negligible anisotropy the frequency of the uniform mode is of the order of 1 GHz. The Fourier transform of the ns-long excitation pulse has significant frequency components in this range and thus an excitation of eigenmodes is rather probable, as shown by SCHÖNHENSE *et al.* (2006a).

The process of magnetization relaxation takes place on a longer time scale than the initial rotation towards the field. The origin for this slow-down lies in the existence of the above-mentioned stripe-patterns, also referred to as "blocking patterns" (CHUMAKOV *et al.*, 2005). Since neighbouring domains in such stripe patterns are dipolarly coupled to each other and separated by partial domain walls, they block themselves from relaxation into a mono-domain state.

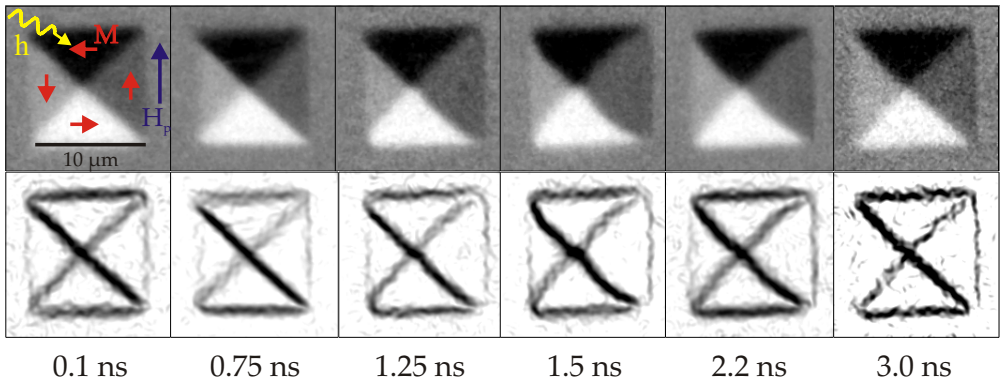

Figure 6.3: Images of the domain pattern in a 10x10 µm^2 iron element as a function of time delay after magnetic excitation. The directions of the local magnetization and the external field pulse are marked with red and blue arrows. The pictures in the bottom row have been obtained by an edge detection algorithm in order to emphasize the position of the domain walls. The pictures for $t = 1.25$ ns, $t = 1.5$ ns and $t = 2.5$ ns clearly show the bulging of the domain walls and a displacement of the vortex to the left.

6.2 Iron films with magnetocrystalline anisotropy

In contrast to Permalloy, iron films exhibit a four-fold in-plane magnetocrystalline anisotropy that strongly affects the micromagnetic behaviour, as already discussed in sect. 5.2. Images of the magnetic domain pattern in a $10 \times 10\,\mu m^2$ Fe element with a thickness of 10 nm are compiled in fig. 6.3. Again, in the ground state a Landau configuration is observed with the four easy directions oriented parallel to the element edges.

As a reaction on the magnetic field pulse no sizeable rotation of the magnetization in any of these four domains is observed during or after the magnetic field pulse. Instead one can see a bulging of the domain walls and a displacement of the vortex core to the left (maximum at $t = 1.5$ ns). By this bulging and displacement effect the domain on the right hand side with the local magnetization oriented parallel to the unipolar field pulse is growing at the expense of the domain with antiparallel magnetization components (left hand side) and thus the magnetization integrated over the entire element develops a finite component parallel to the pulse direction reducing the Zeeman energy.

The reason for the difference in the magnetodynamic behaviour between the Permalloy and iron elements can be traced back to the magnetocrystalline anisotropy. Since Permalloy exhibits only negligible magnetocrystalline anisotropy, the magnetization can freely rotate towards the external field. In epitaxial iron films the magnetization is strongly pinned to one of the four easy directions. By minimization of the total free

energy the expected rotation angle can be estimated. Neglecting other energy terms the minimization of

$$f_{\text{Zeeman}} + f_{\text{ani}} = -\mu_0 M_s \cdot H \cdot \sin(\phi) + 2K_1 \sin^2(\phi) \tag{6.1}$$

leads to a rotation of $\phi = 5.1^\circ$ ($\mu_0 H = 5\,\text{mT}$, $M_s = 1.7 \times 10^6\,\text{A/m}$, $K_1 = 4.8 \times 10^4\,\text{J/m}^3$). Such small rotation angles give rise to only a few percent of XMCD change and are thus not resolvable in these measurements due to the limited signal-to-noise ratio. Domain wall motion, however, provides another channel for the Zeeman energy reduction without a penalty in anisotropy energy. Thus, by an increase of the domain area oriented parallel to the pulse the Zeeman energy can be further decreased.

The reason for the occurrence of the bulging instead of a regular displacement of the domain wall to the left lies in the nature of the demagnetizing field. Of course, without considering demagnetizing field effects, domain walls could move freely and the Zeeman energy increase would be compensated by growth of the parallel domain under minimization of the domain wall length. However, at intrinsic and extrinsic domain boundaries such as domain walls and element edges, respectively, magnetic charges are generated that give rise to a stray field whose occurrence is penalized by an energy increase. Thus, a displacement of the domain walls out of the element corners is highly unfavourable. Moreover, due to the out-of-plane magnetization components the vortex core is forced on an oscillatory path rather than a perpendicular displacement. Therefore, by a motion of the domain wall end points the Zeeman term cannot be reduced since both end points are fixed by other mechanisms. The system chooses to increase the domain area oriented parallel to the pulsed field by a bending of domain walls. Using this configuration both the creation of asymmetric walls and the generation of magnetic charges at the element boundary are avoided and the additional cost due to longer domain walls is compensated by the gain in Zeeman energy.

Fig. 6.4 illustrates the temporal evolution of the displacement of the domain wall center (top) in a $20 \times 10\ \mu\text{m}^2$ large Fe element (shown in the inset) as a reaction on the magnetic field pulse (bottom). For every image the displacement of the center compared to a straight line between its end points has been measured and the derivative was calculated from the smoothed experimental data (middle panel). Starting with the onset of the field pulse the domain wall center begins to accelerate until it reaches a domain wall velocity of ca. 400 m/s. Then the domain wall velocity reaches a plateau until the field pulse has completely decayed. It relaxes with a lower speed of 100-200 m/s until it has the form of a straight line again.

Remarkably, the maximum domain wall displacement is considerably shifted with respect to the maximum excitation field by 700 ps. We attribute a combination of two effects as the reason for this rather long delay: The first one is the suppression of a precessional motion with higher amplitude – as observed in the Permalloy case. The

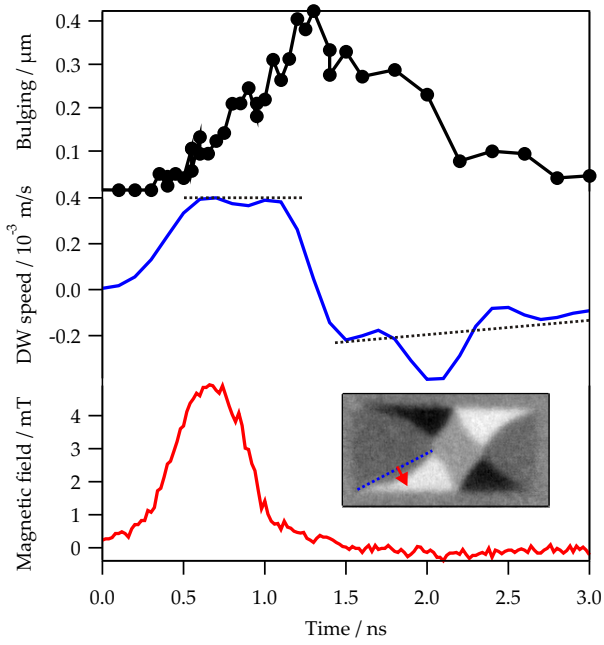

Figure 6.4: Effect of domain wall bulging (top) in a $20\times10\,\mu m^2$ Fe element (inset) as a response to the magnetic field pulse (bottom). The middle panel shows the derivative of the domain wall displacement. The plateau of constant velocity and the relaxation speed are marked by the dotted lines.

high rotation angles occurring in the Permalloy sample give rise to high demagnetizing field components yielding a strong restoring force shortly after the excitation maximum. In the iron sample the anisotropy effectively suppresses a high-angle magnetization rotation so that the Zeeman energy, that is deposited into the spin system, is only consumed by the rather slow domain wall motion process. Thus, the domain wall motion continues until the deposited energy is completely dissipated. The second effect leading to the long delay is the small damping parameter of $\alpha = 0.003$ in iron (SCHECK *et al.*, 2006) defining the characteristic time scale, on which the Zeeman energy is dissipated. This time scale is given by (YUAN & BERTRAM, 1991)

$$\tau_{DW} = \frac{1}{\gamma\mu_0 M_s \alpha}. \tag{6.2}$$

For iron with $\mu_0 M_s = 2.2\,T$ the time constant is $\tau_{Fe} \approx 850\,ps$ being of the same order of magnitude as the temporal shift of 700 ps derived from our measurements.

The plateau in the plot of the domain wall velocity might be attributed to the Walker limit. The domain wall velocity in the regime of viscous motion increases linearly with the external field up to the Walker breakdown field (eq. (2.38)). With typical values of $\alpha = 0.003$ and $M_S = 1.7\times10^6$ A/m the Walker field in iron is $\mu_0 H_W = 3.3\,mT$. This value agrees well with the field acting on the element when the domain wall acceleration stops.

We have simulated the micromagnetic behaviour of the iron element using OOMMF

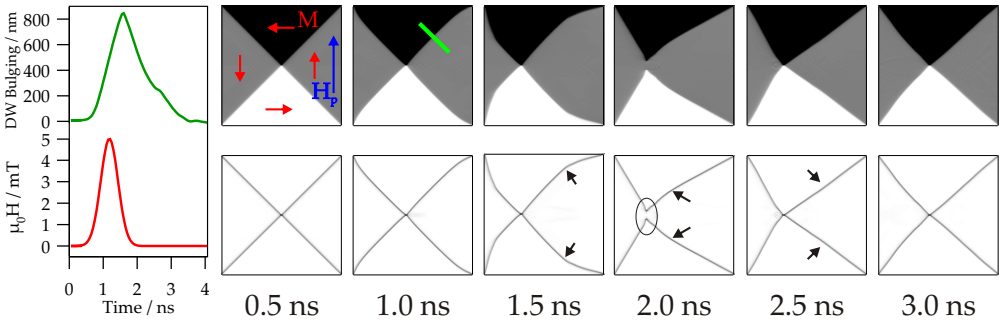

Figure 6.5: Simulations of the micromagnetic behaviour of a 5×5 µm^2 large Fe element with a thickness of 5 nm. The bottom row shows the domain wall positions. A bend in the domain walls (marked by the black arrows) is moving along the wall. The left panel compares the domain wall bulging measured along the green line with the applied magnetic field pulse

(DONAHUE & PORTER, 1999). All characteristic features of the measurements could be reproduced by the simulations, as compiled in fig. 6.5. The simulations enable us to get a more detailed view on the domain wall bulging: We find that the maximum displacement of the domain wall is not statically located in its center, but it is first created near the edges of the wall and is then moving along the domain wall. Furthermore, the simulations show that the bulge in the domain wall has the shape of a sharp bend rather than a round curve. Such sharp features have not been observed by the experiments, as well as the separation of the two grey domains at t=2.0 ns (marked by the oval). Therefore it is very probable that these features do not reproduce reality but are in fact an artefact of the simulations. In order to reach finite simulation times the micromagnetic simulations use a cell size of 20 nm averaging over all features occurring on a smaller length scale. However, the magnetostatic exchange length of iron is $l_{\mathrm{exc}} = \sqrt{A/K_s} = \sqrt{2A/\mu_0 M_s^2} \approx 3$ nm and thus significant magnetic interactions have to be expected below a length scale of 20 nm.

Therefore, the simulations have been repeated with a lower discretation size of 3 nm for an iron element of 1×1 µm^2 size (fig. 6.6). In contrast to the first simulations now the structure inside the domain wall is also visible. Furthermore, the out-of-plane magnetization of the vortex core is included in the simulation which is important for the correct description of the behaviour near the contact point of all four domains. Comparing the two sets of simulation data, the temporal evolution of the domain wall bulging is similar. However, the second set with a smaller discretation size does not show sharp bends in the domain walls and no separation of the domains at the vortex core. Thus, it is concluded, that the latter effect can be attributed to the averaging effect over small-distance interactions. Near the vortex core, where the magnetization is rotated out of the sample plane, this neglect may lead to strong deviations of simulation and reality. Regarding the bend in the domain wall no clear conclusion can be drawn: The smoother domain wall curvature in the second simulation set can

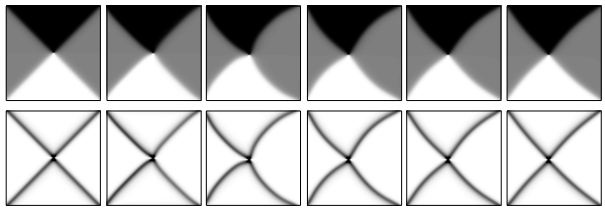

Figure 6.6: Micromagnetic simulations of a $1\times1\,\mu m^2$ Fe element with 1 nm thickness. Due to the smaller discretation size the simulations include the internal domain wall structure and do not show sharp domain wall bends.

also be attributed to the lower element size rather than the inclusion of small-distance interactions.

From a fundamental point of view no reason for the occurrence of the sharp domain wall bends can be found. Fig. 6.7 compares the energetics of a bulged domain wall with a homogeneous curvature and one sharp bend. The calculations include the negative Zeeman energy E_{Zeeman} proportional to the domain area and the positive domain wall energy E_{DW} increasing linearly with the domain wall length. The calculations show that the energetic minimum is reached for a curved domain wall. The Zeeman energy gain due to a higher area always compensates the higher domain wall length. For a different relative weight of E_{DW} and E_{Zeeman}, e.g. due to higher fields increasing the Zeeman term, the minimum is shifted on the displacement axis but the round domain wall remains energetically favourable. Thus these calculations do not explain the occurrence of domain walls with a sharp bend in the simulations. However, consideration of the inhomogeneous demagnetizing field and eventual changes in the internal structure of the domain wall during the motion may give rise to different energetics. This will have to be checked by upcoming aberration-corrected microscopes that will enable measurements with higher spatial resolution.

It has to be noted that similar domain wall bulging effects have also been observed by NEUDERT *et al.* (2007). They report of an undulation of the domain walls in Permalloy elements in a quasistatic external field, which is explained by spatially modulated anisotropy in the polycrystalline sample. For our experiments such random-anisotropy effects can be ruled out: On the one hand the silver bottom layer unambiguously defines the magnetocrystalline axes of the iron film due to the epitaxial growth, on the other hand this effect would not have been reproduced in the simulations, since OOMMF assumes perfectly crystalline samples.

6.3 Summary of the single layer experiments

This chapter concentrated on the interpretation of the magnetodynamic response of magnetic single film elements on an excitation with ns-long magnetic field pulses. The two materials, that have been studied as prototypical systems with and without magnetocrystalline anisotropy, showed distinctly different reactions due to their

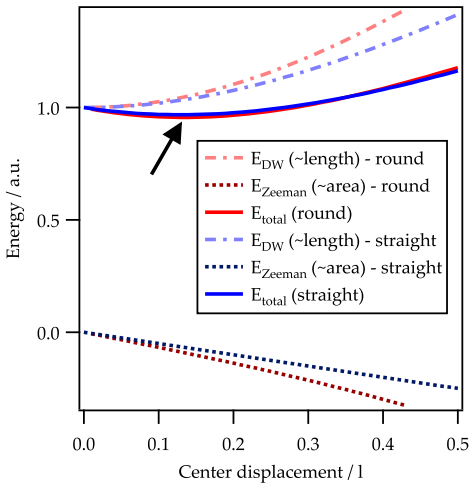

Figure 6.7: Comparison of the energetics of a round domain wall and one with a sharp bend. On the x axis the displacement of the domain wall centre compared to a straight line between its end points is shown in units of the end-point distance l. The arrow marks the energetic minimum.

intrinsic material properties. In Permalloy the demagnetizing field is the only sizeable component of the effective field determining the micromagnetic behaviour and thus the magnetization vector can freely rotate as a reaction on the external field. In iron, however, the micromagnetic behaviour is dominated by the magnetocrystalline anisotropy. Here the external field is only acting on the domain walls. Thus, the dominant reaction is a bulging of the domain walls, the temporal characteristics of which have been studied in detail. The measurements have been correlated to micromagnetic simulations reproducing the measured behaviour. An interpretation of the domain wall bulging effect could be given in terms of a lowering of the Zeeman energy with the domain wall motion partly being constrained due to a magnetostatic pinning at the element edges and at the vortex.

Chapter 7

Magnetization dynamics in heterostructures – effect of coupling phenomena

The core of this thesis is the investigation of magnetization dynamics in heterostructures. In this chapter various results on this topic will be presented. By both choice of materials and the excitation conditions different magnetodynamic processes can be studied. The first two sections concentrate on the magnetodynamic study of pseudo-spin-valve systems excited by ns-long field pulses. Here the competition between different remagnetization processes such as coherent rotation, domain wall motion and domain nucleation is discussed. In the experiments shown in the third section the time-scale of the exitation pulses was reduced by one order of magnitude and magnetic eigenmodes have been excited in the trilayer system. The last section deals with the fact that by the application of a sinusoidal field resonances in the ferromagnetic system can be excited allowing for spatially resolved ferromagnetic resonance (SR-FMR) experiments within a PEEM.

7.1 Domain wall motion in Fe/Cr/Co

In sect. 5.2 the interlayer exchange coupling of Fe/Cr/Co trilayers was introduced. The micromagnetic structure of the system was found to be significantly influenced by both the four-fold magnetocrystalline anisotropy of the Fe layer and the oscillatory interlayer coupling. The magnetodynamics of iron single layers studied in sect. 6.2 was limited to domain wall motion. Therefore, the temporal behaviour of the competition of anisotropy-induced domain wall motion and interlayer coupling can be investigated using the Fe/Cr/Co system. The following results have been acquired

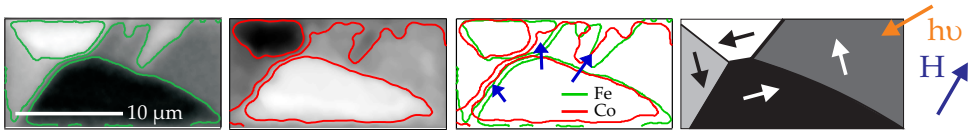

(a) Fe (b) Co (c) Domain walls (d) Fe (schematic)

Figure 7.1: Static domain structure in the Fe (a) and Co (b) film. The position of the domain walls (c) is slightly shifted in both films indicating coupling via the domain wall stray fields. Light incidence direction and magnetic field vector are indicated in (d).

with a 20×10 µm^2 large element consisting of a 10 nm thick Fe layer, a Cr spacer of 1 nm and 2 nm Co. The experiments have been carried out at the beamline ID8 at the ESRF in Grenoble (France). In the 16-bunch mode provided at the ESRF, the time between two subsequent light pulses of 176 ns is sufficiently long for the magnetic system to be in a reproducible ground state at the beginning of each pump-probe cycle and the photon flux is considerably high to be able to study buried layers with a good signal-to-noise ratio.

The two magnetic layers were found to couple antiparallel in the static case, as shown in fig. 7.1. However, comparing the magnetization patterns of Fe and Cr slight deviations from a strict antiparallel coupling are visible near the domain wall positions. Some of the domain walls in the top and bottom layers are shifted slightly with respect to each other. This behaviour can be attributed to the increased stray fields near the domain walls, which overcome the influence of the interlayer coupling. As pointed out in the previous chapter, domain wall stray fields can be as high as several 100 mT at a distance of a few nanometres and may thus easily overcome the coupling fields $H_{\mathrm{coupl}} = J/(\mu_0 M_s t)$ that are typically in the mT range.

First experiments with unipolar field pulses using the same set-up as used for the measurements of sect. 6.2 did not result in reproducible dynamics. Similar to the single Fe films a bulging of the domain walls was observed, but the domain walls showed no sign of relaxation. By subsequent pulses the deflection of the domain walls was not increased. The absence of a restoring force re-establishing an equilibrium state is attributed to a reduced demagnetizing field. The demagnetizing field of magnetic elements with a non-zero average magnetization is the major source of a restoring force that gives rise to domain wall motion reducing the average magnetization. In magnetically coupled multilayer samples this magnetostatic field is reduced when the single magnetic films are ordering non-parallel due to a local flux-closure of the stray fields of neighbouring layers. Therefore, bulged domain walls can be stabilized in antiparallel coupled trilayers. Moreover, the higher number of layers and interfaces in a multilayer sample may increase the number of defects acting as pinning centres for domain walls. Thus, trilayers have a higher probability that after the decay of the external magnetic field domain walls are pinned at a defect with an

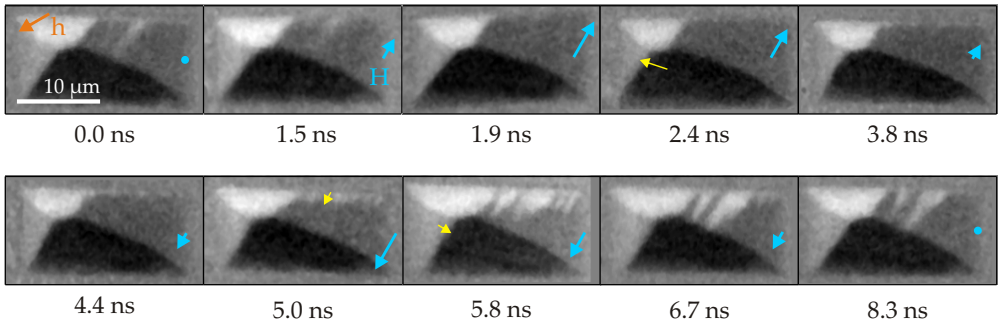

Figure 7.2: Images of the magnetization configuration of the Fe layer. The magnetodynamic response exhibits domain wall motion and growth of stripe domains (marked by arrows). The relative size and direction of the magnetic field is indicated by the blue arrows.

energy barrier that cannot be overcome by the residual restoring field. Due to the stroboscopic character the time-resolved PEEM method is limited to the study of reversible processes. As a consequence, bipolar field pulses have been applied to the samples in order to drive the system back into a defined ground state at the beginning of each pump-probe cycle.

Both layers show different reactions on the bipolar excitation. The images of the magnetodynamic response are shown in fig. 7.2 for Fe and fig. 7.3 for Co, respectively. The temporal characteristics and amplitude of the excitation pulse is displayed in the bottom panel of fig. 7.5. Just as in single Fe films magnetization rotation is effectively suppressed due to the magnetocrystalline anisotropy. The system lowers the Zeeman energy by domain wall motion increasing the area of magnetization components parallel to the field. The domain wall motion manifests itself in three different processes: The domain walls between the two dark and bright domains are bulging, the touching point of all four domains in the middle of the element is moving perpendicular to the pulse and in the top domain (dark grey) white stripe domains grow and shrink depending on the field direction. The former two effects can be understood in terms of the behaviour of a single Fe layer, while the latter one may be attributed to a coupling effect. In the region of the growing white stripes, the Co layer exhibits a spot of permanent darker intensity that may be attributed to a defect or a pinned domain. It has been shown that the large domain wall stray fields of a hard magnetic layer lead to the creation of 'quasiwalls' in a neighbouring soft magnetic layer (VOGEL *et al.*, 2005). They do not separate regions of different magnetization like a regular domain wall but it is a region where the magnetization is tilted away from the average direction (BIRAGNET *et al.*, 1966). External fields exert a torque on this tilted regions and rotate the magnetization towards the field direction. Quasiwalls can act as nucleation centres for new domains with the magnetization antiparallel to their neighbourhood, since they easily grow under the influence of an external field. Similar nucleation centres for antiparallel oriented domains are 360° walls created by

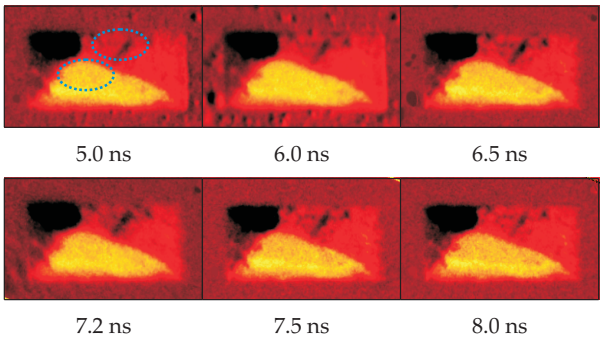

Figure 7.3: Images of the magnetization configuration of the Co layer. The colour scale has been changed for emphasizing the slight changes. Changing regions are marked by the dotted circles.

two 180° walls with opposite chirality. They are very stable up to high fields and grow under the influence of a magnetic field antiparallel to the surrounding domains (PORTIER & PETFORD-LONG, 2000). Thus, we propose, that the reason for the preferential growth of the white stripe domains in the top right Fe domain is a quasiwall or 360° wall in the Fe domain beneath a pinned domain in the Co layer.

The response of the Co film only partly follows the dynamics of the Fe film. Domain wall bulging is not observed, but in the region where the white stripes grow, the XMCD signal of the Co film is reduced. In fig. 7.3 a slight darkening of this region can be observed. This reaction is directed opposite to the magnetic field direction and the Fe reaction, where a growth of white domains is observed. Thus, it can be concluded, that the stripe growth in both layers is controlled by the thicker Fe layer and the antiparallel coupling between Fe and Co. This behaviour is consistent with the quasistatic MOKE measurements shown in fig. 5.10. For a spacer thickness range of 1 nm the antiparallel coupling is dominating up to external fields of 20 mT, which is significantly higher than the peak field of ca. 5 mT in our experiment. However, the magnetization in the stripe region is not oriented antiparallel to the Fe stripes. The small change of magnetic contrast in the Co layer is rather a sign of a slightly canted configuration of Fe and Co. This might be attributed to a competition between the external magnetic field and the opposite magnetic coupling suppressing the growth of 180° domains in the Co film.

The reaction of the Co layer is not exclusively controlled by the antiparallel coupling. Domain wall motion and bulging is *not* reproduced in the Co layer, as stated above. Furthermore, the large white domain at the bottom of the structure shows indication of a slight rotation towards the field direction. This effect is hardly visible in the images of fig. 7.3, but it can be emphasized by difference images removing all constant image contributions. Corresponding difference images have been generated for Fe and Co (fig. 7.4). The pictures have been computed by averaging over the pictures taken at positive and negative external fields for better statistics and subsequent subtraction of the negative from the positive field image. Both images have been normalized to the maximum XMCD contrast. The different scales in the Fe and

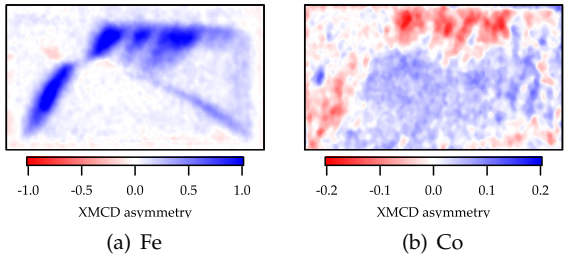

(a) Fe (b) Co

Figure 7.4: Difference images of Fe (a) and Co (b) visualizing the changes between the averaged response on positive and negative fields.

Co difference shows that the XMCD change in Fe is up to five times higher than in Co. This difference is an indicator for the underlying magnetization reversal mechanisms. While the Fe reaction is determined by domain wall motion yielding a magnetization change of 90° and more with an XMCD change of 100%, in Co only minor changes of the XMCD contrast of 5% are observed correlated to a magnetization rotation of ca. 3°. As expected due to the dominance of the magnetocrystalline anisotropy the Fe reaction is mainly determined by domain wall motion and stripe growth, but in the domain on the top right side of the structure it also shows a magnetization rotation of 5°. In the Co layer domain wall motion does not play a role, probably caused by a lower crystalline quality with more pinning centres hindering the domain walls to move.

Three different kinds of reactions on the external field can be identified in Co from the analysis of fig. 7.4(b): The above mentioned antiparallel rotation above the region of stripe-growth in Fe, a slight rotation parallel to the external field in the bottom domain and an antiparallel rotation at the bottom left domain wall. All three reactions can be attributed to different origins. As stated above, the rotation antiparallel to the magnetic field in the top domain is caused by the white stripe growth in the Fe layer leading to an opposite reaction in Co due to the antiparallel coupling. The slight magnetization rotation in the large domain is a direct rotation towards the field direction being partly suppressed by the antiparallel coupling to the Fe layer. The slight rotation near the bottom left domain wall can be also attributed to the coupling to the bottom layer. In this region the Fe layer shows a strong domain wall bulging increasing the domain area with the energetically favourable directions but due to less mobile or pinned domain walls in the Co layer, the domain wall motion cannot be reproduced in the top layer. However, the antiparallel coupling between the two layers induces a rotation of the Co magnetization in this area.

The temporal characteristics of the domain wall motion in the Fe layer and the small-angle magnetization rotation in the Co layers are compiled in fig. 7.5. The domain wall motion has been analysed by calculating the displacement of an edge in a line profile along selected axes (see left inset) and the magnetization rotation has been measured by integrating the XMCD signal over selected regions of interest (right inset). Both types of measurement have been carried out by automatized algorithms.

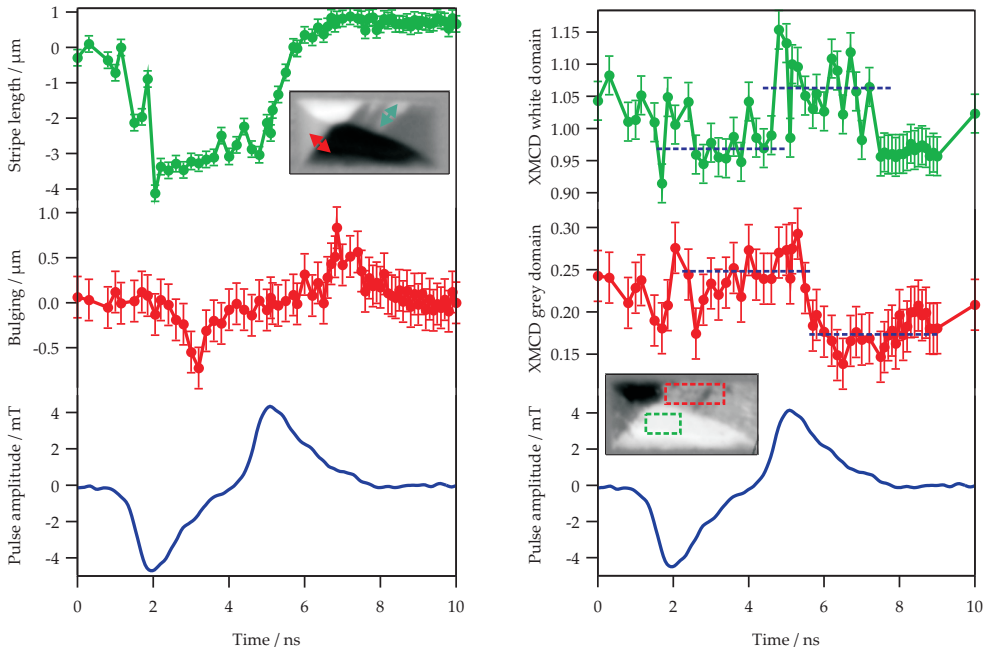

(a) Fe (b) Co

Figure 7.5: Element-selective magnetodynamic response on the field pulse (bottom panels). (a) Fe layer: Length of the white stripe (top) and domain wall bulging (middle), (b) Co layer: Averaged XMCD in the region of the stripe growth (middle) and the large bottom domain (top). The size of the error bars has been determined from the standard deviation of edge positions (a) and grey values (b) of unmagnetic background features. Insets: Integration regions and measurement axes. The dashed lines denote the levels between which the system is switched under the influence of magnetic field pulse.

In order to be able to distinguish the magnetodynamic response from fluctuations in the data, error bars have been added to the data points. The size of the error bars has been determined from the standard deviation of nonmagnetic features like the displacement of edges and fluctuations of the integrated signal on the substrate area.

The temporal evolution of the domain wall bulging and growth of the stripe domains shown in fig. 7.5(a) shows different characteristics indicating different mechanisms. While the stripe growth is switching between two states simultaneously with the field peaks, the domain wall bulging resembles the behaviour seen in single Fe films. Here the maximum displacement is delayed relative to the maximum field by more than one nanosecond and the domain wall quickly relaxes to a ground state. The domain wall velocities as visible from fig. 7.5(a) differ by a factor of five. The centre of the bulged domain wall moves with 600 m/s, which is consistent with the results from

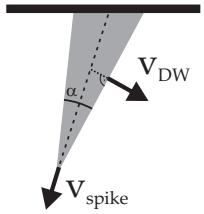

Figure 7.6: Illustration of the measured velocity v_{spike} and the real domain wall velocity v_{DW} given by the projection of v_{spike} on the domain wall normal: $v_{\text{DW}} = \sin(\alpha/2) \cdot v_{\text{spike}}$.

the single Fe layer, while the velocity the stripe spike is of the order of 3000 m/s. However, this rather high value and the quick formation of the stripes suggest that the stripe domains are not nucleated from a monodomain phase but rather grow sidewards from quasiwalls that cannot be resolved in the PEEM images. Thus, the spike velocity cannot be considered the true velocity of the stripe domain wall. The real domain wall velocity is given by the projection of the spike velocity on the domain wall normal. If measured perpendicular to the stripes the growth velocities reduce to values around 600 m/s (see fig. 7.6 for an illustration).

In fig. 7.5(b) the time-resolved XMCD modulations measured in the Co layer are displayed. The amplitude of the changes in both regions is in the range of $\pm 10\%$ corresponding to an average magnetization rotation of ca. 6°, but as discussed above both effects are oriented oppositely. Both domains show a strong change near the positive field peak. As the white domain quickly relaxes, the rotation of the grey domain is nearly constant. This behaviour is consistent with the interpretation by the coupling to the bottom layer. Also in the Fe film the white stripes are stable after the decay of the external field.

It is worthwhile to study the behaviour in the top domain in more detail. Fig. 7.7 visualizes the changes observed in this region. In this graph histograms of the XMCD value distribution of the single pixels have been plotted against the time and are compared to the field profile, allowing for the analysis of the magnetization angle distribution for every time-step. The colour of a given point indicates the number of occurrence of pixels with the specific XMCD value. The dominant line at ± 0.3 corresponds to the ground state magnetization of the studied domain. Under the influence of the negative field it is compressed in both layers due to the removal of the stripe domains. During the time interval between t=2 ns and t=4 ns irrespective of a few fluctuations the domain has a uniform magnetization. This situation is significantly changed under the influence of the positive field which leads to the quick growth of the stripe domains. The stripe growth yields a broadening of the pixel distribution in the histograms which is more pronounced in the Fe signal. However, the stripe growth does not manifest itself in one additional line at a constant grey level, which would be expected for the growth of one additional domain with constant magnetization, but it is rather superimposed by a continuous angle distribution of the stripe domains. The temporal characteristic is similar in both layers confirming the interpretation in terms of coupling between them. From the histograms also a small displacement of

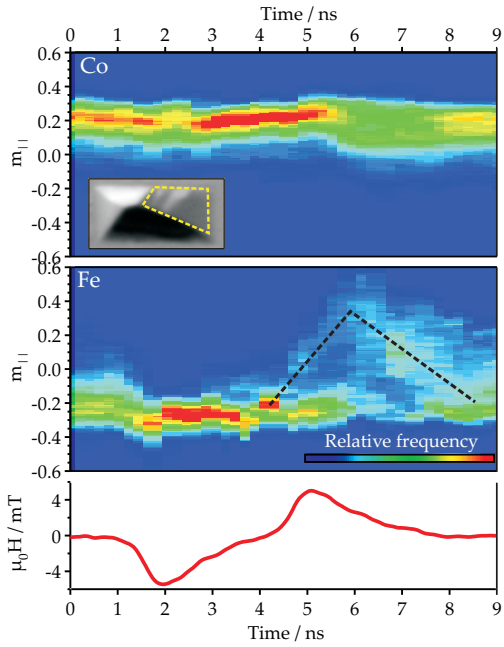

Figure 7.7: Smoothed time-resolved distribution of pixel XMCD values in the stripe growth region. For every time step histograms of the pixel grey values inside the region marked in the inset has been generated. The colour scale corresponds to the number of pixels within the specific interval. The dashed line in the bottom panel is guide to the eyes.

the background magnetization from its initial value is observed due to a rotation by a few degrees.

7.2 Coherent rotation and domain wall motion in CoFe/Cr/NiFe

For the studies on a trilayer stack with less pronounced magnetocrystalline anisotropy CoFe/Cr/NiFe was chosen. As known from the magnetostatic measurements discussed in sect. 5.2 this material combination shows similar oscillatory interlayer coupling as the Fe/Cr/Co system due to the structural similarity. However, both layers employ significantly different coercive fields. Under the magnetic field pulse the influence of this pseudo-spin-valve behaviour on the magnetodynamic response on the system can be studied. The measurements have been obtained from a trilayer stack with a 2.5 nm thick Cr interlayer inducing parallel coupling of the two magnetic films (5 nm CoFe and 2 nm NiFe).

XMCD images that have been taken along the bipolar field pulse are compiled in fig. 7.8. For highlighting the changing areas of the magnetic structure also difference images between the initial magnetic state and the excited states have been generated. The magnetic ground state of the 8 µm large element is a Landau flux-closure

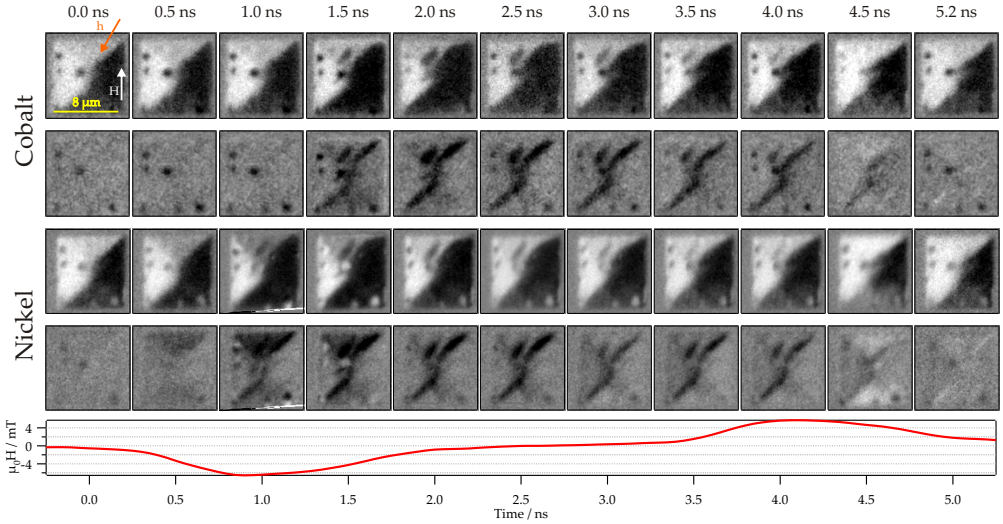

Figure 7.8: XMCD images of the layer-resolved magnetization pattern. For both layers the first row shows the magnetization at a fixed time step, the second row shows the difference to the ground state magnetization. The dark spots on some of the images are particles that appear on some images due to a varying aperture position. The bottom panel shows the time profile of the magnetic field pulse.

structure with some deviations from ideal triangular domains due to fluctuations of the local anisotropy. At the surface of the structure several particles are visible that are also visible in the XMCD and difference images. However, they are not supposed to influence the magnetic structure or the magnetodynamic behaviour but due to their three-dimensional structure the angular photoelectron distribution emitted from such particles can be highly anisotropic yielding an apparent displacement on images taken at different positions of the contrast aperture.

Under the influence of the bipolar magnetic field pulse three effects can be identified in both layers (see illustration in fig. 7.9): Magnetization rotation in the two domains oriented perpendicular to the magnetic field (top and bottom domain), domain wall bulging leading to a growth of parallel oriented domains and the nucleation of a small stripe domain in the top domain. The temporal characteristics is different for all three effects as well as the rotational amplitudes in both layers. The temporal characteristics of all three effects are compiled in fig. 7.10 and 7.12.

As known from other samples where the magnetization is not constricted by the magnetocrystalline anisotropy, the magnetization is rotated towards the magnetic field direction. If the external field is varying, the magnetization is moving on a spiral trajectory precessing around the momentary effective field direction. Typical precession frequencies of magnetic microstructures lie in the range of several GHz and thus the

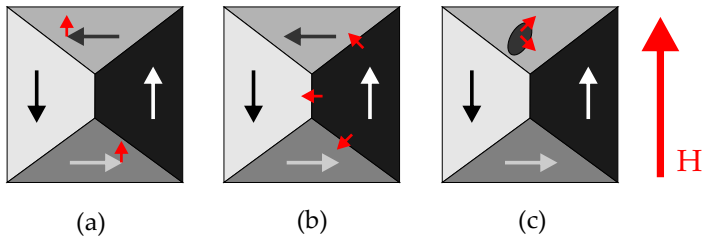

Figure 7.9: Illustrations of the three different magnetodynamic processes observed in the CoFe/Cr/NiFe trilayer system: (a) Rotation of the magnetization in the domains perpendicular to H, (b) Domain wall motion increasing the magnetization area parallel to H, (c) Growth of an additional domain.

excitation signal with a FWHM of 1 ns that is used in this experiment does not contain significant frequency components for exciting precessions. Therefore, in this case the magnetization follows the excitation in a driven quasi-static way and no delays between field and rotation peaks are observed.

In the top domain the first negative pulse creates a small stripe domain that grows under the influence of the magnetic field. Following the interpretation of the previous section, the fast creation times and small fields that are necessary for the growth indicate that the stripe domain is not nucleated from a homogeneously magnetized domain but it is created and growing from reminiscent pseudo or 360° walls that are not fully annihilated by the positive pulse. By putting integration areas on the stripe domain and the neighbouring area that is rotating towards the field direction the different remagnetization and reversal times of both coherent rotation and domain wall motion processes can be studied. The values integrated over three different areas have been plotted for both layers in fig. 7.10. It is a striking result that the magnetization vectors in both layers react differently on the external field. The correlation of both layers is different for the three integration areas. Regarding the temporal structure of the magnetization rotation the soft-magnetic NiFe layer reacts faster on the field pulses. Both rising and falling edges of the NiFe response are steeper than for the CoFe layer. The relaxation times of the integrated XMCD values are very different for the integration area with the stripe domain and the two areas exhibiting magnetization rotation. While the rotation directly follows the profile of the external field pulse, the stripe domain is still present after the decay of the pulse and is slowly disappearing between the two pulses.

Furthermore, the rotational amplitudes are different for both layers and for different remagnetization mechanisms. Via the relation $A_{\mathrm{XMCD}} \propto \cos(\phi)$ the angle ϕ between light polarization vector and magnetization vector can be obtained from the XMCD asymmetry A_{XMCD}. In the case of the NiFe layer the free magnetization (blue curves) is rotated by $35° \pm 5°$ by both field pulses. At the position of the stripe domain (red curve) both during creation by the first pulse and annihilation by the second pulse

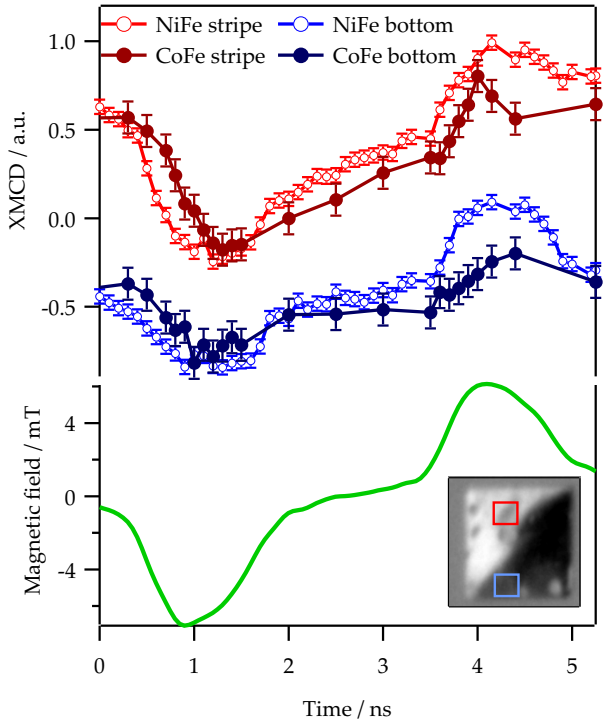

Figure 7.10: Layer-resolved XMCD values integrated over two different regions of interest (marked in the inset) in the two domains that are initially aligned perpendicular to the field pulse. The red integration area is integrating over the region where a stripe domain appears, while the magnetization in the blue integration area is rotating. The size of the error bars has been obtained from the standard deviation of unmagnetic areas.

rotational amplitudes of more than 50° are measured. However, an exact determination of the magnetization angle of the stripe domain is not possible due to the limited spatial resolution of the order of the stripe width.

In the subjacent CoFe layer, the rotational amplitudes of $25° \pm 5°$ under the first pulse are only slightly smaller than in the soft-magnetic NiFe layer. However, the speed of magnetization change is distinctly lower in the CoFe layer leading to a shift of the CoFe curve compared to the NiFe curve by 250 ± 50 ps. Due to the higher relaxation times in the CoFe film, the magnetization of the bottom film has not completely returned to the initial state when the second pulse starts to rise. Thus at the time of the second pulse the difference of the two magnetization values is even higher.

The different switching speeds of the magnetization in both layers can be understood by the empirical model for the switching time

$$\frac{1}{\tau} = S_w^{-1}(H - H_c) \tag{7.1}$$

with the layer-specific coercive field H_c and the switching coefficient $S_w \approx 2(1 + \alpha^2)/(\alpha \cdot \gamma)$ (DOYLE *et al.*, 1998). Although the quasistatically determined coercive fields cannot be considered valid at a nanosecond time scale due to an expected increase (MOORE *et al.*, 2005), the measured coercitivities of the two layers of $H_{c,\mathrm{CoFe}} \approx$

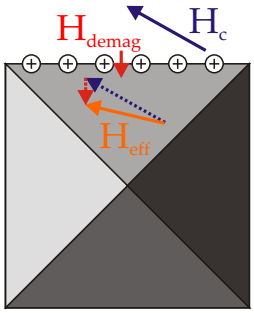

Figure 7.11: Construction of an effective field component acting on the NiFe magnetization.

5 mT and $H_{c,\mathrm{NiFe}} \approx 0.5$ mT can be regarded as a lower bound for the dynamic H_c values. Thus, from the comparison of these values the switching time τ in the CoFe layer is expected to be significantly higher than in the softer NiFe layer. However, due to the influence of the field profile and the incomplete switching this formula can here only be used for a qualitative interpretation rather than a detailed analysis of the switching behaviour.

During the relaxation of the magnetization between the two field pulses the magnetization of the two layers is tilted by an angle of $(7 \pm 2)^\circ$. For the interpretation of this dynamic breakdown of the interlayer coupling the single effective field contributions have to be considered. Following the argumentation of the previous paragraph, the dynamics of the CoFe layer can be assumed to be mainly determined by the high coercitivity and the NiFe magnetization aligns along the effective field direction. The acting field terms are the coupling field $H_c = J/(\mu_0 M_s t)$ and the demagnetizing field $\boldsymbol{H}_{\mathrm{demag}} = \mathbf{N}\boldsymbol{M}$. The coupling field is parallel to the CoFe magnetization and can be calculated as $\mu_0 H_c \approx 6.2$ mT, the inhomogeneous demagnetizing field is mainly induced by magnetic charges due to the rotation out of the orientation parallel to the element edges and is believed to be inwards oriented perpendicular to the edge and it is of the order of $\mu_0 H_{\mathrm{demag}} \approx 0.8$ mT. The comparison of these values shows that the NiFe magnetization is mostly influenced by the coupling field. However, the demagnetizing field favours an increased projection of the NiFe magnetization along the element edges. Considering a rotation of the CoFe magnetization of 30° relative to the element edge, as shown in fig. 7.11, the inplane components of the effective field acting on the NiFe magnetization is

$$\mu_0 \boldsymbol{H}_{\mathrm{eff}} = \mu_0 \begin{pmatrix} \cos(30^\circ) \cdot H_c \\ \sin(30^\circ) \cdot H_c - H_{\mathrm{demag}} \end{pmatrix} = \begin{pmatrix} 5.37 \\ 2.3 \end{pmatrix} \mathrm{mT}. \tag{7.2}$$

The effective field and the element edge include an angle of $\arctan(2.3/5.37) = 23.2^\circ$. Although derived from a simplified model without knowledge of the exact demagnetization field value the angle of 6.8° between NiFe and CoFe magnetization agrees resonably well with the experimental values.

The assumption of an independent behaviour in terms of a pseudo spin-valve fails

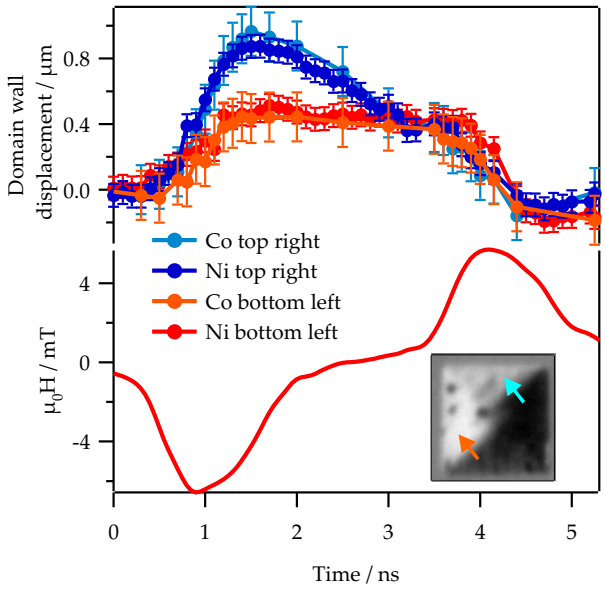

Figure 7.12: Bulging of the top right and bottom left domain walls (marked in inset). The error bars have been obtained from the standard deviation of the structure edges

when the coupling strength is enhanced by the increased stray fields near domain walls. Fig. 7.12 shows the measurements of the domain wall bulging observed in two domain wall in both layers. The measured domain wall positions in both layers agree well within their error bars. The two studied domain walls show a different behaviour with amplitudes of 400 nm (bottom left) and 800 nm. The different situation in both domain walls is attributed to inhomogeneities in the film growth leading to a different probability of a magnetization flip of the grains at both positions.

The maximum domain wall velocites that have been extracted from the data are 1000 m/s (top right) and 610 m/s (bottom left) and -270 m/s for the relaxation speed of the top right domain wall. Contrary to the results from the Fe film, these values are not limited by the Walker field. The Walker field of CoFe is $\mu_0 H_W \approx 18.8\,\mathrm{mT}$ (using $\alpha = 0.02$ and $\mu_0 M_S = 1.88\,\mathrm{T}$ from CHOE *et al.* (2004)) is distinctly higher than the maximum field value of 6.5 mT. Using literature values for the calculation of H_W for the NiFe layer ($\alpha = 0.01$, $\mu_0 M_S = 1.0\,\mathrm{T}$ yields a smaller value of $\mu_0 H_W = 5\,\mathrm{mT}$. However, measurements on shorter time scales, that will be presented in the next section, show an increased value of the NiFe damping coefficient $\alpha = 0.04$ resulting in $\mu_0 H_W = 20\,\mathrm{mT}$. Thus, in both layers the domain wall motion can be assumed to be in the viscous regime and therefore the domain wall displacement is directly driven by the external field.

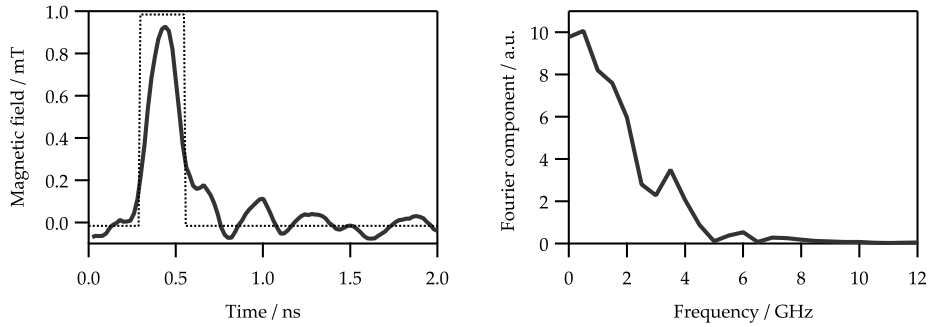

(a) Time-domain (b) Frequency-domain

Figure 7.13: Fast excitation pulse (a) and Fourier power spectrum (b). The edges of the 250 ps square wave (indicated by the dashed line in (a)) are smeared out due to imperfect impedance matching of the cabling. In the Fourier spectrum frequency components up to 5 GHz are visible.

7.3 Excitation of precessional eigenmodes

From previous experiments it is known that with sufficiently steep excitation signals eigenmodes of the magnetic system can be excited. With the time-resolved PEEM technique effects such as the excitation of modes of uniform precession (KRASYUK *et al.*, 2005; RAABE *et al.*, 2005), oscillations of the vortex core (CHOE *et al.*, 2004) and propagating and standing spin-waves (WEGELIN *et al.*, 2007) have been investigated. A necessary condition for the observation of such effects is the existence of frequency components in the excitation signal of the order of the eigenfrequency of the system. The frequency of the uniform mode of precession is given by the Kittel frequency (see eq. (2.33)) and lies typically in the GHz range for the type of microstructures studied in this thesis without considering an external field. As the Fourier transform of a Gaussian-shaped pulse with width σ_t has the width $\sigma_f = 1/\sigma_t$, the excitation of frequencies with more than 1 GHz by a Gaussian with $\sigma_t = 1$ ns is negligible. In order to study the influence of the interlayer coupling on the frequencies of the uniform mode experiments with shorter excitation signals have been carried out on a CoFe/Cr/NiFe trilayer with a wedged Cr spacer. The excitation signal was a square wave with a temporal width of 250 ps and a field amplitude of 1 mT. Ideal square signals have Fourier components up to infinite frequencies. However, the transmission spectrum of our experimental system has a cut-off at around 5 GHz, as displayed in fig. 7.13. The experiments have been conducted at BESSY-II (UE56/1-SGM) in the BESSY multi-bunch mode with a bunch repetition frequency of 500 MHz.

The magnetodynamics has been studied at different positions along the spacer wedge

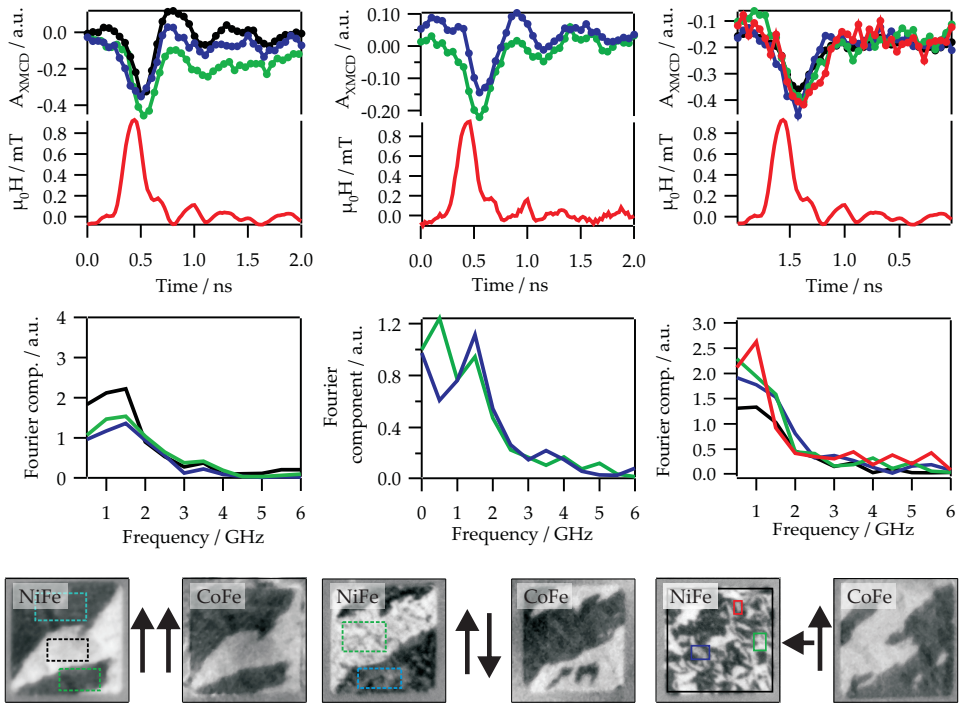

(a) Parallel configuration (b) Antiparallel configuration (c) Transition regime

Figure 7.14: Temporal profile of the response of the NiFe magnetization on the field pulse. The integration of the XMCD signal has been carried out over different integration areas as indicated in the bottom panel. All curves have been offset by the average XMCD value. The approximated error of the XMCD signal is $\Delta_{\mathrm{XMCD}} \approx 0.1$ due to beam instabilities. The Fourier transforms of all signals are compiled in the bottom panel showing different frequency components.

corresponding to a different coupling strength between CoFe and NiFe. In this sections measurements are shown that have been taken at a spacer thickness of 1.7 nm (parallel coupling), 2.0 nm (transition regime, partly 90° coupling) and 2.3 nm (antiparallel coupling). At all positions the system behaves as a pseudo spin-valve. The pulse field is not strong enough to rotate the bottom CoFe layer while the NiFe layer quickly follows the excitation field. The equilibrium position is given by the CoFe magnetization and the coupling field is exerting a restoring torque on the NiFe film.

In fig. 7.14 the measured signals of all three microstructures are compiled. In each case the XMCD signal has been integrated over boxes with maximum response. Within the error of the measurement configurations all measurement curves on one microstructure show an equal temporal behaviour. In the case of parallel and antiparallel magne-

tization configuration the signals have the shape of a damped sine due to a precession of the magnetization after the decay of the magnetic field pulse. In the reaction of the weakly coupled structure only the direct rotation by the field pulse is observed. The temporal width of the response is higher than the width of the field peak.

In all three cases the response peak is shifted by (100 ± 50) ps with respect to the field peak. For each measurement curve Fourier transforms have been carried out. The frequency components are shown in the bottom panels in fig. 7.14. Due to the strong precessional modes the data from both parallel and antiparallel coupled structures show peaks at $f = 1.5\,\mathrm{GHz}$, the weakly coupled structure shows a peak at $f = 1\,\mathrm{GHz}$ for one of the four signals. We account this peak an artefact in the measurements. However, it might be also attributed to a local excitation of a weak precessional mode with this frequency.

A comparison of the different measurements shows that the amplitudes of the antiparallel coupled element only reaches half of the values of the measurements on that exhibiting parallel coupling. A closer look on the magnetization reveals differences between the two structures. While the parallel coupled microstructure has rather large domains with only few deviations from the average magnetization, the antiparallel coupled element shows a ripple-like structure consisting of many small domains. Since the integration is carried out over many small domains, also domains with smaller rotation amplitudes are included leading to a reduction of the average rotation amplitude. In addition, the dipolar coupling of neighbouring grains is expected to block the magnetization from free rotation.

The precession of the magnetic moment can be explained on the basis of the Landau-Lifshitz-Gilbert (LLG) equation (eq. (2.32)). Under the influence of an effective magnetic field H_{eff} the magnetic moments precess around the effective field. The damping term of the LLG leads to a decrease of the precessional amplitude and a rotation towards the direction of H_{eff} with the time constant defined in eq. (2.34). Since our measurements are mostly sensitive to the projection of the magnetic moment on the field direction, the damping also explains the delay between rotation and peak. After the decay of the magnetic field pulse, it is the internal effective field that forces the magnetic moments back to their equilibrium position on a spiral trajectory. The internal components of the effective field are the anisotropy field H_{anis} which can be neglected in NiFe, the demagnetizing field $\boldsymbol{H}_{\mathrm{demag}} = \mathbf{N}\boldsymbol{M}$ and the coupling field $H_{\mathrm{coupl}} = J/(\mu_0 M_s \cdot t)$. Using the Kittel formula (2.33) the effective field H_{eff} can be derived from the precession frequency $f = \omega_0/2\pi$. From fits of a damped sine function to the measurement data frequencies of $f_{\mathrm{parallel}} = (1.62 \pm 0.14)$ GHz (parallel) and $f_{\mathrm{antiparallel}} = (1.7 \pm 0.1)$ GHz with damping times of $\tau_{\mathrm{parallel}} = (0.23 \pm 0.08)$ ns and $\tau_{\mathrm{antiparallel}} = (0.25 \pm 0.1)$ ns could be deduced. Using the above mentioned relations and the magnetization of NiFe of $\mu_0 M_s = 1\,\mathrm{T}$, the effective fields and damping

constants have been calculated as

$$\begin{aligned} \mu_0 H_{\text{eff, P}} &= (3.3 \pm 0.3)\ \text{mT} \\ \alpha_{\text{P}} &= 0.048 \pm 0.017 \\ \mu_0 H_{\text{eff, AP}} &= (3.4 \pm 0.2)\ \text{mT} \\ \alpha_{\text{AP}} &= 0.044 \pm 0.009. \end{aligned}$$

Neglecting the anisotropy field and subtracting the demagnetizing field of the order of $\mu_0 H_{\text{demag}} \approx 0.4\,\text{mT}$, a coupling field of $\mu_0 H \approx 3\,\text{mT}$ can be assumed, from which a coupling constant $J \approx 5 \cdot 10^{-6}\,\text{J/m}^2$ is obtained. This result is one order of magnitude smaller than the peak values extracted from the MOKE measurements in sect. 5.2. The deviation can be attributed to the fact, that the PEEM measurements have been carried out at random positions without considering the position of maximum coupling and are thus not comparable to the peak values. In addition, the coupling constant J that is derived from the frequency measurements is an effective value that depends on the bilinear and biquadratic coupling constants (KUANR *et al.*, 2003):

$$J_{\text{eff}} = J_1 + 2J_2 \quad \text{for parallel alignment} \tag{7.3}$$

$$J_{\text{eff}} = J_1 - 2J_2 \quad \text{for antiparallel alignment.} \tag{7.4}$$

Thus the measured value serves only as a raw estimate for the coupling constants J_1 and J_2. However, for dominating bilinear behaviour the real bilinear coupling constant is always higher than the effective value obtained from the frequency calculations. The obtained result of the damping constant of $\alpha > 0.04$ is distinctly higher than the literature value of $\alpha = 0.01$ (BONNENBERG *et al.*, 1986). Similarly increased values in thin NiFe layers in heterostructures have also been reported by other authors (GUAN, 2007; WEGELIN *et al.*, 2007; SCHUMACHER *et al.*, 2002) and may be attributed to a spin-pumping effect due to the interaction with the neighbouring non-magnetic films (TSERKOVNYAK *et al.*, 2002).

In order to compare the experimental results with theory the LLG was solved for a system of two coupled macrospins with the same dimensions as the two magnetic films of our experiment. For the calculation the LLG was written in terms of the polar and azimuthal angle ϕ and θ (MILTAT *et al.*, 2002):

$$\frac{\mathrm{d}\theta}{\mathrm{d}t} = -\frac{\gamma}{(1+\alpha^2)\mu_0 M_S}\left(\alpha\frac{\partial f}{\partial \theta} + \frac{1}{\sin\theta}\frac{\partial f}{\partial \phi}\right) \tag{7.5}$$

$$\frac{\mathrm{d}\phi}{\mathrm{d}t} = +\frac{\gamma}{(1+\alpha^2)\mu_0 M_S}\left(\frac{1}{\sin\theta}\frac{\partial f}{\partial \phi} - \frac{\alpha}{\sin^2\theta}\frac{\partial f}{\partial \theta}\right) \tag{7.6}$$

with the energy density f that is composed of the anisotropy, demagnetizing and coupling energy terms, as described in chapter 1. In order to reproduce the spin-valve behaviour the anisotropy constant of the bottom layer was set to $K_1 = 45000\,\text{J/m}^3$. Thus the magnetization of the bottom layer was only marginally influenced by the

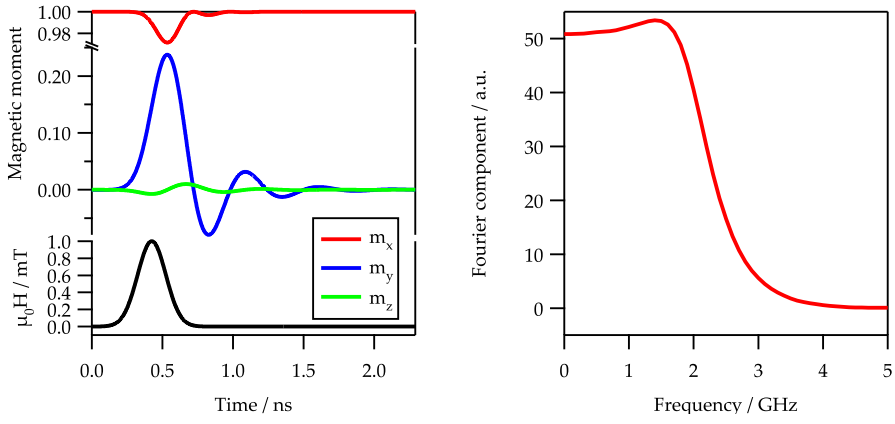

(a) Precession (b) Frequency components

Figure 7.15: Macro-spin simulation of a spin-valve system under the influence of a Gaussian-shaped field pulse. (a) Temporal behaviour of the free layer. (b) Fourier power spectrum of the m_y component.

weak magnetic field pulse of $\mu_0 H = 1\,\mathrm{mT}$ of Gaussian shape with a temporal width of 250 ps that is applied along the y-axis. Other values used in the simulation are $J_1 = 5 \cdot 10^{-6}\,\mathrm{J/m^2}$, $M_S = 800000\,\mathrm{A/m}$ and $\alpha = 0.04$. The resulting response of the three components of the magnetic moment and the Fourier transform of the m_y component are shown in fig. 7.15. All features of the experimental results for parallel and antiparallel coupling are reproduced by the simulation: The temporal and frequency characteristics of m_y resemble the experimental results. Furthermore the simulation reproduces the delay between maximum deflection of the m_y component and field peak. From the simulation a delay value of 120 ps is obtained which agrees well with the experimental value of (100 ± 50)ps. As expected the maximum m_z deflection coincides with the maximum of the external field and is transformed at a delay to an in-plane rotatioin.

7.4 Resonant excitation

Due to their broad frequency spectrum magnetic field pulses can excite a whole zoo of different oscillatory modes (ADAM *et al.*, 2007; PARK *et al.*, 2003). By using a continuous RF sine wave with a sharp frequency spectrum, the excitation can be limited to selected modes such as vortex motion, uniform magnetization precession or higher-order spin-wave modes. By temporal and spatially resolving imaging techniques such as PEEM or Kerr microscopy the spatial distribution of such oscillatory

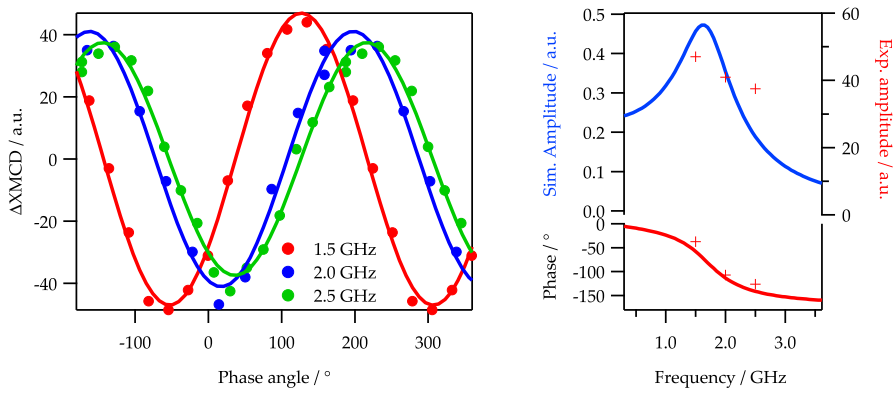

(a) Experiment (b) Simulation

Figure 7.16: (a) Phase-resolved XMCD signals acquired with excitation frequencies of 1.5 GHz, 2.0 GHz and 2.5 GHz together with a sine fit. The signals have been normalized to the excitation amplitude measured from the image shift. (b) Theoretical frequency dependence of oscillation amplitude and phase as acquired from a macrospin simulation. Experimental values are marked with crosses.

modes can be probed by applying an RF field on the sample that is frequency-matched with the illumination source. By some authors this technique has been referred to as *spatially resolved ferromagnetic resonance* (SR-FMR) (TAMARU *et al.*, 2002; PUZIC *et al.*, 2005). It has been applied to the investigation of vortex dynamics (BUESS *et al.*, 2003; PUZIC *et al.*, 2005) and surface spin waves (TAMARU *et al.*, 2002) by means of X-ray and Kerr microscopy. We have applied a similar approach to the investigation of magnetization precession using PEEM. Investigating the parallel coupled CoFe/Cr/NiFe structures discussed above, the experiments have been conducted by using a continuous sine wave excitation with variable frequency, which had to be an integer multiple of the bunch repetition frequency of 500 MHz.

Experimental results using excitation frequencies of 1.5 GHz, 2.0 GHz and 2.5 GHz are compiled in fig. 7.16(a). The displayed results have been obtained by integrating over a large domain with magnetization perpendicular to the magnetic field direction (black box in inset of fig. 7.14(a)). The coplanar waveguides and the cabling used in the experiment have a frequency-dependent transmission for frequencies in the GHz-range. Thus the magnetic field amplitudes have been measured from the shift and breathing of the images and the XMCD curves have been normalized to the real field amplitudes. The measured signals can be approximated by sine fits with different amplitude and phase values. The phase relative to the excitation signal is strongly frequency dependent while the normalized amplitude changes only slightly.

Macrospin simulations have been conducted assuming an RF excitation with variable

frequency and the resulting amplitude and phase values of the m_y rotation are displayed in fig. 7.16(b). The simulations predict a resonance at a frequency of 1.6 GHz connected with an increase of the oscillation amplitude and a phase shift of 180° over the width of the resonance ($\Delta f \approx 1\,\mathrm{GHz}$). The phase values that have been obtained from the experimental results show the same characteristics as the calculated values. However, the simulated behaviour of the amplitudes cannot be reproduced quantitatively. This deviation may be ascribed to the differences in the applied field strength and the difficulties in determining the real amplitudes.

7.5 Summary of the layer-resolved magnetization dynamics

Various aspects of magnetization dynamics in magnetically coupled heterostructures have been investigated in this chapter. In these experiments the full versatility of the XPEEM method exploiting spatial, elemental and temporal resolution was used. In most cases the dynamic response was influenced by a weak coupling with an independent reaction on the field pulse in both layers, in contrast to the situation in the equilibrium configuration. The major results are illustrated in fig. 7.17.

The behaviour of the Fe/Cr/Co trilayer (fig. 7.17 (a)) was determined by the anisotropy in the Fe layer suppressing magnetization rotation to a large degree, as known from the single film elements, and the high coercitivity of the Co layer. In the Co layer a competition between coupling field and external field appeared without a clear winner: The strong stray fields near Fe domain walls showed to influence the Co behaviour significantly, while in a large domain without considerable stray fields the Co magnetization was rotated by the pulse field.

In a CoFe/Cr/NiFe trilayer (fig. 7.17 (b)) incorporating parallel coupling the behaviour of a magnetically less anisotropic system could be studied. The system is characterized by a pseudo-spin-valve behaviour with significantly different coercive fields. This difference considerably influences the temporal characteristics of magnetization rotation towards the magnetic field pulse, significantly slowing down the process in the magnetically harder CoFe film. However, near domain walls this independent behaviour was found to break down probably due to the high stray fields at the domain boundaries. By decreasing the length of the excitation pulse, higher-frequency eigen-oscillations of the system have been excited. The NiFe magnetization of one domain was found to precess around an effective magnetic field that is mainly determined by the interlayer coupling strength. From the eigenfrequencies that were measured from the reaction the coupling constant of the system could be derived.

In addition, the feasibility of spatially resolved FMR measurements could be shown by applying a sinusoidal excitation signal of variable frequency. The phase shifts of the rotation relative to the excitation and amplitude of the magnetodynamic reactions

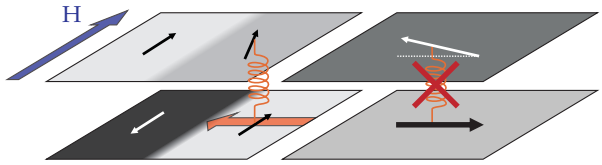

(a) Fe/Cr/Co

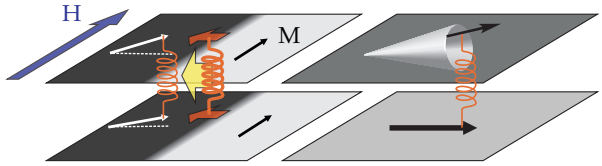

(b) CoFe/Cr/NiFe

Figure 7.17: Illustration of the different effects observed in trilayer systems. In Fe/Cr/Co (a) domain wall motion (red arrow) in the Fe layer yields a rotation of the Co layer due to interlayer coupling (indicated by springs) (left) and at a different position the Co layer is rotated towards the field direction independent of the fixed Fe magnetization (right). In CoFe/Cr/NiFe (b) strongly coupled domain wall motion (thick spring) and weaker coupled magnetization rotation (thin spring) was observed (left). Using low-amplitude excitation on a shorter time scale, the trilayer exhibits a spin-valve character with magnetization precession in the NiFe layer (right).

have been extracted from the measurements and compared to macrospin simulations showing a significant match of the determined phase relations. In future experiments using a broader spectrum of excitation frequencies this approach is expected to be able to systematically study the excitation of particular eigenmodes of magnetically coupled systems.

Chapter 8

Conclusions & Outlook

The topic of this thesis is the study of magnetization dynamics in magnetically coupled heterostructure systems. For the systematic analysis of the coupled behaviour and eventual limits of the coupling under the excitation with short magnetic field pulses, it was mandatory to carry out layer-resolved investigations in heterostructures. In order to discern the dynamics of different processes spatial resolution was needed. Therefore, the PEEM technique was chosen for the experiments incorporating spatial, elemental, magnetic and temporal resolution. During the work of this thesis the time-resolved PEEM technique was further developed and new insights into the physics of magnetization dynamics have been gained. In addition, novel experimental approaches have been tested with promising results for future experiments.

The technical improvements incorporate the implementation of the time-resolved method into the PEEM set-up that was used for the measurements. The technical modifications involved the development of a new sample-holder/sample-stage combination with high-frequency compatible cabling and adapters. For the time-resolved experiments an optical lithography mask was created for structuring coplanar waveguides and magnetic microstructures on the samples. Furthermore, by the development of the deflection gating technique the influence of unwanted light-pulses to the image generation could be suppressed. The deflection gating works on a timescale of 20 ns and thus enables the realization of time-resolved magnetic measurements with long relaxation times in the BESSY hybrid bunch mode. It was shown that the image quality was preserved by the gating.

In order to be able to interpret results of magnetodynamic measurements in terms of time- and coupling-independent sample properties preparatory experiments have been carried out illuminating the influence of coupling on the micromagnetic ground state configuration of various heterostructure systems and the effect of the magnetocrystalline anisotropy on the magnetodynamic response of single layers.

As a promising material for spintronics applications the micromagnetic structure of Heusler-based magnetic tunnelling junctions was investigated. The systems were found to be distinctly influenced by the different magnetic properties of the two magnetic materials, such as anisotropy and coercive field. The elemental selectivity of the XPEEM method revealed the disappearance of the Mn magnetic moment in a thin Co_2MnSi layer in one sample and a roughness-induced parallel interlayer coupling in another trilayer system. By PEEM measurements at elevated temperatures the influence of the Heusler phase formation on the micromagnetic structure was investigated. The combination of magnetic spectromicroscopy with temperature variation enables a microscopic view on the generation of magnetic ordering during the crystallization process and might be expanded to other systems in the future. Moreover, also the magnetodynamic properties of Heusler-based systems provide an interesting perspective for future experiments. As shown recently by KUBOTA *et al.* (2009) the half-metallic character of Heusler materials leads to a decrease of Gilbert damping in these systems, which has a decisive influence on the magnetodynamic behaviour.

Using MBE-grown heterostructures incorporating Chromium spacers the domain patterns of interlayer exchange coupled systems were investigated. Fe/Cr/Co and CoFe/Cr/NiFe trilayers have been studied as prototypes for systems with and without considerable influence of magnetocrystalline anisotropy, respectively. Both sample types showed the expected oscillatory dependence of the coupling behaviour on the spacer thickness. While in samples exhibiting strong bilinear coupling the magnetic configuration was unambiguously determined by the coupling conditions, in weaker coupled samples magnetostatic interactions were found to significantly influence the micromagnetics either by a local flux-closure in perpendicular coupled Fe/Cr/Co samples avoiding head-to-head/tail-to-head configurations or by the strong domain wall stray fields yielding a local enhancement of the coupling in a weakly coupled CoFe/Cr/NiFe sample.

The findings of the magnetodynamic measurements are compiled in fig. 8.1. They can be classified basically into two groups: Systems with a strong influence of the magnetocrystalline anisotropy and systems without a preferential in-plane orientation of the magnetization. Thus, as a first step towards the understanding of magnetodynamic reactions the effect of the magnetocrystalline anisotropy was studied in single layers, using the examples of the well-studied Permalloy and single-crystalline iron samples. The Permalloy results reproduced the findings of previous experiments and thus served as a successful test of the deflection gating technique. Compared to the low-anisotropic Permalloy the situation in the iron sample was drastically changed. The pinning of the magnetization along the four easy axes suppresses the free rotation of the magnetization yielding domain wall motion the only allowed channel for the dissipation of the Zeeman energy induced by the external magnetic field. However, due to the inhomogeneous demagnetizing field the domain walls in the magnetic elements can be assumed to be fixed at their end-points leading to a bulging of the domain walls. This effect has been observed before but was for the first time studied in more detail and compared to micromagnetic simulations.

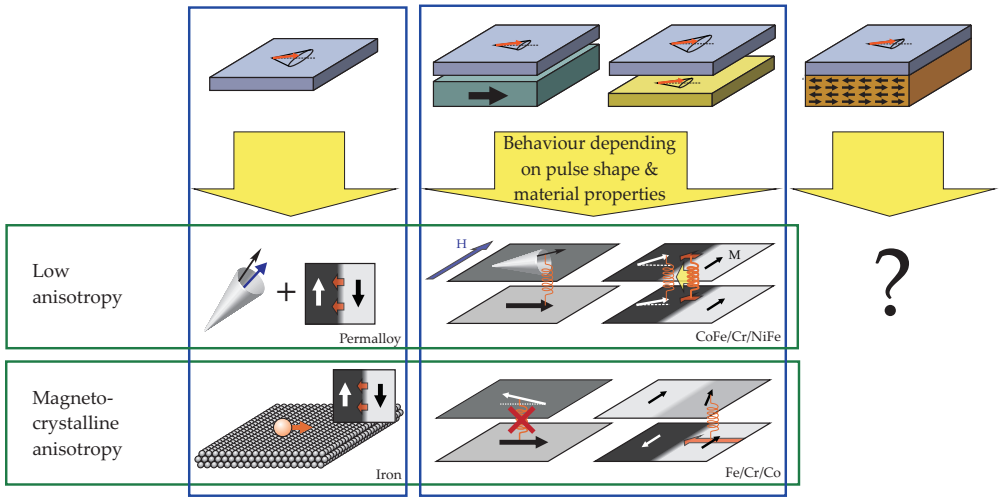

Figure 8.1: Illustration of the magnetodynamic processes investigated in the different magnetic systems: Single and multi-layers with and without considerable magnetocrystalline anisotropy. In epitaxial single layers the presence of magnetocrystalline anisotropy led to the suppression of a sizeable magnetization rotation. A similar behaviour was also observed in the magnetic heterostructures yielding domain wall motion the dominant process in magnetically anisotropy Fe/Cr/Co trilayers. Moreover, the results acquired for the magnetically coupled heterostructures revealed both behaviour of a spin-valve and of a system of coupled magnetic layers with individual reactions. The magnetodynamics of ferromagnet-antiferromagnet bilayers is still an open topic for future experiments.

With the knowledge of the energy terms determining the static structure and the understanding of the influence of internal fields on the magnetodynamic reaction, different heterostructure systems have been investigated with the time-resolved PEEM set-up. Although the equilibrium domain structure was determined by the coupling of the magnetic layers, the dynamic situation was found to be strongly influenced by their intrinsic properties. As a trilayer with pronounced magnetocrystalline anisotropy the Fe/Cr/Co system was investigated. Due to the antiparallel coupling this system was ideally suited for studies of the competition between magnetic field and coupling. Because of the high coercitivity of the Co layer the magnetodynamic reaction was mostly limited to domain wall motion in the Fe layer. However, the reaction was also influenced by the interlayer coupling: Defects in the Co layer were supposed to facilitate the growth of stripe domains in the Fe layer, that in turn led to a slight magnetization rotation in the Co layer that can be clearly attributed to a coupling effect. At other sample positions in the Co layer magnetization rotations both towards and opposite to the magnetic field direction could be observed that have been interpreted in terms of inhomogeneous magnetic stray fields.

In CoFe/Cr/NiFe the magnetodynamic response of a system mostly determined by the shape rather than the magnetocrystalline anisotropy could be studied. Here magnetization rotation and domain wall motion effects were investigated. Due to the high coercitivity the speed of magnetization rotation in CoFe was reduced compared to the soft-magnetic NiFe layer. The deviations could be interpreted by a simple model considering the effective magnetic field acting on the NiFe layer. The analysis of the domain wall motion revealed a different behaviour: Again, the stray fields at the domain boundaries led to a locally stronger coupling inducing a parallel motion of the domain walls in both layers.

By lowering the timescale of the excitation pulse by one order of magnitude, precessional magnetization rotation rather than a driven behaviour could be excited. At different positions of a CoFe/Cr/NiFe trilayer with a wedged interlayer, the precessional frequencies of the NiFe magnetization were studied. The results could be reproduced by a macrospin simulation model and were found to be significantly influenced by the interlayer coupling to the CoFe layer.

With these experiments the magnetodynamic reactions of magnetically coupled heterostructures were investigated observing a spatially inhomogeneous response. Here the spatial resolution of the PEEM method proved a striking advantage over spatially integrating XMCD methods since the dynamic reaction could be studied on a sub-µm length scale where local variations of the coupling were found due to the inhomogeneous effective field terms. For the first time, microscopic studies have been carried out on coupled systems showing an individual magnetodynamic response in both layers. The local magnetodynamic behaviour was found to be influenced by the excitation pulse shape and amplitude, by the intrinsic material properties of the single layers and by locally varying effective field terms giving rise to inhomogeneities in the effective coupling strength.

In addition to these scientific insights, first steps have been made towards new experimental methods. For the first time the standing wave/wedge method, based on the modulation of the photo-electron yield by standing wave generation, was employed in a microscope. First experiments resulted in promising results and in future experiments combining depth- and time-resolution this method might enable the microscopic investigation of interface magnetodynamics. Furthermore, we have employed continuous wave excitation signals in the time-resolved measurements allowing for the systematic studies of the resonance phenomena by driving the excitation frequency. Such spatially resolved ferromagnetic resonance (SR-FMR) experiments have already been conducted using other microscopy methods. By implementing this method into a PEEM the way is paved for the systematic layer-resolved study of the influence of interlayer coupling on magnetodynamic eigenmodes. The first experiments have been carried out under regular conditions in the BESSY hybrid bunch for which reason the excitation frequencies have been limited to multiple integers of the multi bunch repetition frequency of 500 MHz. In combination with the deflection gating technique, however, this limitation can be overcome in future experiments

enabling studies at multiple integers of the single bunch frequency of 1.25 MHz, considerably increasing the degree of freedom in the choice of the excitation frequency.

An interesting topic for future experiments is the study of ferromagnet-antiferromagnet (FM-AFM) bilayers, as indicated on the right hand side of fig. 8.1. The exchange coupling occurring at such interfaces accessible by XMCD and XMLD is an important application area of soft x-ray photoemission microscopy. In a recent work KRUG (2008) has incorporated the model of anisotropic XMLD in the analysis of the coupling at the Fe_3O_4/NiO interface allowing for the quantitative analysis of the spin orientation. Combined with the interface-sensitivity provided by the standing wave method, the understanding of the coupling near FM-AFM interfaces might be drastically improved. Moreover, the magnetization dynamics of FM-AFM thin film systems is an interesting field of research, as shown in recent works by MCCORD (2009). Regarding the inhomogeneous exchange bias investigated microscopically by KRONAST *et al.* (2008b), the influence of a spatially varying coupling strength on the magnetization dynamics can be further investigated by future time-resolved PEEM measurements.

One limiting factor of the study of magnetization dynamics by time-resolved PEEM is given by the limitation of the temporal resolution to the width of the light pulses of ca. 30 ps. This limitation can be overcome at the expense of intensity by using the low-alpha mode provided at BESSY-II with a light pulse width of 1-2 ps (BESSY WEBSITE, 2009). The study of faster magnetic processes has been demonstrated in this mode by experiments carried out by WEGELIN *et al.* (2007) observing the excitation of spin wave modes. Faster processes such as the ultrafast demagnetization by a laser pulse (BEAUREPAIRE *et al.*, 1996) or all-optical magnetization switching reported by STANCIU *et al.* (2007) are currently not accessible by time-resolved PEEM methods. Promising results of NAKAGAWA *et al.* (2007) and HILD *et al.* (2008, 2009) report of the observation of XMCD in laser-based photoemission, raising hope for the study of ultrafast magnetodynamic processes by time-resolved PEEM experiments using lab-based light sources in the near future.

Bibliography

ADAM, R., KHIVINTSEV, Y., HERTEL, R., SCHNEIDER, C. M., HUTCHISON, A., CAMLEY, R., & CELINSKI, Z., *Dynamic properties of arrays of ferromagnetic rectangular bars*, J. Appl. Phys. **101**, 09F516 (2007).

AHARONI, A., *Demagnetizing factors for rectangular ferromagnetic prisms*, J. Appl. Phys. **83**, 3432 (1998).

ATTWOOD, D., *Soft x-rays and extreme ultraviolet radiation: principles and applications* (Cambridge University Press, 2007).

BAIBICH, M. N., BROTO, J. M., FERT, A., NGUYEN VAN DAU, F., PETROFF, F., ETIENNE, P., CREUZET, G., FRIEDERICH, A., & CHAZELAS, J., *Giant magnetoresistance of (001)Fe/(001)Cr magnetic superlattices*, Phys. Rev. Lett. **61**, 2472 (1988).

BALL, P., *The hidden Van Gogh*, Nature **454**, 563 (2008).

BALTZ, A. & DOYLE, W. D., *Effect of Crystallite Size and Orientation on the Magnetization Ripple in Permalloy Films*, J. Appl. Phys. **35**, 1814 (1964).

BAUER, E., *Photoelectron spectromicroscopy: present and future*, J. El. Spectr. and Rel. Phen. **114**, 975 (2001).

BAUER, M., WIEMANN, C., LANGE, J., BAYER, D., ROHMER, M., & AESCHLIMANN, M., *Phase propagation of localized surface plasmons probed by time-resolved photoemission electron microscopy*, Appl. Phys. A **88**, 473 (2007).

BEAUREPAIRE, E., MERLE, J. C., DAUNOIS, A., & BIGOT, J. Y., *Ultrafast spin dynamics in ferromagnetic nickel*, Phys. Rev. Lett. **76**, 4250 (1996).

BERGER, A., *Technology of Hard Disk Drives*, *in:* S. BLÜGEL, D. BÜRGLER, M. MORGENSTERN, C. M. SCHNEIDER, & R. WASER (eds.), *Spintronics, 40th IFF Spring School* (Forschungszentrum Jülich, 2009).

BERGMANN, L., SCHÄFER, C., KASSING, R., & BLÜGEL, S., *Lehrbuch der Experimentalphysik: Festkörper* (de Gruyter, 2005).

BERNHARD, P., MAUL, J., BERG, T., WEGELIN, F., OTT, U., SUDEK, C., SPIECKER, H., MERCHEL, S., & SCHÖNHENSE, G., *Nondestructive full-field imaging XANES-PEEM analysis of cosmic grains*, Phys. Rev. B **74**, 75401 (2006).

BESSY WEBSITE, *BESSY Operating modes* (2009), URL `http://www.helmholtz-berlin.de/forschung/grossgeraete/betrieb-beschleuniger/betriebsmodi_en.html`.

BIHLMAYER, G., *Reduced Dimension II: Magnetic Anisotropy*, *in:* S. BLÜGEL, T. BRÜCKEL, & C. M. SCHNEIDER (eds.), *Magnetism Goes Nano, 36th IFF Spring School* (Forschungszentrum Jülich, 2005).

BINASCH, G., GRÜNBERG, P., SAURENBACH, F., & ZINN, W., *Enhanced magnetoresistance in layered magnetic structures with antiferromagnetic interlayer exchange*, Phys. Rev. B **39**, 4828 (1989).

BIRAGNET, F., DEVENYI, J., CLERC, G., MASSENET, O., MONTMORY, R., & YELON, A., *Interactions between domain walls in coupled films*, phys. stat. sol. (b) **16**, 569 (1966).

BLAND, A. & HEINRICH, B., *Ultrathin magnetic structures* (Springer, 2005).

BLÜGEL, S., *Magnetische Anisotropie und Magnetostriktion (Theorie)*, *in:* R. HÖLZLE (ed.), *30. IFF-Ferienkurs, Magnetische Schichtsysteme* (Forschungszentrum Jülich, 1999).

BLUNDELL, S., *Magnetism in Condensed Matter* (Oxford University Press, 2001).

BOBO, J. F., KIKUCHI, H., REDON, O., SNOECK, E., PIECUCH, M., & WHITE, R. L., *Pinholes in antiferromagnetically coupled multilayers: Effects on hysteresis loops and relation to biquadratic exchange*, Phys. Rev. B **60**, 4131 (1999).

BONFIM, M., GHIRINGHELLI, G., MONTAIGNE, F., PIZZINI, S., BROOKES, N. B., PETROFF, F., VOGEL, J., CAMARERO, J., & FONTAINE, A., *Element-Selective Nanosecond Magnetization Dynamics in Magnetic Heterostructures*, Phys. Rev. Lett. **86**, 3646 (2001).

BONNENBERG, D., HEMPEL, K. A., & WIJN, H. P. J., *Magnetic properties: Alloys between 3d elements: Alloys between Fe, Co or Ni*, *in: Landolt-Börnstein III/32A* (Springer, 1986).

BÜRGLER, D. E., GRÜNBERG, P., DEMOKRITOV, S. O., & JOHNSON, M. T., *Interlayer exchange coupling in layered magnetic structures*, *in:* K. H. J. BUSCHOWS (ed.), *Handbook of Magnetic Materials, Vol. 13* (Elsevier, 2001).

BRÜCHE, E., *Elektronenmikroskopische Abbildung mit lichtelektrischen Elektronen*, Z. Phys. A Hadr. and Nuclei **86**, 448 (1933).

BRÜCHE, E. & JOHANNSON, H., *Elektronenoptik und Elektronenmikroskop*, Die Naturwissenschaften **20**, 353 (1932).

BRUNO, P., *Physical origins and theoretical models of magnetic anisotropy, in:* R. HÖLZLE (ed.), *24. IFF-Ferienkurs, Magnetismus von Festkörpern und Grenzflächen* (Forschungszentrum Jülich, 1993).

BUCHMEIER, M., *private communication* (2009).

BUESS, M., HÖLLINGER, R., HAUG, T., PERZLMAIER, K., KREY, U., PESCIA, D., SCHEINFEIN, M. R., WEISS, D., & BACK, C. H., *Fourier transform imaging of spin vortex eigenmodes*, Phys. Rev. Lett. **93**, 077207 (2003).

BÜRGLER, D. E. & GRÜNBERG, P. A., *Magnetoelectronics - Magnetism and Magnetotransport in Layered Structures, in:* R. WASER (ed.), *Nanoelectronics and Information Technology* (Wiley-Vch, 2005).

BÜRGLER, D. E., SCHMIDT, C. M., SCHALLER, D. M., MEISINGER, F., HOFER, R., & GÜNTHERODT, H.-J., *Optimized epitaxial growth of Fe on Ag(001)*, Phys. Rev. B **56**, 4149 (1997).

CAMARA, C. G., ESCOBAR, J. V., HIRD, J. R., & PUTTERMAN, S. J., *Correlation between nanosecond X-ray flashes and stick-slip friction in peeling tape*, Nature **455**, 1089 (2008).

CARRA, P., THOLE, B. T., ALTARELLI, M., & WANG, X., *X-ray circular dichroism and local magnetic fields*, Phys. Rev. Lett. **70**, 694 (1993).

CHOE, S. B., ACREMANN, Y., SCHOLL, A., BAUER, A., DORAN, A., STOHR, J., & PADMORE, H. A., *Vortex Core-Driven Magnetization Dynamics*, Science **304**, 420 (2004).

CHOU, K., PUZIC, A., STOLL, H., SCHÜTZ, G., VAN WAEYENBERGE, B., TYLISZCZAK, T., ROTT, K., REISS, G., BRÜCKL, H., NEUDECKER, I., *et al.*, *Vortex dynamics in coupled ferromagnetic multilayer structures*, J. Appl. Phys. **99**, 08F305 (2006).

CHUMAKOV, D., MCCORD, J., SCHÄFER, R., SCHULTZ, L., VINZELBERG, H., KALTOFEN, R., & MÖNCH, I., *Nanosecond time-scale switching of permalloy thin film elements studied by wide-field time-resolved Kerr microscopy*, Phys. Rev. B **71**, 014410 (2005).

CONGER, R. L. & TOMLINSON, J. L., *Magneto-optic readout for computer memories*, J. Appl. Phys. **33**, 1059 (1962).

CRAMM, S., *Synchrotron Radiation Sources and Beamlines: Overview, in:* K. URBAN, C. M. SCHNEIDER, T. BRÜCKEL, S. BLÜGEL, K. TILLMANN, W. SCHWEIKA, M. LENTZEN, & L. BAUMGARTEN (eds.), *Probing the Nanoworld, 38th IFF Spring School* (Forschungszentrum Jülich, 2007).

DE GROOT, R. A., MUELLER, F. M., ENGEN, P. G., & BUSCHOW, K. H. J., *New Class of Materials: Half-Metallic Ferromagnets*, Phys. Rev. Lett. **50**, 2024 (1983).

DEMOKRITOV, S., TSYMBAL, E., GRÜNBERG, P., ZINN, W., & SCHULLER, I. K., *Magnetic-dipole mechanism for biquadratic interlayer coupling*, Phys. Rev. B **49**, 720 (1994).

DEMOKRITOV, S. O., *Biquadratic interlayer coupling in layered magnetic systems*, J. Phys. D. Appl. Phys. **31**, 925 (1998).

DIN, *DIN EN 122340:2002, Rahmenspezifikation - Hochfrequenz-Steckverbinder - Serie MMCX* (Deutsches Institut für Normung, 2002).

DONAHUE, M. J. & PORTER, D. G., *OOMMF User's Guide, Interagency Report NISTIR 6376* (National Institute of Standards and Technology, 1999).

DOYLE, W. D., STINNETT, S., DAWSON, C., & HE, L., *Magnetization Reversal at High Speed: An Old Problem in a New Context*, J. Magn. Soc. Jap. **22**, 91 (1998).

EIMÜLLER, T., SCHOLL, A., LUDESCHER, B., SCHÜTZ, G., & THIELE, J. U., *Slow relaxation of spin reorientation following ultrafast optical excitation*, Appl. Phys. Lett. **91**, 042508 (2007).

EINSTEIN, A., *Über einen die Erzeugung und Verwandlung des Lichtes betreffenden heuristischen Gesichtspunkt*, Ann. Phys. **17**, 132 (1905).

ELSPEC GMBH, *Subminiaturkabel MK5001* (2007).

ESCHER, M., WEBER, N., MERKEL, M., KRÖMKER, B., FUNNEMANN, D., SCHMIDT, S., REINERT, F., FORSTER, F., HÜFNER, S., BERNHARD, P., ZIETHEN, C., ELMERS, H. J., & SCHÖNHENSE, G., *NanoESCA: imaging UPS and XPS with high energy resolution*, J. El. Spect. Rel. Phen. **144**, 1179 (2005).

FERRÉ, J., *Dynamics of Magnetization Reversal: From Continuous to Patterned Ferromagnetic Films, in:* B. HILLEBRANDS & K. OUNADJELA (eds.), *Spin dynamics in confined magnetic structures, Vol. 1* (Springer, 2002).

FINK, R., WEISS, M. R., UMBACH, E., PREIKSZAS, D., ROSE, H., SPEHR, R., HARTEL, P., ENGEL, W., DEGENHARDT, R., WICHTENDAHL, R., KUHLENBECK, H., ERLEBACH, W., IHMANN, K., SCHLÖGL, R., FREUND, H.-J., BRADSHAW, A. M., LILIENKAMP, G., SCHMIDT, T., BAUER, E., & BENNER, G., *SMART: a planned ultrahigh-resolution spectromicroscope for BESSY II*, J. El. Spect. Rel. Phen. **84**, 231 (1997).

FLIESSBACH, T., *Elektrodynamik* (BI Wissenschaftsverlag, 1994).

FOCUS GMBH, *FOCUS IS-PEEM Manual* (2001).

FRAZER, B. H., GILBERT, B., SONDEREGGER, B. R., & DE STASIO, G., *The probing depth of total electron yield in the sub-keV range: TEY-XAS and X-PEEM*, Surf. Sc. **537**, 161 (2003).

FUKUMOTO, K., KUCH, W., VOGEL, J., ROMANENS, F., PIZZINI, S., CAMARERO, J., BONFIM, M., & KIRSCHNER, J., *Dynamics of Magnetic Domain Wall Motion after Nucleation: Dependence on the Wall Energy*, Phys. Rev. Lett. **96**, 97204 (2006).

GALANAKIS, I., DEDERICHS, P. H., & PAPANIKOLAOU, N., *Slater-Pauling behavior and origin of the half-metallicity of the full-Heusler alloys*, Phys. Rev. B **66**, 174429 (2002).

GALLAGHER, W. J. & PARKIN, S. S. P., *Development of the magnetic tunnel junction MRAM at IBM: From first junctions to a 16-Mb MRAM demonstrator chip*, IBM J. Res. Dev. **50**, 5 (2006).

GILBERT, T. L., *A phenomenological theory of damping in ferromagnetic materials*, IEEE Trans. Mag. **40**, 3443 (2004).

GRIEBEL, M., *Ultraschnelle Ladungsträgerdynamik in LTG-GaAs und ErAs:GaAs-Ubergittern – Grundlagen und Anwendungen*, Ph.D. thesis, Universität Stuttgart (2002).

GRÜNBERG, P., SCHREIBER, R., PANG, Y., BRODSKY, M. B., & SOWERS, H., *Layered Magnetic Structures: Evidence for Antiferromagnetic Coupling of Fe Layers across Cr Interlayers*, Phys. Rev. Lett. **57**, 2442 (1986).

GUAN, Y., *Ultrafast magnetization dynamics in ferromagnetic thin films and heterostructures*, Ph.D. thesis, Columbia University (2007).

GULLIKSON, E., *Calculator for multilayer reflectivity* (2008), URL `http://henke.lbl.gov/optical_constants/multi2.html`.

HAYASHI, K., SHIN'ICHI KAWATO, T. H., MATSUSHIGE, K., KITAJIMA, Y., TAKENAKA, H., & KAWAI, J., *Photoelectron spectra enhanced by x-ray total reflection and diffraction from periodic multilayer*, Appl. Phys. Lett. **68**, 1921 (1996).

HEINRICH, B., *Spin Relaxation in Magnetic Metallic Layers and Multilayers*, *in:* B. HEINRICH & J. A. C. BLAND (eds.), *Ultrathin Magnetic Structures III* (Springer, 2004).

HEINRICH, B. & COCHRAN, J. F., *Ultrathin metallic magnetic films: magnetic anisotropies and exchange interactions*, Adv. Phys. **42**, 523 (1993).

HERTEL, R., *Micromagnetism*, *in:* S. BLÜGEL, D. BÜRGLER, M. MORGENSTERN, C. M. SCHNEIDER, & R. WASER (eds.), *Spintronics, 40th IFF Spring School* (Forschungszentrum Jülich, 2009).

HEUSLER, F., *Über magnetische Manganlegierungen*, Verh. Dtsch. Phys. Ges. **12**, 219 (1903).

HIEBERT, W. K., STANKIEWICZ, A., & FREEMAN, M. R., *Direct observation of magnetic relaxation in a small permalloy disk by time-resolved scanning Kerr microscopy*, Phys. Rev. Lett. **79**, 1134 (1997).

HILD, K., MAUL, J., MENG, T., KALLMAYER, M., SCHÖNHENSE, G., ELMERS, H. J., RAMOS, R., ARORA, S. K., & SHVETS, I. V., *Optical magnetic circular dichroism in threshold photoemission from a magnetite thin film*, J. Phys. Cond. Matt. **20**, 235218 (2008).

HILD, K., MAUL, J., SCHÖNHENSE, G., ELMERS, H. J., AMFT, M., & OPPENEER, P. M., *Magnetic Circular Dichroism in Two-Photon Photoemission*, Phys. Rev. Lett. **102**, 057207 (2009).

HOFFMANN, H., *Theory of magnetization ripple*, IEEE Trans. Magn. **4**, 32 (1968).

HUBER JR., E. E., SMITH, D. O., & GOODENOUGH, J. B., *Domain-Wall Structure in Permalloy Films*, J. Appl. Phys. **29**, 294 (1958).

HUBERT, A. & RÜHRIG, M., *Micromagnetic analysis of thin-film elements (invited)*, J. Appl. Phys. **69**, 6072 (1991).

HUBERT, A. & SCHÄFER, R., *Magnetic Domains: The Analysis of Magnetic Microstructures* (Springer, 1998).

IVANOV, B. A. & ZASPEL, C. E., *Gyrotropic mode frequency of vortex-state permalloy disks*, J. Appl. Phys. **95**, 7444 (2004).

JACKSON, J. D., *Classical Electrodynamics* (Wiley, 1998).

JAKUBITH, S., ROTERMUND, H. H., ENGEL, W., VON OERTZEN, A., & ERTL, G., *Spatiotemporal concentration patterns in a surface reaction: Propagating and standing waves, rotating spirals, and turbulence*, Phys. Rev. Lett. **65**, 3013 (1990).

JANSEN, R., *The spin-valve transistor: a review and outlook*, J. Phys. D **36**, 289 (2003).

JULLIERE, M., *Tunneling between ferromagnetic films*, Phys. Lett. A **54**, 225 (1975).

KAISER, A., BANERJEE, D., RATA, A. D., WIEMANN, C., CRAMM, S., & SCHNEIDER, C. M., *Magnetic microstructure of candidates for epitaxial dual Heusler magnetic tunnel junctions*, J. Magn. Magn. Mat. **321**, 1182 (2009a).

KAISER, A., WIEMANN, C., CRAMM, S., & SCHNEIDER, C. M., *Influence of Magnetocrystalline Anisotropy on the Magnetization Dynamics of Magnetic Microstructures*, J. Phys. Cond. Matt. (accepted) (2009b).

KITTEL, C., *On the Theory of Ferromagnetic Resonance Absorption*, Phys. Rev. **73**, 155 (1948).

KÄMMERER, S., *The Heusler alloy Co_2MnSi in thin films*, Ph.D. thesis, Univ. Bielefeld (2003).

KOSCIESZA, D. & BARTUNIK, H. D., *Extraction of single bunches of synchrotron radiation from storage rings with an X-ray chopper based on a rotating mirror*, J. Synchrotron Rad. **6**, 947 (1999).

KOTSUGI, M., KUCH, W., OFFI, F., CHELARU, L. I., & KIRSCHNER, J., *Microspectroscopic two-dimensional Fermi surface mapping using a photoelectron emission microscope*, Rev. Sc. Instr. **74**, 2754 (2003).

KRASYUK, A., *Entwicklung der zeitaufgelösten Photoemissions-Elektronenmikroskopie für die Untersuchung der Magnetisierungsdynamik von mikrostrukturierten magnetischen Schichten*, Ph.D. thesis, Johannes Gutenberg-Universität Mainz (2006).

KRASYUK, A., OELSNER, A., NEPIJKO, S., KUKSOV, A., SCHNEIDER, C., & SCHÖNHENSE, G., *Time-resolved photoemission electron microscopy of magnetic field and magnetisation changes*, Applied Physics A: Materials Science & Processing **76**, 863 (2003).

KRASYUK, A., WEGELIN, F., NEPIJKO, S., ELMERS, H., SCHÖNHENSE, G., BOLTE, M., & SCHNEIDER, C., *Self-Trapping of Magnetic Oscillation Modes in Landau Flux-Closure Structures*, Phys. Rev. Lett. **95**, 207201 (2005).

KRÖMKER, B., ESCHER, M., FUNNEMANN, D., HARTUNG, D., ENGELHARD, H., & KIRSCHNER, J., *Development of a momentum microscope for time resolved band structure imaging*, Rev. Sc. Instr. **79**, 053702 (2008).

KRONAST, F., OVSYANNIKOV, R., KAISER, A., WIEMANN, C., YANG, S.-H., LOCATELLI, A., BÜRGLER, D. E., SCHREIBER, R., SALMASSI, F., FISCHER, P., DÜRR, H. A., SCHNEIDER, C. M., EBERHARDT, W., & FADLEY, C. S., *Depth-resolved soft x-ray photoelectron emission microscopy in nanostructures via standing-wave excited photoemission*, Appl. Phys. Lett. **93**, 243116 (2008a).

KRONAST, F., SCHLICHTING, J., RZHEVSKIY, A., RADU, F., SHRAWAN, M., DÜRR, H. A., & EBERHARDT, W., *Imaging of exchange bias in Co/FeMn bilayers on the nm length scale, in: LEEM/PEEM VI*, p. 38 (2008b).

KRONMÜLLER, H. & FÄHNLE, M., *Micromagnetism and the microstructure of ferromagnetic solids* (Cambridge University Press, 2003).

KRUG, I. P., *Magnetic Proximity Effects in Highly-Ordered Transition Metal Oxide Heterosystems – A Study by Soft-X-Ray Photoemission Microscopy*, Ph.D. thesis, Universität Duisburg-Essen (2008).

KRYDER, M. H. & HUMPHREY, F. B., *Dynamic Kerr Observations of High Speed Flux Reversal and Relaxation Processes in Permalloy Thin Films*, J. Appl. Phys. **40**, 1225 (1969).

KUANR, B. K., BUCHMEIER, M., GAREEV, R. R., BÜRGLER, D. E., SCHREIBER, R., & GRÜNBERG, P., *Spin-wave modes and line broadening in strongly coupled epitaxial Fe/Al/Fe and Fe/Si/Fe trilayers observed by Brillouin light scattering*, J. Appl. Phys. **93**, 3427 (2003).

KUBOTA, T., TSUNEGI, S., OOGANE, M., MIZUKAMI, S., MIYAZAKI, T., NAGANUMA, H., & ANDO, Y., *Half-metallicity and Gilbert damping constant in CoFeMnSi Heusler alloys depending on the film composition*, Appl. Phys. Lett. **94**, 122504 (2009).

KUCH, W., FROEMTER, R., GILLES, J., HARTMANN, D., ZIETHEN, C., SCHNEIDER, C. M., SCHÖNHENSE, G., SWIECH, W., & KIRSCHNER, J., *Element-Selective Magnetic Imaging in Exchange-Coupled Systems by Magnetic Photoemission Microscopy*, Surf. Rev. Lett. **5**, 1241 (1998).

KÜPFMÜLLER, K., MATHIS, W., & REIBIGER, A., *Theoretische Elektrotechnik* (Springer, 2005).

LANDAU, L. D. & LIFSHITZ, E., *On the theory of the dispersion of magnetic permeability in ferromagnetic bodies*, Phys. Z. Sowjetunion **8**, 101 (1935).

LEE, W. Y., CHOI, B. C., XU, Y. B., & BLAND, J. A. C., *Magnetization reversal dynamics in epitaxial Fe/GaAs (001) thin films*, Phys. Rev. B **60**, 10216 (1999).

MCCORD, J., *Magnetization Dynamics of Coupled Ferromagnetic-Antiferromagnetic Thin Films*, Advances in Solid State Physics **48**, 157 (2009).

MCMICHAEL, R. D. & STILES, M. D., *Magnetic normal modes of nanoelements*, J. Appl. Phys. **97** (2005).

MCPHERSON, A., LEE, W. K., & MILLS, D. M., *A synchronized rotating crystal x-ray beam chopper*, Rev. Sc. Instr. **73**, 2852 (2002).

MEIKLEJOHN, W. & BEAN, C., *New magnetic anisotropy*, Phys. Rev. **102**, 1413 (1956).

MERKEL, M., ESCHER, M., SETTEMEYER, J., FUNNEMANN, D., OELSNER, A., ZIETHEN, C., SCHMIDT, O., KLAIS, M., & SCHONHENSE, G., *Microspectroscopy and spectromicroscopy with photoemission electron microscopy using a new kind of imaging energy filter*, Surf. Sc. **480**, 196 (2001).

MEYER ZU HERINGDORF, F. J., CHELARU, L. I., MÖLLENBECK, S., THIEN, D., & HORN-VON HOEGEN, M., *Femtosecond photoemission microscopy*, Surface Science **601**, 4700 (2007).

MILTAT, J., ALBUQUERQUE, G., & THIAVILLE, A., *An introduction to micromagnetics in the dynamic regime, in:* B. HILLEBRANDS & K. OUNADJELA (eds.), *Spin dynamics in confined magnetic structures, Vol. 1* (Springer, 2002).

MOODERA, J. S., KINDER, L. R., WONG, T. M., & MESERVEY, R., *Large Magnetoresistance at Room Temperature in Ferromagnetic Thin Film Tunnel Junctions*, Phys. Rev. Lett. **74**, 3273 (1995).

MOORE, T. A., WALKER, M. J., MIDDLETON, A. S., & BLAND, J. A. C., *Mesofrequency switching dynamics in epitaxial CoFe and Fe thin films on GaAs (001)*, J. Appl. Phys. **97**, 053903 (2005).

NAKAGAWA, T., YOKOYAMA, T., HOSAKA, M., & KATOH, M., *Measurements of threshold photoemission magnetic dichroism using ultraviolet lasers and a photoelastic modulator*, Rev. Sc. Instr. **78**, 023907 (2007).

NÉEL, L., *Sur un nouveau mode de couplage entre les aimantation de deux couches minces ferromagnétiques*, C. R. Acad. Sci. **255**, 1676 (1962a).

NÉEL, L., *Sur un problème de magnétostatique relatif à des couches minces ferromagnétiques*, C. R. Acad. Sci. **255**, 1545 (1962b).

NEUDERT, A., MCCORD, J., SCHÄFER, R., & SCHULTZ, L., *Domain-wall transformation by high-frequency magnetic fields*, Phys. Rev. B **75**, 172404 (2007).

NOGUÉS, J. & SCHULLER, I. K., *Exchange bias (review)*, J. Magn. Magn. Mater **192**, 203 (1999).

NOLTING, F., SCHOLL, A., STOHR, J., SEO, J. W., FOMPEYRINE, J., SIEGWART, H., LOCQUET, J. P., ANDERS, S., LÜNING, J., FULLERTON, E. E., TONEY, M. F., SCHEINFEIN, M. R., & PADMORE, H. A., *Direct observation of the alignment of ferromagnetic spins by antiferromagnetic spins*, Nature **405**, 767 (2000).

OOGANE, M., YILGIN, R., SHINANO, M., YAKATA, S., SAKURABA, Y., ANDO, Y., & MIYAZAKI, T., *Magnetic damping constant of Co_2FeSi Heusler alloy thin film*, J. Appl. Phys. **101**, 09J501 (2007).

PALMSTRØM, C., *Epitaxial Heusler Alloys: New Materials for Semiconductor Spintronics*, MRS Bulletin **28**, 725 (2003).

PANTOS, E., *X-Rays for Archaeology* (Springer, 2005).

PARK, J. P., EAMES, P., ENGEBRETSON, D. M., BEREZOVSKY, J., & CROWELL, P. A., *Imaging of spin dynamics in closure domain and vortex structures*, Phys. Rev. B **67**, 020403 (2003).

PARKIN, S., JIANG, X., KAISER, C., PANCHULA, A., ROCHE, K., & SAMANT, M., *Magnetically engineered spintronic sensors and memory*, Proc. IEEE **91**, 661 (2003).

PARKIN, S. S. P., MORE, N., & ROCHE, K. P., *Oscillations in exchange coupling and magnetoresistance in metallic superlattice structures: Co/Ru, Co/Cr, and Fe/Cr*, Phys. Rev. Lett. **64**, 2304 (1990).

PERZLMAIER, K., WOLTERSDORF, G., & BACK, C. H., *Observation of the propagation and interference of spin waves in ferromagnetic thin films*, Phys. Rev. B **77**, 054425 (2008).

PICOZZI, S., CONTINENZA, A., & FREEMAN, A., *Role of structural defects on the half-metallic character of Co_2MnGe and Co_2MnSi Heusler alloys*, Phys. Rev. B **69**, 94423 (2004).

PORTIER, X. & PETFORD-LONG, A. K., *The formation of 360° domain walls in magnetic tunnel junction elements*, Appl. Phys. Lett. **76**, 754 (2000).

PUZIC, A., VAN WAEYENBERGE, B., CHOU, K. W., FISCHER, P., STOLL, H., SCHÜTZ, G., TYLISZCZAK, T., ROTT, K., BRÜCKL, H., REISS, G., *et al.*, *Spatially resolved ferromagnetic resonance: Imaging of ferromagnetic eigenmodes*, J. Appl. Phys. **97**, 10E704 (2005).

QUITMANN, C., RAABE, J., BUEHLER, C., BUESS, M., JOHNSON, S., NOLTING, F., SCHLOTT, V., & STREUN, A., *Measuring magnetic excitations in microstructures using X-ray microscopy*, Nucl. Instr. Meth. Phys. Res. A (2008).

RAABE, J., QUITMANN, C., BACK, C., NOLTING, F., JOHNSON, S., & BUEHLER, C., *Quantitative Analysis of Magnetic Excitations in Landau Flux-Closure Structures Using Synchrotron-Radiation Microscopy*, Phys. Rev. Lett. **94**, 217204 (2005).

RAMEEV, B., YILDIZ, F., KAZAN, S., AKTAS, B., GUPTA, A., TAGIROV, L., RATA, D., BUERGLER, D., GRÜNBERG, P., SCHNEIDER, C. M., KÄMMERER, S., REISS, G., & HÜTTEN, A., *FMR investigations of half-metallic ferromagnets*, phys. stat. sol.(a) **1**, 10 (2006).

RAVE, W. & HUBERT, A., *Magnetic ground state of a thin-film element*, IEEE Trans. Mag. **36**, 3886 (2000).

REISS, G., *Magnetic Logic*, *in:* S. BLÜGEL, D. BÜRGLER, M. MORGENSTERN, C. M. SCHNEIDER, & R. WASER (eds.), *Spintronics, 40th IFF Spring School* (Forschungszentrum Jülich, 2009).

REMPFER, G. F., SKOCZYLAS, W. P., & GRIFFITH, O. H., *Design and performance of a high-resolution photoelectron microscope.*, Ultramicroscopy **36**, 196 (1991).

RÖNTGEN, W. C., *Ueber eine neue Art von Strahlen*, Annalen der Physik **300**, 12 (1898).

SAKURABA, Y., HATTORI, M., OOGANE, M., ANDO, Y., KATO, H., SAKUMA, A., MIYAZAKI, T., & KUBOTA, H., *Giant tunneling magnetoresistance in CoMnSi/ Al–O/ CoMnSi magnetic tunnel junctions*, Appl. Phys. Lett. **88**, 192508 (2006).

SCHECK, C., CHENG, L., & BAILEY, W. E., *Low damping in epitaxial sputtered iron films*, Appl. Phys. Lett. **88**, 252510 (2006).

SCHMALHORST, J., KÄMMERER, S., SACHER, M., REISS, G., HÜTTEN, A., & SCHOLL, A., *Interface structure and magnetism of magnetic tunnel junctions with a Co_2MnSi electrode*, Phys. Rev. B **70**, 24426 (2004).

SCHNEIDER, C. M., *Imaging Magnetization Dynamics*, *in:* S. BLÜGEL, T. BRÜCKEL, & C. M. SCHNEIDER (eds.), *Magnetism Goes Nano, 36th IFF Spring School* (Forschungszentrum Jülich, 2005).

SCHNEIDER, C. M., KUKSOV, A., KRASYUK, A., OELSNER, A., NEEB, D., NEPIJKO, S. A., SCHÖNHENSE, G., MÖNCH, I., KALTOFEN, R., MORAIS, J., DE NADAÏ, C., & BROOKES, N. B., *Incoherent magnetization rotation observed in subnanosecond time-resolving x-ray photoemission electron microscopy*, Appl. Phys. Lett. **85**, 2562 (2004).

SCHNEIDER, C. M., MEINEL, K., KIRSCHNER, J., NEUBER, M., WILDE, C., GRUNZE, M., HOLLDACK, K., CELINSKI, Z., & BAUDELET, F., *Element specific imaging of magnetic domains in multicomponent thin film systems*, J. Magn. Magn. Mat. **162**, 7 (1996).

SCHNEIDER, C. M. & SCHÖNHENSE, G., *Investigating surface magnetism by means of photoexcitation electron emission microscopy*, Rep. Progr. Phys. **65**, 1785 (2002).

SCHÖNHENSE, G., ELMERS, H. J., KRASYUK, A., WEGELIN, F., NEPIJKO, S. A., OELSNER, A., & SCHNEIDER, C. M., *Transient spatio-temporal domain patterns in permalloy microstructures induced by fast magnetic field pulses*, Nucl. Inst. and Meth. Phys. Res. B **246**, 1 (2006a).

SCHÖNHENSE, G., ELMERS, H. J., NEPIJKO, S. A., & SCHNEIDER, C. M., *Time-Resolved Photoemission Electron Microscopy*, Adv. Im. El. Phys. **142**, 159 (2006b).

SCHRYER, N. L. & WALKER, L. R., *The motion of 180° domain walls in uniform dc magnetic fields*, J. Appl. Phys. **45**, 5406 (1974).

SCHUMACHER, H. W., CHAPPERT, C., CROZAT, P., SOUSA, R. C., FREITAS, P. P., & BAUER, M., *Coherent suppression of magnetic ringing in microscopic spin valve elements*, Appl. Phys. Lett. **80**, 3781 (2002).

SCHÜTZ, G., WAGNER, W., WILHELM, W., KIENLE, P., ZELLER, R., FRAHM, R., & MATERLIK, G., *Absorption of circularly polarized x rays in iron*, Phys. Rev. Lett. **58**, 737 (1987).

SCHWABL, F., *Quantenmechanik* (Springer, 1992).

SIMONS, R. & WILEY, J., *Coplanar Waveguide Circuits, Components, and Systems* (John Wiley, 2001).

SLONCZEWSKI, J. C., *Fluctuation mechanism for biquadratic exchange coupling in magnetic multilayers*, Phys. Rev. Lett. **67**, 3172 (1991).

SLONCZEWSKI, J. C., *Origin of biquadratic exchange in magnetic multilayers (invited)*, J. Appl. Phys. **73**, 5957 (1993).

SLONCZEWSKI, J. C., *Overview of interlayer exchange theory*, J. Magn. Magn. Mater **150**, 13 (1995).

STANCIU, C. D., HANSTEEN, F., KIMEL, A. V., KIRILYUK, A., TSUKAMOTO, A., ITOH, A., & RASING, T., *All-optical magnetic recording with circularly polarized light*, Phys. Rev. Lett. **99**, 47601 (2007).

STÖHR, J. & SIEGMANN, H. C., *Magnetism - From Fundamentals to Nanoscale Dynamics* (Springer, 2006).

STILES, M. D., *Interlayer Exchange Coupling*, *in:* B. HEINRICH & J. A. C. BLAND (eds.), *Ultrathin Magnetic Structures III* (Springer, 2004).

STOCKMAN, M. I., KLING, M. F., KLEINEBERG, U., & KRAUSZ, F., *Attosecond nanoplasmonic-field microscope*, Nature Photonics **1**, 539 (2007).

STÖHR, J., WU, Y., HERMSMEIER, B. D., SAMANT, M. G., HARP, G. R., KORANDA, S., DUNHAM, D., & TONNER, B. P., *Element-specific magnetic microscopy with circularly polarized X-rays*, Science **259**, 658 (1993).

STONER, E. C., *Collective Electron Ferromagnetism*, Proc. Roy. Soc. Lond. Ser. A, Math. Phys. Sc. p. 372 (1938).

TAMARU, S., BAIN, J. A., VAN DE VEERDONK, R. J. M., CRAWFORD, T. M., COVINGTON, M., & KRYDER, M. H., *Imaging of quantized magnetostatic modes using spatially resolved ferromagnetic resonance*, J. Appl. Phys. **91**, 8034 (2002).

THEIS-BRÖHL, K., SCHEIDT, R., ZEIDLER, T., SCHREIBER, F., ZABEL, H., MATHIEU, T., MATHIEU, C., & HILLEBRANDS, B., *Magnetic exchange-coupling effects in asymmetric trilayer structures of MBE-grown Co/Cr/Fe*, Phys. Rev. B **53**, 11613 (1996).

THOLE, B. T., CARRA, P., SETTE, F., & VAN DER LAAN, G., *X-ray circular dichroism as a probe of orbital magnetization*, Phys. Rev. Lett. **68**, 1943 (1992).

THOMAS, L., SAMANT, M. G., & PARKIN, S. S. P., *Domain-Wall Induced Coupling between Ferromagnetic Layers*, Phys. Rev. Lett. **84**, 1816 (2000).

TONNER, B. P. & HARP, G. R., *Photoelectron microscopy with synchrotron radiation*, Rev. Sc. Instr. **59**, 853 (1988).

TSERKOVNYAK, Y., BRATAAS, A., & BAUER, G. E. W., *Enhanced Gilbert damping in thin ferromagnetic films*, Phys. Rev. Lett. **88**, 117601 (2002).

UNGURIS, J., CELOTTA, R. J., & PIERCE, D. T., *Observation of two different oscillation periods in the exchange coupling of Fe/Cr/Fe(100)*, Phys. Rev. Lett. **67**, 140 (1991).

VOGEL, J., KUCH, W., BONFIM, M., CAMARERO, J., PENNEC, Y., OFFI, F., FUKUMOTO, K., KIRSCHNER, J., FONTAINE, A., & PIZZINI, S., *Time-resolved magnetic domain imaging by x-ray photoemission electron microscopy*, Appl. Phys. Lett. **82**, 2299 (2003).

VOGEL, J., KUCH, W., CAMARERO, J., FUKUMOTO, K., PENNEC, Y., BONFIM, M., PIZZINI, S., PETROFF, F., FONTAINE, A., & KIRSCHNER, J., *Time and layer resolved magnetic domain imagig of FeNi/Cu/Co trilayers using x-ray photoelectron emission microscopy (invited)*, J. Appl. Phys. **95**, 6533 (2004).

VOGEL, J., KUCH, W., HERTEL, R., CAMARERO, J., FUKUMOTO, K., ROMANENS, F., PIZZINI, S., BONFIM, M., PETROFF, F., FONTAINE, A., & KIRSCHNER, J., *Influence of domain wall interactions on nanosecond switching in magnetic tunnel junctions*, Phys. Rev. B **72**, 220402 (2005).

WANG, W. H., PRZYBYLSKI, M., KUCH, W., CHELARU, L. I., WANG, J., LU, Y. F., BARTHEL, J., MEYERHEIM, H. L., & KIRSCHNER, J., *Magnetic properties and spin polarization of Co_2MnSi Heusler alloy thin films epitaxially grown on GaAs (001)*, Phys. Rev. B **71**, 144416 (2005).

WEBSTER, P. J. & ZIEBECK, K. R. A., *Alloys and Compounds of d-Elements with Main Group Elements, Part 2, in: Landolt-Börnstein III/9c*, p. 75 (Springer, 1988).

WEGELIN, F., VALDAITSEV, D., KRASYUK, A., NEPIJKO, S. A., SCHÖNHENSE, G., ELMERS, H. J., KRUG, I., & SCHNEIDER, C. M., *Magnetization dynamics in microscopic spin-valve elements: Shortcomings of the macrospin picture*, Phys. Rev. B **76**, 134410 (2007).

WEN, C. P., *Coplanar Waveguide: A Surface Strip Transmission Line Suitable for Nonreciprocal Gyromagnetic Device Applications*, Microwave Theory and Techniques, IEEE Transactions on **17**, 1087 (1969).

WIJN, H. P. J., *Magnetic Properties of Metals - d-Elements, Alloys and Compounds* (Springer, 1991).

WOODRUFF, D. P., *Surface structure determination using x-ray standing waves*, Rep. Prog. Phys. **68**, 743 (2005).

WURMEHL, S., FECHER, G. H., KANDPAL, H. C., KSENOFONTOV, V., FELSER, C., LIN, H. J., & MORAIS, J., *Geometric, electronic, and magnetic structure of Co_2FeSi: Curie temperature and magnetic moment measurements and calculations*, Phys. Rev. B **72**, 184434 (2005).

YAMAMOTO, M., MARUKAME, T., ISHIKAWA, T., MATSUDA, K., UEMURA, T., & ARITA, M., *Fabrication of fully epitaxial magnetic tunnel junctions using cobalt-based full-Heusler alloy thin film and their tunnel magnetoresistance characteristics*, J. Phys. D: Appl. Phys. **39**, 824 (2006).

YANG, S. H., MUN, B., MANNELLA, N., KIM, S. K., KORTRIGHT, J. B., UNDERWOOD, J., SALMASSI, F., ARENHOLZ, E., YOUNG, A., HUSSAIN, Z., VAN HOVE, M. A., & FADLEY, C. S., *Probing buried interfaces with soft x-ray standing wave spectroscopy: application to the Fe/Cr interface*, J. Phys. Cond. Mat. **14**, 407 (2002).

YANG, S. H., MUN, B. S., KAY, A. W., KIM, S. K., KORTRIGHT, J. B., UNDERWOOD, J. H., HUSSAIN, Z., & FADLEY, C. S., *Depth-resolved photoemission spectroscopy from surface and buriedlayers with soft x-ray standing waves*, Surf. Sc. **461**, L557 (2000).

YUAN, S. W. & BERTRAM, H. N., *Domain-wall dynamic transitions in thin films*, Phys. Rev. B **44**, 12395 (1991).

YUASA, S., NAGAHAMA, T., FUKUSHIMA, A., SUZUKI, Y., & ANDO, K., *Giant room-temperature magnetoresistance in single-crystal Fe/MgO/Fe magnetic tunnel junctions*, Nature Materials **3**, 868 (2004).

ZABEL, H., *Magnetism of chromium at surfaces, at interfaces and in thin films*, J. Phys. Cond. Matt. **11**, 9303 (1999).

ZAKERI, K., *unpublished result* (2007).

Publications

Articles in refereed journals

C.M. Schneider, I. Krug, M. Müller, F. Matthes, A. Kaiser, C. Wiemann, S. Cramm, H.-J. Elmers, F. Wegelin, A. Krasyuk, S.A. Nepijko, G. Schönhense
Investigating Spintronics Thin Film Systems with Synchrotron Radiation
Radiation Physics and Chemistry (in press, 2009).

A. Kaiser, C. Wiemann, S. Cramm, C. M. Schneider
Influence of Magnetocrystalline Anisotropy on the Magnetization Dynamics of Magnetic Microstructures
Journal of Physics Condensed Matter **21**, 314008 (2009).

A. Kaiser, D. Banerjee, A.D. Rata, C. Wiemann, S. Cramm, C.M. Schneider
Magnetic microstructure of candidates for epitaxial dual Heusler magnetic tunnel junctions
Journal of Magnetism and Magnetic Materials **321**, 1182 (2009).

F. Kronast, R. Ovsyannikov, A. Kaiser, C. Wiemann, S.-H. Yang, A.Locatelli, D. E. Bürgler, R. Schreiber, F. Salmassi, P. Fischer, H.A. Dürr, C. M. Schneider, W. Eberhardt, C. S. Fadley
Depth-resolved soft x-ray photoelectron emission microscopy in nanostructures via standing-wave excited photoemission
Applied Physics Letters **93**, 243116 (2008)

Conference contributions – talks

A. Kaiser, C. Wiemann, S. Cramm, C.M. Schneider
Magnetization Dynamics in Interlayer Exchange Coupled Magnetic Microstructures
Frühjahrstagung der DPG, Dresden, Germany, 22.-27.03.2009.

A. Kaiser, C. Wiemann, S. Cramm, C.M. Schneider
Magnetization dynamics of magnetic microstructures using time-resolved PEEM with deflection gating
LEEM/PEEM VI, Trieste, Italy, 7.-11.09.2008.

Conference contributions – posters

A. Kaiser, C. Wiemann, S. Cramm, C. M. Schneider, C. Tieg
Layer-resolved Magnetization Dynamics in Interlayer Exchange Coupled Trilayers
International Colloquium on Magnetic Films and Surfaces, Berlin, Germany, 20.-24.07.2009.

A. Kaiser, C. Wiemann, S. Cramm, C. M. Schneider, C. Tieg
Slow and fast excitation of magnetization dynamics in interlayer coupled heterostructures
International Workshop: Nanomagnetism probed by X-rays and Neutrons, Bochum, Germany, 12.-13.06.2009.

A. Kaiser, C. Wiemann, S. Cramm, C. M. Schneider
Time-resolved PEEM measurements on single-crystalline Fe-structures
Frühjahrstagung der DPG, Berlin, Germany, 25.-29.02.2008.

C. Wiemann, A. Kaiser, S. Cramm, C. M. Schneider
Gated detector for time-resolved photoemission microscopy
Frühjahrstagung der DPG, Berlin, Germany, 25.-29.02. 2008.

A. Kaiser, D. Rata, S. Cramm, C.M. Schneider
Magnetism and magnetic microstructure in Heusler alloy based thin film systems
Frühjahrstagung der Deutschen Physikalischen Gesellschaft, Regensburg, 26.03.2007.

A. Kaiser, C. Wiemann, S. Cramm, H. Pfeifer, C.M. Schneider
Gated detector for time-resolved photoemission microscopy
BESSY User Meeting, Berlin, 06.12.2007.

F. Kronast, R. Ovsyannikov, A. Locatelli, H.A. Dürr, A. Kaiser, C. Wiemann, R. Schreiber, D. Bürgler, C.M. Schneider, C.S. Fadley
Spectromicroscopy with depth resolution via standing wave excitation
BESSY User Meeting, Berlin, 06.12.2007.

A. Kaiser, D. Rata, S. Cramm, C.M. Schneider
Magnetism and magnetic microstructure in Heusler alloy based thin film systems
BESSY Users' Meeting, Berlin, 07.-08.12.2006.

Other publications

A. Kaiser, C. Wiemann, S. Cramm, C.M. Schneider
Magnetic domain structure of Heusler/MgO/Heusler trilayer systems
IFF Scientific report 2008 & BESSY Annual Report 2008.

F. Kronast, S. Döring, M. Gorgoi, R. Ovsyannikov, A. Kaiser, C. Wiemann, S.-H. Yang, M. Huijben, A. Locatelli, D. E. Bürgler, R. Schreiber, F. Schäfers, W. Braun, H. A. Dürr, C. M. Schneider, C. Westphal, C. S. Fadley
Looking beneath the surface: Standing-waves and hard X-ray photoemission
BESSY Highlights 2007.

Schriften des Forschungszentrums Jülich
Reihe Information / Information

1. **Ferrocenes as Potential Building Blocks for Molecular Electronics**
   Self-Assembly and Tunneling Spectroscopy
   by L. Müller-Meskamp (2008), 153 pages
   ISBN: 978-3-89336-509-8

2. **Magnetic Proximity Effects in Highly-ordered Transition Metal Oxide Heterosystems studied by Soft x-Ray Photoemission Electron Microscopy**
   by I. P. Krug (2008), XX, 180 pages
   ISBN: 978-3-89336-521-0

3. **Seltenerd-basierte ternäre Oxide als alternative Gatedielektrika**
   von J. M. Roeckerath (2008), 148 Seiten
   ISBN: 978-3-89336-543-2

4. **Strominduzierte Magnetisierungsdynamik in einkristallinen Nanosäulen**
   von R. Lehndorff (2009), I, 86 Seiten
   ISBN: 978-3-89336-564-7

5. **Magnetization Dynamics in Magnetically Coupled Heterostructures**
   von A. Kaiser (2009), X, 121 Seiten
   ISBN: 978-3-89336-577-7

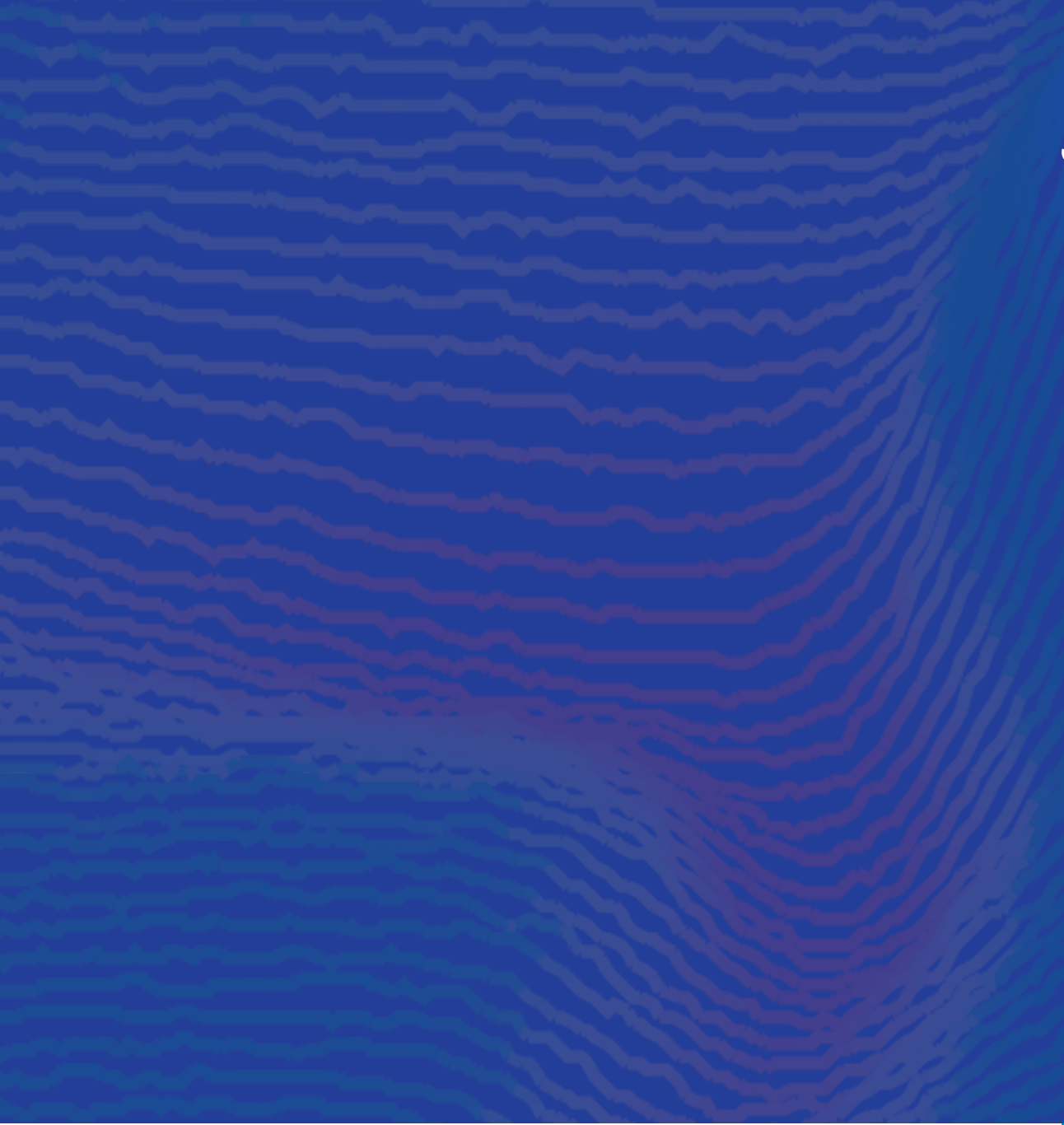

Information
Band / Volume 5
ISBN 978-3-89336-577-7

JÜLICH
FORSCHUNGSZENTRUM